UNIVERSITE DE LIMOGES

ECOLE DOCTORALE n° 521 – Science et Ingénierie pour l'Information
FACULTE des Sciences et Techniques
Xlim – Départements Photonique - Ondes et Systèmes Associés

Thèse N° [-----]

Thèse
pour obtenir le grade de
DOCTEUR DE L'UNIVERSITÉ DE LIMOGES
Discipline / Spécialité : Electronique des Hautes Fréquences, Photonique et Systèmes

Présentée et soutenue par
Annalisa DE ANGELIS

le 29 Novembre 2012

Electro-optical pump-probe system suitable for the investigation of electroporated biological cells

Thèse dirigée par Vincent Couderc et Philippe Lévêque

JURY :

Rapporteurs

M. Justin TEISSIE — **Directeur de Recherche Emérite CNRS**
Institut de Pharmacologie et de Biologie Structurale, Toulouse

M.me Katia GRENIER — **HDR Chargé de Recherche CNRS**
Laboratoire d'Analyse et d'Architecture des Systèmes, Toulouse

Examinateurs

M. P. Thomas VERNIER — **Research Associate Professor and Engineering Manager MOSIS**
USC, Ming Hsieh Departement of Electrical Engineering, Los Angeles

M. Christophe LAUX — **Professeur des Universités**
Laboratoire EM2C, UPR 288 CNRS, Ecole Centrale Paris, Paris

M. Vincent COUDERC — **Directeur de Recherche CNRS**
Université de Limoges, XLIM, Dépt. « Photonique », Limoges

M. Philippe LEVEQUE — **Directeur de Recherche CNRS**
Université de Limoges, XLIM, Dépt. « OSA », Limoges

Invités

M. Philippe LEPROUX — **Maître de Conférences**
Université de Limoges, XLIM, Département « Photonique », Limoges

Don't keep forever in the public road, going only where others have gone.
Leave the beaten track occasionally and dive into the woods.
You will be certain to find something you have never seen before.

Alexander Graham Bell (1906)

Acknowledgements

I would like to express my gratitude to Vincent Couderc and Philippe Leveque, my research supervisors, for the kind welcome in their research equip, and for allowing me to carry out my PhD thesis. I would also like to thank Philippe Leproux for sharing his competences with me and for his useful critiques. A deep gratitude to Alessandro Tonello, Alexis Labruyère and Marco Andreana which are involved in the part of the work concerning the numerical optical simulations. I wish also to thank my colleagues Saad El Amari and Sophie Kohler which have collaborate to the design and the characterization of the electric pulse exposure system.

I am particularly grateful for the technical assistance of Patrick Frugier which provided me the mechanical support in setting up my system.

I would like to express my special thanks to Caterina Merla which, not only has collaborated to the thesis revision but she is also a precious reference, support and friend for me.

Résumé

L'étude présenté dans ce manuscrit s'inscrit dans le projet Bio-Electro-Photonique, transversal aux départements OSA (Ondes et systèmes associés) et Photonique. Il s'agit d'un projet de recherche codirigé par Philippe Lévêque (OSA) et Vincent Couderc (Photonique) au sein du laboratoire Xlim, à l'Université de Limoges. Ce projet concerne l'étude des interactions entre le champ électromagnétique et les tissus biologiques à l'échelle cellulaire. L'objectif est l'exploration et l'utilisation d'impulsions électriques et optiques ultracourtes de très forte amplitude en vue d'atteindre et d'observer directement le noyau des cellules biologiques. L'équipe Bio-Electro-Photonique, dont je fais partie depuis Octobre 2009, s'intéresse notamment à l'étude des interactions au niveau de la membrane cellulaire qui semblerait être l'endroit où l'on observe la plupart des effets de l'application du champ électrique.

La membrane cellulaire est une double couche de molécules formées par un corps apolaire (hydrophobe) orienté vers l'intérieur et une tête polaire (hydrophile) vers l'extérieur. Elle est entourée sur chaque coté de molécules d'eau et ions à concentrations différentes qui en détermine le potentiel transmembranaire au repos, généralement compris entre -40 et -80 mV dans des conditions physiologiques. Une caractéristique importante de la membrane cellulaire est sa perméabilité sélective qui permet de contrôler l'entrée et la sortie des différentes molécules et ions entre les milieux extérieur et intérieur.

Dans un point de vue électrique, on peut imaginer la membrane cellulaire comme un isolateur entre deux électrolytes : la suspension à l'extérieur et le plasma à l'intérieur. Isolateur et électrolytes sont caractérisés par des propriétés électriques spécifiques, en termes de conductivité et permittivité, responsables de la réponse de la cellule au champ électrique. Notamment, quand un champ électrique pulsé de forte intensité (ordre de kV/cm) et courte durée (< ms) est appliqué à la cellule biologique, un potentiel induit va s'ajouter au potentiel à repos, en augmentant la conductivité et, par conséquence, la perméabilité de la membrane. Une telle « électroperturbation » semblerait conduire à la formation de pores hydrophiles, puis à un réarrangement des molécules d'eau et de la bicouche membranaire, d'où le nom de « électroporation ». Les paramètres des impulsions appliquées jouent un rôle important dans la détermination des effets induits sur la cellule. En particulier, la durée des impulsions (et donc le contenu fréquentiel) détermine où les effets se produisent: les impulsions dites longues (ordre des millisecondes or microsecondes) agissent sur la membrane plasmique, tandis que les impulsions plus courts (nanosecondes et picosecondes) atteignent les membranes intracellulaires. Les impulsions longues ont rapidement été utilisées pour des applications médicales (électrochimiothérapie, électrotransfert de gènes) et biotechnologiques (stérilisation d'aliments). Très récemment, l'intérêt de la communauté scientifique s'est adressée à l'étude des

effets des « nanopulses » (impulsions d'une durée plus courte des centaines de nanosecondes, et une amplitude de l'ordre des MV/cm), qui pourraient trouver application dans la thérapie du cancer, en évitant l'administration de médicaments anticancéreux.

A présent, ce domaine de recherche n'est pas encore suffisamment exploré à cause de la manque d'outils technologiques à la fois pour la stimulation cellulaire et pour le diagnostic et l'imagerie de ces phénomènes à l'échelle subcellulaire et avec une dynamique temporelle de quelques microsecondes.

Dans un tel contexte, nous avons conçu et réalisé un système complet et compact de pompe électrique et sonde optique pour l'investigation des effets biologiques des « nanopulses » sur la cellule biologique.

La « pompe électrique » représente le système de stimulation électrique : elle est composé par un générateur à « ondes gelées » basé sur la photo-commutation de composantes électro-optiques déclenchées par commande optique. La commande optique est fournie par un microlaser qui délivre des impulsions sub-nanosecondes. Le même laser est utilisé dans le système de « sonde optique », basé sur le processus non linéaire multiplex-CARS (Coherent anti-Stokes Raman Scattering). Dans le processus CARS, une première onde, dite de *pompe*, et une deuxième onde, dite *Stokes*, sont envoyées sur l'échantillon. Leur différence en termes de longueurs d'onde, excite une vibration moléculaire spécifique, donnant naissance à l'onde dite *anti-Stokes*. Celle-ci est utilisée pour construire l'image de l'échantillon à partir des spectres enregistrés des molécules qui le composent. L'adjectif « multiplex » signifie que l'on remplace le faisceau Stokes, généralement monochromatique, par un faisceau polychromatique qui permet d'exciter plusieurs résonnances moléculaires à la fois.

Pour la partie de stimulation électrique, on a réalisé un générateur dans la géométrie « microruban ». Cette typologie de générateur délivre des impulsions électriques ultra-rapide et à très haute intensité dont la durée dépend de la longueur de la ligne de transmission et le profil suit celui de l'impulsion optique. Il est dans ces conditions possible de synchroniser le générateur et la commande optique grâce à une gigue temporelle faible (< 2 ps) et au régime linéaire choisi pour la photo-commutation. Le générateur est adapté en impédance au système d'exposition et à la solution biologique pour un maximum d'énergie délivrée aux cellules. Le système d'application des impulsions électriques est dans une typologie « microchambre », convenant à la microscopie : deux électrodes biocompatibles sont collées en parallèle sur la lamelle d'un microscope. Elles forment un canal où les cellules biologiques en solution sont déposées afin d'être exposées au champ électrique. Cette technologie de système d'exposition, déjà présentée et caractérisée dans études précédents de l'équipe Bio-Electro-Photonique, est ici reprise et mieux adaptée au système complet et aux impulsions sub-nanosecondes.

Pour ce qui concerne la partie « sonde optique », une source laser en régime sub-nanoseconde pour l'imagerie multiplex-CARS est présentée de façon complète ici pour la première fois à notre connaissance.

Une des façons la plus connue de générer un élargissement spectral (supercontinuum) de l'onde Stokes est de faire passer le faisceau du laser fondamental dans une fibre optique à cristaux photoniques (PCF). Le régime sub-nanoseconde présente plusieurs avantages par rapport aux sources femtosecondes ou picosecondes normalement utilisées. Notamment, les impulsions optiques sub-nanosecondes ont une faible sensibilité aux effets de dispersion dans la fibre, permettant un recouvrement spatial et temporel plus efficace des deux ondes, pompe et Stokes, indispensable pour la microspectroscopie CARS. En plus, les impulsions plus longues ont un meilleur contraste vibrationnel intrinsèque et, donc, une meilleure résolution spectrale. En revanche, les mécanismes qui produisent l'élargissement spectral du faisceau sub-nanoseconde dans la PCF ne sont pas très connus et ils sont étudiés pour la première fois et décrits en détail dans ce manuscrit.

Dans un premier temps nous avons mise en place le chemin optique pour les trois faisceaux : celui qui déclenche la génération des impulsions électriques, et les deux ondes, de pompe et Stokes, pour la microspectroscopie multiplex-CARS. Le faisceau de pompe se propage dans l'air, tandis que le faisceau Stokes est injecté dans 7 mètres de PCF, en obtenant un supercontinuum de 400 nm à 2000 nm. En suite, afin de synchroniser l'onde de pompe et l'onde Stokes, nous avons projeté deux typologies de lignes à retard le long du chemin optique de pompe. Dans le spécifique, nous avons montée une ligne à retard formée par une succession des miroirs qui acheminent le faisceau de pompe en lui faisant parcourir une trajectoire de longueur ajustable par translation horizontale des miroirs. Just après cette ligne à retard, nous avons réalisé une cavité d'Herriott : deux miroirs sont placés l'un en face de l'autre à une distance qui dépende des rebondis que l'on souhaite faire accomplir au faisceau, susceptible de rester confiné dans cette cavité multi-passage sans pertes et en évitant que le faisceau diverge.

Enfin, nous avons vérifié et améliorer la superposition spatiale et temporelle des deux ondes optiques en optimisant la génération de la somme de fréquences dans un cristal KDP.

Dans un second temps, nous nous sommes intéressés à un cas particulier de source laser pour la microspectroscopie multiplex-CARS. Dans ce cas là, nous avons pu augmenter le taux de répétition des impulsions laser fondamentales car nous n'avions pas les contraintes de la partie électrique qui nécessite d'une énergie optique suffisante à déclencher une photo-commutation efficace. Néanmoins, en augmentant la fréquence de répétition du laser, nous avons eu besoin d'amplifier la puissance crête des impulsions afin d'engendrer les effets non linéaire qui génèrent l'élargissement spectral dans la PCF et qui requièrent un seuil spécifique. Dans ce but, nous avons ajouté un amplificateur optique fibré sur le chemin optique de l'onde Stokes. Le

passage dans la fibre de l'amplificateur introduit des distorsions du profile temporel des impulsions Stokes. Nous avons analysé en détail les phénomènes qui sont à la base de la génération du supercontinuum dans ce cas spécifique. En particulier, nous avons démontré expérimentalement et à l'aide de simulations numériques la compétition des deux effets non linéaires principaux qui mènent à la génération de composantes spectrales éparpillées autour de la longueur d'onde originale : l'instabilité de modulation et le gain Raman. La première apparait sous la forme d'oscillations d'amplitude du profile des impulsions et elle semblerait représenter le commencement de la formation d'ondes solitoniques. Un soliton est une onde se propageant à travers la fibre optique sans modification d'amplitude et de durée, grâce à la concurrence de la dispersion linéaire et des effets non linéaire propres de la PCF. Le gain Raman dans un second temps déplace les solitons vers des longueurs d'ondes plus longues, élargissant de cette façon le spectre du faisceau optique.

Pour conclure, le système électro-optique pompe-sonde qui a fait l'objet de ma thèse, présente une nouveauté importante via l'utilisation d'une source laser en régime sub-nanoseconde qui convient, à la fois, à la technologie choisi pour la stimulation électrique et celle pour la detection optique de la cellule biologique. La source pour le système d'imagerie multiplex-CARS est proposée en tant que nouvelle méthode non invasive (pas besoin de marqueurs pour l'échantillon) pour étudier les mécanismes à la base de l'électroporation de la membrane cellulaire. Il en résulte un système compact et complet. Le générateur est robuste, stable et permet de générer des « nanopulses » avec des profils et des durées ajustables selon l'application.

La source M-CARS sub-nanoseconde a montré une synchronisation aisée entre le faisceau de pompe et Stokes et un meilleur recouvrement spatial grâce à une moindre sensibilité à la dispersion dans la fibre optique par rapport aux impulsions picosecondes ou femtosecondes. En outre, le meilleur contraste spectral et la rapidité de prise d'images font de telle source une candidate idéale à être employer comme système d'imagerie temps-réelle des phénomènes rapides qui concernent l'électroporation et, plus généralement, les interactions du champ électromagnetique avec la cellule biologique.

Les résultats de mes travaux de thèse ont été publiés dans trois différents revues à comité de lecture international et ont étés présentés dans cinq communications internationales et deux nationales.

Par ailleurs, le système de source dédié à la microspectroscopie M-CARS a été l'objet d'un brevet.

Une liste des communications est détaillée à la fin du manuscrit.

CONTENTS

List of Figures

List of Tables

List of Acronyms (alphabetical order)

BS: beam splitter
CARS: Coherent anti-Stokes Raman Scattering
C-CARS: Counter-propagating CARS
E-CARS: Epi-CARS (backward-propagating radiation)
F-CARS: Forward- propagating CARS
FIR: Far-Infrared
FWHM: Full Width at Half of the Maximum value
FWM: Four Wave Mixing
GaAs: Gallium Arsenide
GNLSE: Generalized Non-Linear Schrodinger Equation
GVD: Group Velocity Dispersion
IR: Infrared
LP: Long-pass Filter
M-CARS: multiplex-CARS
MF: Microstructured Fiber
MI: Modulation Instability
NA: Numerical Aperture
NIR: Near Infrared
NLSE: Non-Linear Schrodinger Equation
nsPEF: Nanosecond Pulsed Electric Field
OPA: Optical Parametric Amplifier
OPO: Optical Parametric Oscillator
PBF: Photonic Band-gap Fiber
P-CARS: Polarization-detected CARS
PCB: Printed Circuit Board
PCF: Photonic Crystal Fiber
PCSS: Photoconductive Semiconductor Switch
PEF: Pulsed Electric Field
PFL: Pulse Forming Line
SC: Supercontinuum
SF: Short-pass Filter
SFG: Sum Frequency Generation
SHG: Second Harmonic Generation
SMF: Standard Monomode Fiber
SPM: Self-Phase Modulation
SRS: Stimulated Raman Scattering
SSFS: Soliton Self Frequency Shift
TMP: Transmembrane Potential
XPM: Cross-Phase Modulation
YDFA: Ytterbium-Doped Fiber Amplifier
ZWD: Zero Wavelength Dispersion

General Introduction

Since the Science started to be interested in how electromagnetic field interacts with the human body, the researchers have been involved in studying phenomena at different scale, starting from the macroscopic to cellular and molecular interactions. This escalation from the macroscopic to the microscopic has been accompanied by technological improvements that have permitted to deepen the knowledge and the understanding of the interaction mechanisms. Nowadays, it is well known that an electric field of sufficient magnitude is able to perturb a cell immersed in it [1]. Each cell is enveloped by a plasma membrane which is first responsible of the cell response to the applied electric field. The plasma membrane, essentially formed by a double layer of lipids, behaves partly as a liquid and partly as a gel. It is a selectively permeable barrier with the main function of protecting the cell interior, and also facilitating the flow of selected types of ions and other materials from and to its surroundings. Such selectivity maintains the equilibrium in ion concentration between the exterior and the interior of cell, determining a difference of the potential at the outer and the inner sides of the membrane (transmembrane potential, TMP). This resting potential under physiological conditions is comprised between -40 mV and -80 mV.

Electrically, the plasma membrane can be viewed as a thin insulator surrounded on both sides by aqueous electrolyte solutions. When exposed to a strong enough electric field (intensity of the order of kV/cm and duration < ms), the membrane undergoes an electrical breakdown which changes its permeability, and, consequently, its dielectric properties. As largely associated to the formation of aqueous pathways in the cell membrane, called pores, we are used to refer to this process as “electroporation” or “electropermeabilization”.

Since its discovery, electroporation has gained ground as a useful tool in biotechnological (bacterial decontamination [2]) and medical (electrochemoterapy [3], [4], [5], DNA electrotransfer [6–8], trans-dermal drug delivery [9]) applications, justifying so the growing interest in better understanding the nature of the mechanisms leading to electroporation. To date, thanks to molecular dynamics simulation and experimental observations, we know that when a cell is exposed to an external field, a voltage is induced across the plasma membrane [10]. This voltage is proportional to the field strength and superimposes onto the resting voltage. It has been observed that a high voltage on the membrane reduces the energy necessary for rearrangements of the membrane lipids, resulting in formation of aqueous passages (hydrophilic pores) and consequently in an increased conductivity and permeability of the membrane [11]. The resting voltages that are normally present on the cell membrane and on the organelle membranes are clearly insufficient for this, as

electroporation is not observed under physiological conditions. Conversely, with exposures to electric fields able to induce total membrane voltages of several hundreds of millivolts, the electroporation of the cell membrane becomes readily achievable in experiments.

The fields used for electroporation are most often delivered in the form of unipolar rectangular pulses, with typical amplitudes of several hundred volts per centimeter, durations ranging from tens of microseconds up to milliseconds, and microseconds duration risetimes. In the first few microseconds after the onset of the pulse, these exposures induce a voltage in the range of several hundred millivolts on the cell membrane, and this voltage persists until the end of the pulse. Although they are used less commonly, bipolar rectangular pulses [12] and sinusoidal or sine-modulated rectangular pulses [13].

More recently the development of shorter pulses in the range of μs and ns with amplitude varying from kV/m up to few MV/m, have assumed increased significance mainly for their potential in medical applications [14]. In fact this kind of exposure is able to induce voltages on the intracellular sub-structures thus affecting organelle membranes, providing a promising base for treating cancer tumors without delivering drugs.

Today, the mechanisms beyond the electroporation are not yet well known. The debate on electroporation mechanism is still open. For example the trigger event of the pore formation as well as the pore formation kinetics times show discrepancies between simulations and experimental results [11]. The difficulty in performing real-time detection of this ultra-rapid and subcellular-scale phenomenon and the lack of exposure system (electrical pulse generator and microelectrode) adapted to microscopy and biological environment represent major limits for microscopic-scale investigations.

All attempts to observe directly the pore formation have failed. With submicrometric radii, the pores are too small to be observed under an optical microscope, whereas the sample preparation for the electronic microscope is too aggressive for the “metastable” structure of the plasma membrane [11]. However, imaging of cell membrane is of great importance for precisely describing the events leading to membrane electropermeabilization.

The most of current electroporation experimental studies uses fluorescence microscopy as technique for cell imaging. The limits of this method lie in the need of markers such as fluorescent dyes or, more recently, quantum dots, that can be used for dead tissue or fixed cells but not for living organisms (whether *in vitro* or *in vivo*). In fact, the insertion of exogenous molecules can significantly affect the cell metabolism or be toxic even at low concentrations.

The lack of more detailed information, if on the one hand implies that the details of cell electroporation are not still fully understood, on the other hand, makes this scientific domain more and more interesting.

From this context arises the project "BioElectroPhotonique" within the "Institut de Recherche" Xlim, at the University of Limoges. This is a transversal project that brings two research areas together, namely Bioelectromagnetics and Nonlinear Optics. That project is based on the collaboration between two Departments of Xlim: OSA (Ondes et Systèmes Associés, Waves and associated systems), and Photonique. Since few years, the BioElectroPhotonique group works to the conception and the realization of hardware devices for electrical cell stimulation (pulse generator [15], [16], [17], [18], and exposure system [19], [20]) with the final purpose to quantitatively and qualitatively characterize the electrical field bioeffects (Figure I-1). The quantitative analysis is represented by dosimetric studies both numerical and experimental [21], [22]. The qualitative analysis is mainly performed through models of molecular dynamic [23] or, experimentally, by fluorescence microscopy.

Since 2009, I have taken part in this project with the thrilling challenge to provide a complete and compact system that involves all the rings of the electroporation investigation chain, from the electric field application on biological cell to the bioeffects detection (red pathway in Figure I-1).

Precisely, the work of my PhD thesis concerns the design and characterization of an electro-optical pump-probe system permitting both the electrical stimulation of a biological cell, and the 3D imaging of the cell response, through a nonlinear optical technique, called multiplex-CARS (Coherent anti-Stokes Raman Scattering) microspectroscopy.

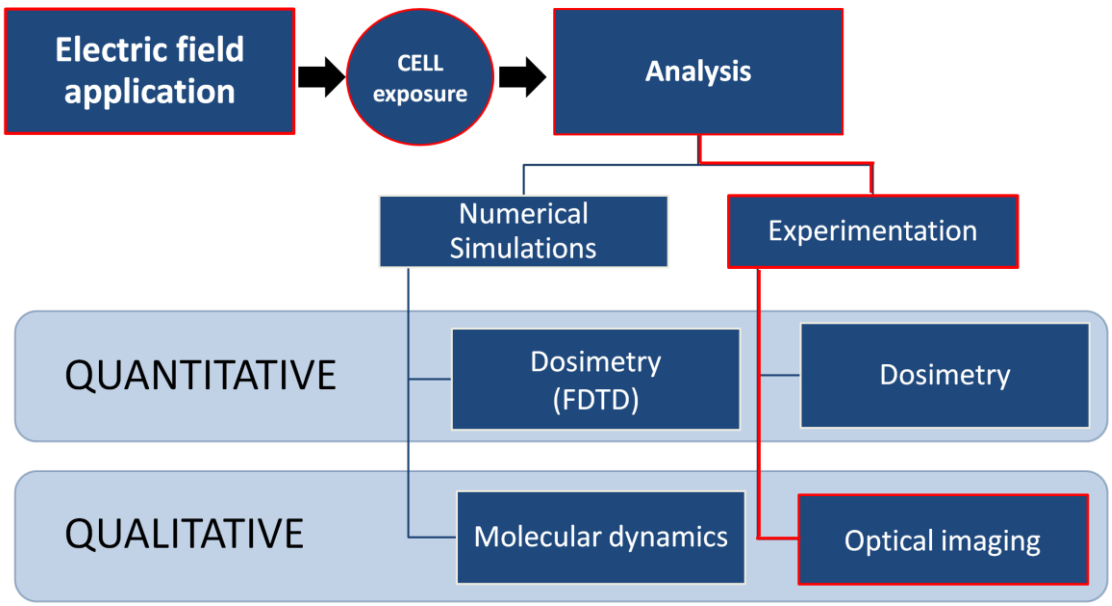

Figure I-1: *Overview of the different research branches of the "BioElectroPhonique" project within the "Insistut de Recherche Xlim". The red pathway on the chart illustrates the part of the project concerning my PhD thesis work described in this manuscript.*

Current electroporation researches are now focusing more attention to develop new imaging techniques based on intrinsic optical properties of biological tissues [24]. Among these imaging techniques, Coherent Anti-Stokes Raman Scattering (CARS) micro-spectroscopy permits to obtain images of cell membrane structure by exploiting the vibrational resonance of each chemical bond. In particular, the lipids forming cell membranes contain a large number of carbon-hydrogen bonds with a large Raman cross section and hence an intense CARS signal.

In CARS process, two laser beams are used for excitation: the *pump beam* and the *Stokes beam*, and a third beam, named *probe beam* detects the emission of an anti-Stokes photon. In this process the three beams (*pump, Stokes*, and *probe)* need to be temporally and spatially overlapped on the sample for generating the CARS signal. Generally, all the beams are monochromatic and their wavelength difference is tuned to be resonant with a molecular vibration, in order to obtain a more intense CARS signal. Nevertheless, a broadband Stokes beam can be used for exciting a larger number of chemical bonds at the same time, performing the so-called multiplex-CARS (M-CARS) microspectroscopy.

The main drawback of M-CARS method is the requirement for bulky femtosecond and picosecond laser systems for generating a stable broadband beam (supercontinuum generation). An important innovation introduced by our system is to work in subnanosecond regime. Indeed, the advances in laser technologies like the introduction of compact subnanosecond laser sources and the advent of photonic crystal fibers (PCFs) have paved the way for a new method of broadband beam generation suitable for M-CARS microspectroscopy. The pump and Stokes sub-nanosecond pulses have several advantages (e.g. a high vibrational contrast and a better spectral resolution) that make sub-nanosecond M-CARS microspectroscopy particularly useful to investigate the dynamics of living processes by mapping the spatial distribution of different chemical specimens within biological samples.

Therefore, the electro-optical pump-probe system presented in this thesis can represent a very innovating and useful device for bioelectromagnetic investigations, potentially permitting high-resolution real-time imaging at molecular level. Indeed, M-CARS imaging could probably bring further advances in understanding how ultrashort electric fields interact with living cells.

The thesis is structured as followings:

Chapters 1 and 2 refer to the **general context**, bioelectromagnetics and nonlinear optics respectively, of the project and to the **state-of-the-art** of the current advancements both in

ultrashort pulsed electric field exposure systems for microscopy, and in laser sources specifically designed for M-CARS microspectroscopy.

In **Chapter 3** the **whole electro-optical system** is described and characterized, highlighting in detail the specifications and the performances of the electrical pulse generator and the M-CARS laser source.

Finally, in **Chapter 4** is introduced a **further subnanosecond M-CARS laser source** in which the imaging is made faster by increasing the laser repetition rate. The use of a microchip laser source and a fiber amplifier can provide an original alternative in order to realise a compact high repetition rate source for M-CARS experiments. Then, in Chapter 4 a detailed **analysis in time and spectral domain of that unconventional compact source** is presented.

Chapter 1- Bioeffects of pulsed electric fields (PEFs)

An electric field of sufficient magnitude induces nonlinear changes in cell membranes, firstly in plasma membrane [1]. Due to the plasma membrane selectivity, under physiological conditions the value of the TMP is constant (Figure 1-1(a)). If an external, high enough electric field is applied on the cell (Figure 1-1(b)), first the polar molecule and the water dipoles, surrounding the cell membrane, orient their polarity following the electric field (Figure 1-1(c)). Next, after the time necessary for the dipole relaxation to occur (a few ns) ions move towards the cell interface (Figure 1-1(d)), whit the accumulation of ions along cell membrane the TMP increases [25]. Moreover, if the value of TMP is maintained above a certain threshold long enough compared to the plasma membrane charging time (generally hundreds of ns), some modifications occurs in the membrane, changing its permeability rather permanently. The nature of these modifications is not yet well known. Some researchers explain the change in membrane permeability with the formations of actual pores through the membrane, justifying in this way the widely used term "electroporation" (Figure 1-1(e)). Other researchers refer to this phenomenon as "electropermeabilization", that more generally states the only detectable parameters of membrane modifications: the changes of TMP and permeability.

The effect of intense pulsed electric fields on biological cells and tissues has been the topic of research since the late 1950s. First reports on the reversible breakdown of the cell membranes and the increase of plasma membrane permeability appeared in 1958 and 1972, as respectively in [26], [27].

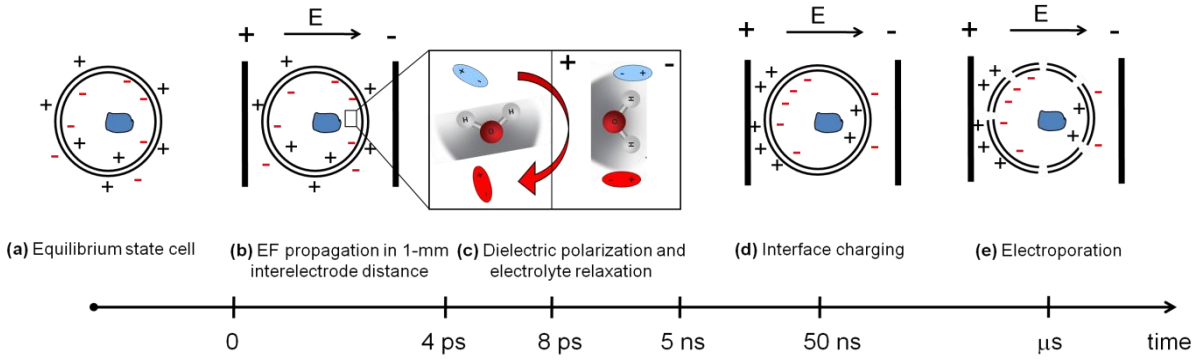

Figure 1-1: *Schematic representation of the different phases of the perturbation induced on the biological cell membrane by an external electric field. (a) Cell in the resting state; (b) during the first 4 ps of the exposure, the electric field propagates between the electrodes; (c) the electrophoretic movement of ions and water dipoles occurs in the first few nanoseconds; (d) finally, the charge displacement starts. (e) After several microseconds the electroporation occurs.*

Since the effects induced by electric field mainly depend on the duration of applied pulses compared to the charging time of the plasma membrane [28], in this thesis we will refer to the electric pulses as:

long pulses (> hundreds ns, ms, µs): if their duration is longer than the charging time of the plasma membrane;

short pulses (from tens ns to 100 ns): if their duration is shorter than the plasma membrane charging time;

ultra-short pulses (sub-ns or ps): if their duration is < 10 ns.

When long pulses are applied "classical electroporation" studies are performed. In this case, amplitudes from several hundreds of V/cm to several kV/cm are employed, giving rise to micrometric pores and to the transfer of large molecule, as DNA. Currently, the classical electroporation finds application in different domains: as in medical applications (e.g. electrochemotherapy [5], cell fusion [29], DNA transfer [6], [7]), and industrial processes (e.g. bacterial decontamination [2]).

More recently, the use of short electric pulse has opened a new field of research specifically devoted to investigate and comprehend the bioeffects of nanosecond pulsed electric field (nsPEF) [30–34]. Indeed, by reducing the duration of electrical pulses from microsecond to nanosecond range and increasing the field intensity up to the MV/m, the electric field-cell interactions shift increasingly their effectiveness from the plasma membrane to the subcellular structures (i.e., cytoskeleton, endoplasmic reticulum, Golgi apparatus, nuclear membrane; Figure 1-2(a)). These "intracellular electroeffects" seem to be similar to that occurring on plasma membrane, and have additional effects as the so called "secondary effects", including modified cell functions, and apoptosis (programmed cell death) [34–36]. Since these effects are cell specific, they may allow targeting certain cell type in mixed population, permitting to apply electric pulses to kill the cells without the use of drugs as in standard electrochemotherapy.

The next frontier of bioelectric research is represented by the application of subnanosecond and picoseconds pulses to cells and tissues, with intensity of the order of tens of MV/m. Due to their potential powerful applications for "intracellular manipulation", a clear understanding of the physical and structural mechanisms beyond the membrane and subcellular structures destabilization is of great interest. This aspect is at the moment lack in the literature dealing with ultra-short pulses.

In this context, the present work addresses the thrilling challenge to provide a complete and performing system capable to improve the knowledge in the short and ultrashort regime of electrical stimulation. Indeed, the developed system is able to detect and visualize the phenomena characterized by temporal dynamics of the order of ps and ns (Figure 1-1). Only by

observing these physical mechanisms we will get further insight to the understanding of the nature of the cell membrane perturbation.

The first chapter introduces the conceptual background and the state-of-the-art of the electropermeabilization studies, useful for understanding the main motivations of my PhD work. Therefore, cell membrane characteristics both from a biological and electrical point of view are first presented. Then, the PEF-induced biological effects and main applications are introduced. Finally, different types of electric field exposure systems and the most widely used electroporation detection techniques are described.

1.1 Overview of biological cell

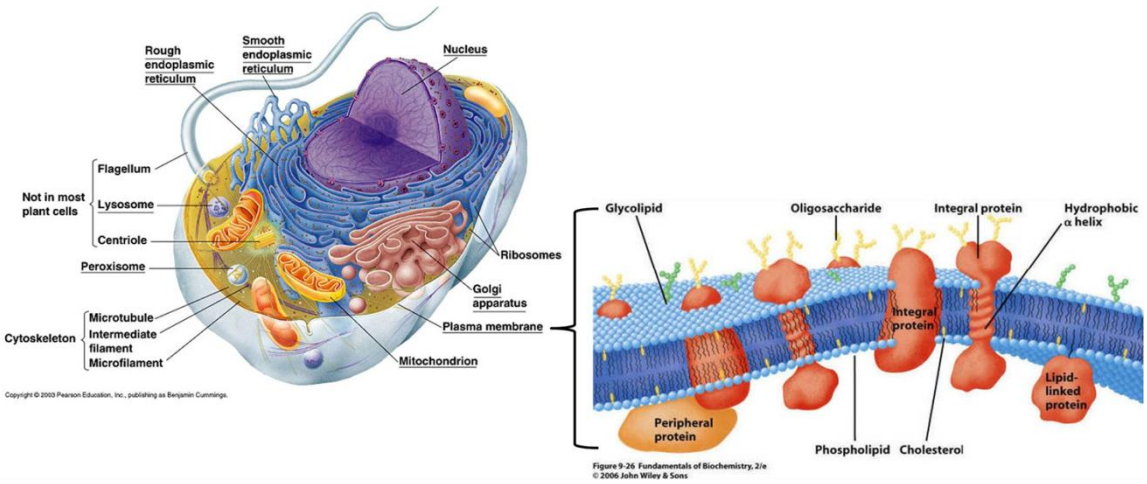

Figure 1-2: *(a) Biological cell and (b) plasma membrane structure.*

1.1.1 Biological cell description

As well known, a typical "cell system" is composed by an interior environment, the cytoplasm, in which different organelles (e.g. lysosomes, mitochondria, nucleus...) are in suspension; it is surrounded by the plasma membrane that represents the physical barrier between the interior and exterior of the cell. A typical cell diameter is in the range 8-100 μm and the membrane thickness varies from 5 nm to 10 nm, depending on cell type [37]. The plasma membrane represents both a mechanical support and a protection of the cell. It consists of a phospholipid bilayer (Figure 1-3) composed of hydrophilic heads (phosphate group) oriented towards the outside of the membrane and hydrophobic tails (fat acid chain) at the interior.

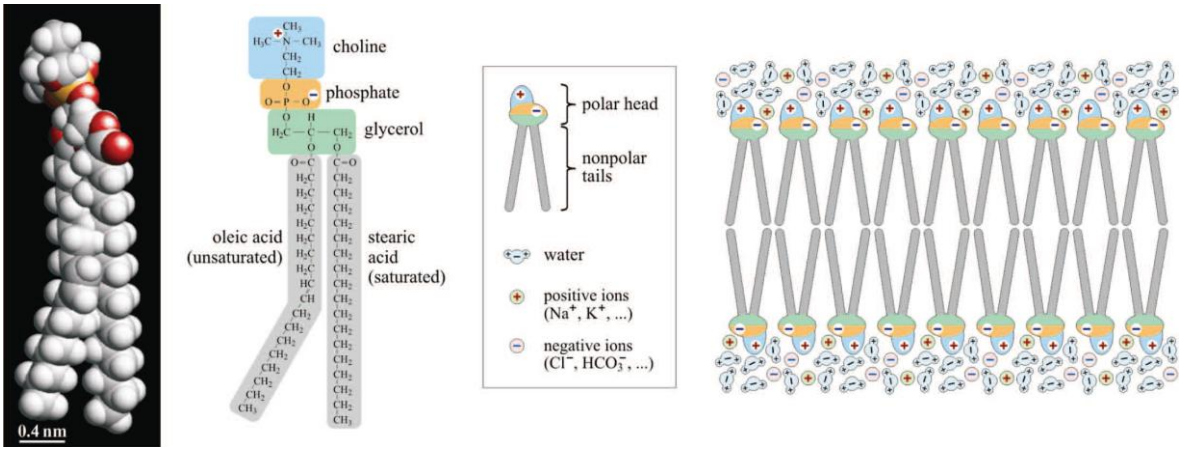

Figure 1-3: *From left to right: 3D model and structural formula of a phospholipid; schematic representation of a bilayer of such lipids in an aqueous electrolyte solution* **[11]**.

Some proteins, known as transmembrane proteins (Figure 1-2(b)), are embedded in the bilayer and represent channel through whom ions pass from inside to outside (and vice versa) of the cell, controlling the selective permeability and maintaining the membrane potential constant. The subcellular membrane, e.g. the nuclear membrane, has the same structure of the plasma membrane and the function of regulating ions between the cytoplasm and the subcellular organelle.

TMP, as said before, is the difference in voltage between the interior and exterior of the cell membrane voltage $\left(V_{\text{interior}} - V_{exterior}\right)$. It arises from the interactions of ion channels and ion pumps embedded in the membrane (transmembrane protein), which produce different concentrations of electrically charged ions on the intracellular and extracellular sides of the membrane by a "gating" mechanism (Figure 1-4).

These ion channels can be ligand-dependent or voltage-dependent (i.e. in the case of excitable cells, such as neurons or muscle cells). In the first case, their conductance depends, directly or indirectly, on a chemical messenger. For voltage-dependent channel the conductance depends on the transmembrane potential.

At the resting state the membrane potential ranges from -40 to -80 mV. This value can be calculated by using the following expression, known as Goldman equation:

$$V_m = \frac{RT}{F} \ln\left(\frac{P_k\left[K^+\right]_{out} + P_{Na}\left[Na^+\right]_{out} + P_{Cl}\left[Cl^-\right]_{in}}{P_k\left[K^+\right]_{in} + P_{Na}\left[Na^+\right]_{in} + P_{Cl}\left[Cl^-\right]_{out}} \right) \quad \textbf{(1)}$$

where R is the universal gas constant, T is the absolute temperature, F is the Faraday constant, $\left[X^+\right]_{out}$ is the extracellular concentration of ion X, $\left[X^+\right]_{in}$ is the intracellular concentration of ion X, P_x stands for the relative permeability of the ion type X.

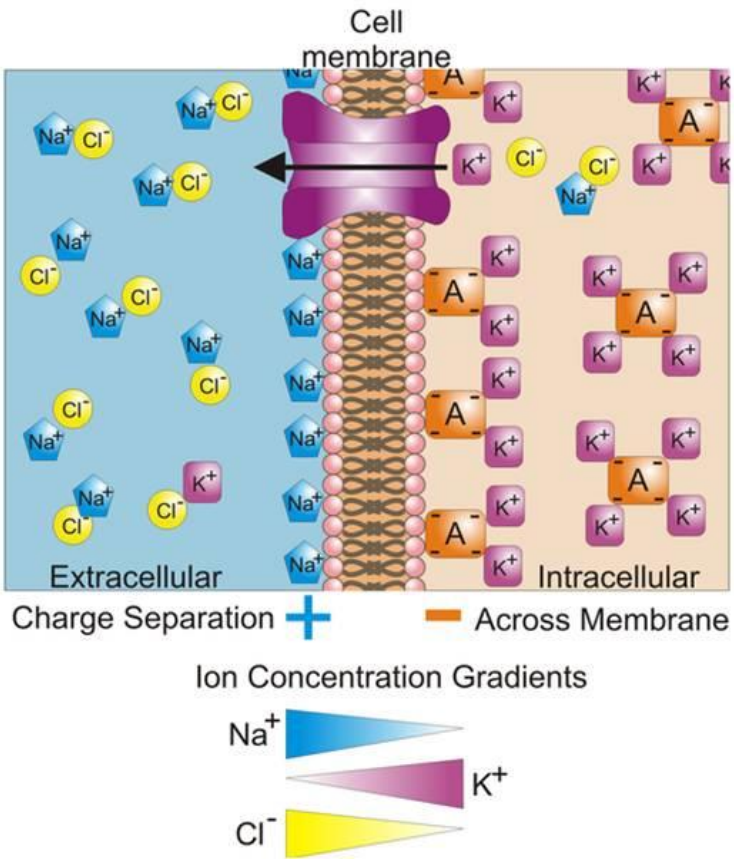

Figure 1-4: *Schematic representation of different ion concentrations on the opposite sides of the plasma membrane producing the TMP*.

1.1.2 Biological cell: from the reality to the electric models

From an electrical point of view, the whole cell can be represented through a simple spherical model in which the cytoplasm is the conductive medium and the membrane is the insulator (Figure 1-5(a)). The cell electrical properties are expressed by the conductivity σ_j and the permittivity ε_j (*j=in*, *m*, and *out*, for cytoplasm, cell membrane and external suspension, respectively). Typical values for σ_j and ε_j are reported in Table 1. The plasma membrane functions as a combined resistor and capacitor (Figure 1-5 (b)). The high resistive behaviour arises from the fact that the membrane impedes the movement of charges across it. The capacitance is due to the fact that the lipid bilayer is so thin that an accumulation of charged particles on one side gives rise to an electrical force that pulls oppositely-charged particles on the other side. The capacitance of the membrane is relatively affected by the molecules that are embedded in it, so its value is more or less invariant and it is estimated to be about 1 $\mu F/cm^2$. The resistance, instead, is highly variable, due to the conductance of alternative pathways provided by embedded molecules, and it is larger than the cytoplasm resistivity (on the order of 100 $\Omega \cdot cm$ or even higher).

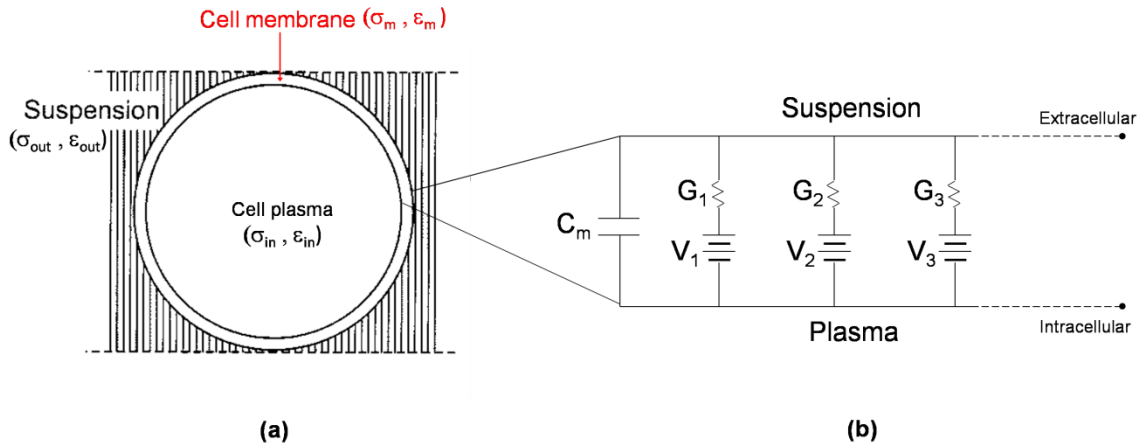

Figure 1-5: *(a) Spherical model of cell considering a conducting medium at the interior (the plasma) surrounded by a dielectric layer (cell membrane). (b) Equivalent circuit of plasma membrane with C_m, fixed capacitance, in parallel with some batteries (ion channel voltages) in series with ion channel conductance.*

Table 1. Characteristic electric values of cell conductivity and cell permittivity.

	Conductivity (S/m)		Permittivity (F/m)
σ_{out}	0.14 – 1.2	ε_{out}	67 - 80
σ_m	$0 - 10^{-5}$	ε_m	2 - 12
σ_{in}	0.13 – 1.2	ε_{in}	60 - 80

Therefore, the plasma membrane can be represented by an equivalent circuit composed by a capacitance C_m in parallel with voltage-dependent ionic channel each represented by a series of conductance G_i (i=1,2…) and a voltage sources V_i (Figure 1-5(b)) [38]. The time constant for the charging process depends on the cell size and conductivity of the suspension media. A typical charging time for a mammalian cell of 10 μm of diameter in suspension is 75 ns (it reaches 100-300 ns in tissue) [35]. The voltage of each ionic pathway at any point in time is determined by the concentrations of ion on each side of the membrane (see (1)) and the conductance is determined by the state of all ion channels that are potentially permeable to that ion, including ligand-dependent channels, and voltage-dependent channels.

The dielectric behavior of plasma membrane is well represented in Figure 1-6, where the dielectric permittivity ε and the conductivity σ of a living yeast cell membrane are plotted as functions of the frequency [39]. At extremely low (up to hundred of kHz) frequencies the cell membrane response to the electric field is dominated by charge monuments. Then the membrane dipole orientation starts to occur. So, at higher frequencies (> 100 kHz) the dielectric permittivity dominates on the conductivity. At much higher frequencies (100 MHz) the dipoles

cannot follow the faster electric field changes and the dielectric relaxation of the membrane structure appears.

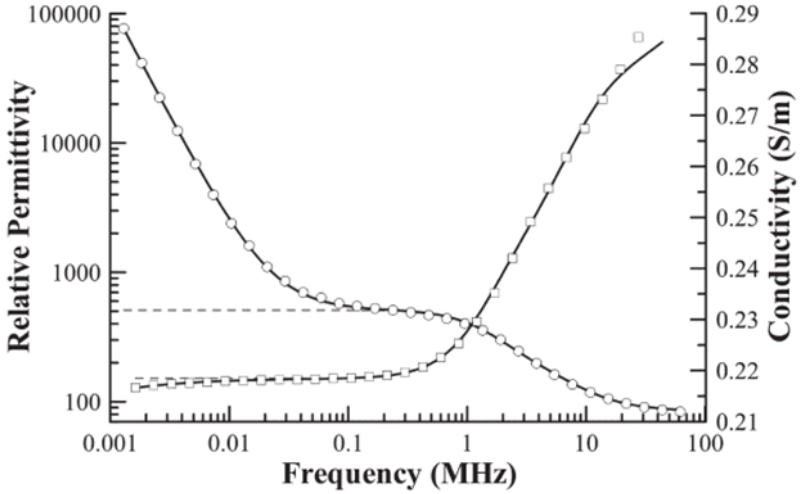

Figure 1-6: Typical plots of relative permittivity (circles) and conductivity (squares) versus frequency for yeast cells [39].

The previous description of the cell from a biological and an electrical point of view allows us to better understand how an exogenous electric field can perturb the cell and its environment. In particular, the dissipative and dielectric nature of the cell membrane is the key to understand the importance of the duration of the applied electric pulses, and their different spectral content, in the electropermeabilization processes. In the next section, the electropermeabilization phenomenon is discussed with particular emphasis on the differences between bioeffects induced by long and short pulses and their main biomedical applications.

1.2 Primary effects of PEFs

1.2.1 The "classical electroporation"

The classical electroporation, as said in the introduction of this chapter, refers to the creation of membrane-spanning aqueous pathways across the lipid bilayer after application of an exogenous pulsed electric field, allowing idrophilic and rather large molecules to pass through the membrane. This phenomenon occurs in regions of the plasma membrane where the local potential, inducted by the applied electric field, is above a certain threshold that depends on several parameters, like the cell type (size, shape, physiological or pathological state), electric field exposure configuration (electrode geometry, *in vitro* or *in vivo*…) and pulse parameters [13], [40]. If the applied electric pulse is neither too long nor too intense the electroporation is reversible, exploiting the relatively weak nature of the phospholipid bilayer

hydrophobic/hydrophilic interactions and its ability to reassemble spontaneously after disturbance. On the contrary, if an electric field above a critical value for that cell is applied, the fast electric shock may definitely disrupt areas of the membrane, leading to the cell death and necrosis of the tissue (irreversible electroporation). Thus, the magnitude of electric field should be high enough to cause reversible membrane permeabilization, but lower than the value causing irreversible damages.

Classical electroporation uses field strengths of several hundred volts per centimeter for microsecond to millisecond durations to allow passage of normally non-permeable molecules across the plasma membrane with quite large dimentions. The electric potential across the membrane of the cell simultaneously rises by about 0.5-1.0 V so that charged molecules (such as DNA) are driven across the membrane through the pores.

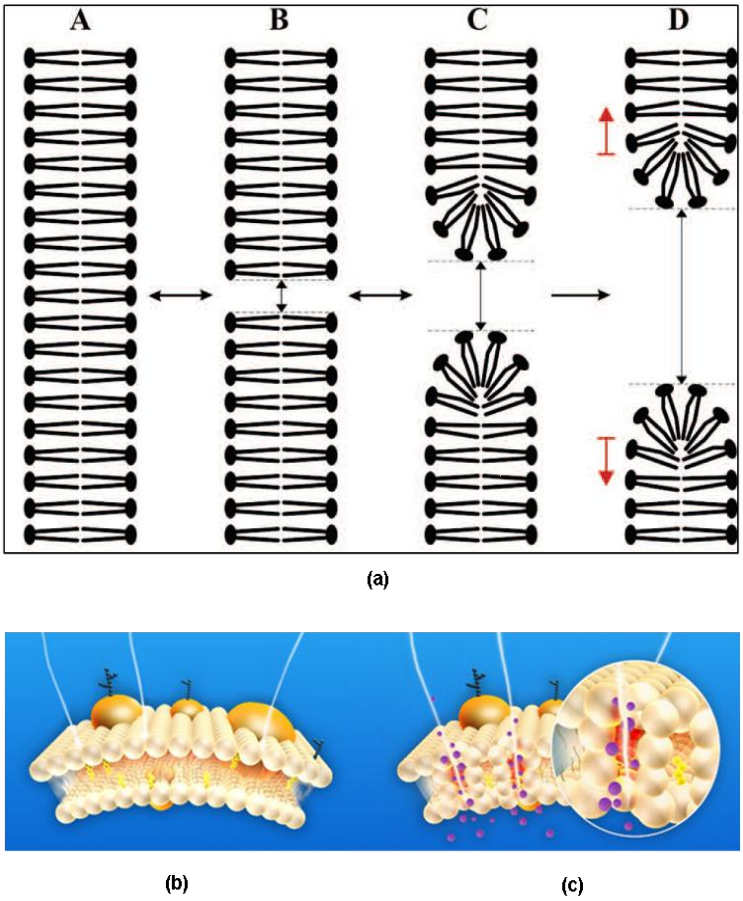

Figure 1-7: *(a) Phases of pore formation dynamic: bilayer without pores (A), with a hydrophobic pore (B), its reversible transition into a metastable hydrophiolic pore (C), and its irreversible transition into a unstable self-expanding hydrophilic pore (D)* **[11]**. *3D schematic representation of (b) the intact plasma membrane and (c) the electroporated one* **[37]**.

1.2.2 Classical electroporation applications

Classical electroporation is widely used in many areas of molecular biology research and in the medical area (Figure 1-8). For example, reversible electroporation is used in electrochemoterapy permitting to directly introduce antitumor drug in cancer cell, avoiding in this way the systemic effects of the ordinary chemotherapy [3], [5]. It also permits introducing DNA fragments or genetic sequences into the cell (DNA transfection, gene therapy). Moreover, if the cells are close enough, the permeabilization of cell membrane can induce cell fusion. Finally, irreversible electroporation leads to the destruction of cell membrane with consequent cell death (electrosterilization and cellular ablation). Indeed, controlled electric field distribution in the tissue is able to locally induce thermal effects without damaging the healthy tissue. These irreversible process has been proposed as a minimally invasive surgical procedure to ablate the cancerous tissue without the use of adjuvant drugs [41].

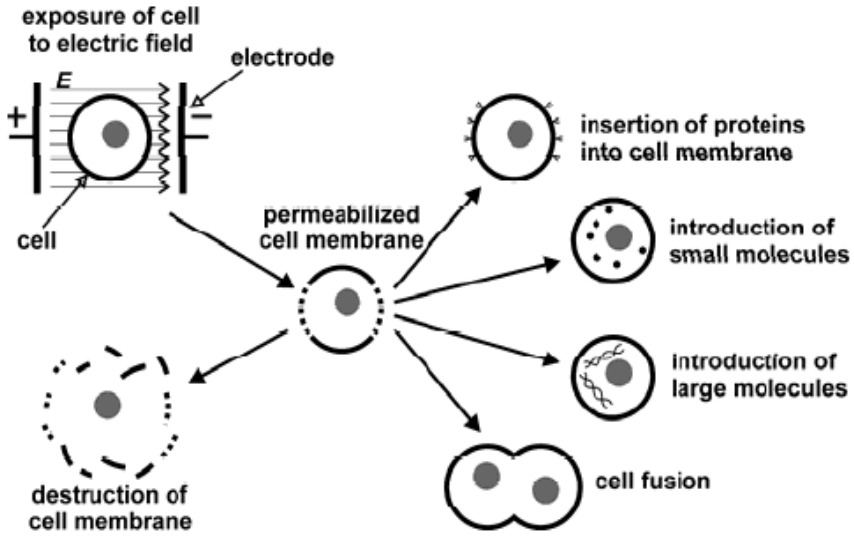

Figure 1-8: *Principle of electroporation and some applications. Cell is exposed to a large enough electric field E, inducing membrane permeabilization. In this way, it's possible to introduce polar or large molecules (like DNA and proteins) into the cell, to induce cell fusion or cell death by membrane disruption* **[42]**.

The main applications of electroporation are described below:

- **Electrotransfection** is likely the most widespread application using electroporation. The electropermeabilization of the cell membrane can allow vectors, containing important genes or DNA, to be transported across the skin and into the target tissue. Once incorporated into the cells of the body, the protein produced from this gene could replace a defective one and thus treat a genetic disorder. In Figure 1-9 the DNA transfer process is described [43].

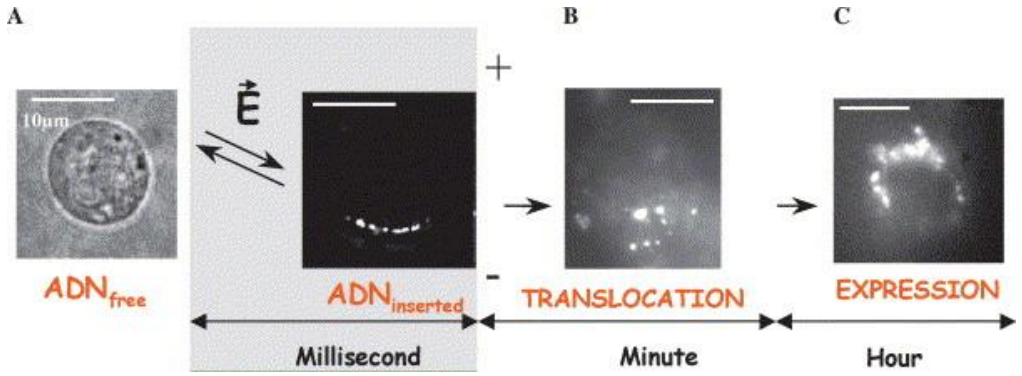

Figure 1-9: *DNA transfer steps: A, in the first µs of electric field application the electropermeabilization takes place and after a few ms the DNA is electrophoretically driven into contact with cell surface; B, a metastable complex forms between the plasmid and the electropermeabilized patch of membrane. After few minutes DNA left the complex and diffused in the cytoplasm. C, a small fraction crossed the nuclear membrane to be expressed* **[43]**.

- **Trans-dermal Drug Delivery**: as electroporation causes temporary pores in plasma membranes, studies suggest that similar pores could be formed in lipid bilayers of the stratum corneum (the outermost dead layer of skin). These pores could allow drugs to pass through the skin in order to target tissues. This method of drug delivery would be more pleasant than injection for the patient (not requiring a needle) and could avoid the problems of improper absorption or degradation of oral medication in the digestive system [9].

- **Cancer Tumor Electrochemotherapy:** scientists are investigating the potential of electroporation to increase the effectiveness of chemotherapy. As in electroporation for DNA - transfer, the applied electrical pulse would disrupt the membrane of the tumor cell and increase the amount of drug delivered to the site. Some studies have showed that increased tumor reduction is seen when this method is applied to cancerous cells in animal model systems [3], [5].

Figure 1-10: *Tumor nodules of breast chest wall recurrence were treated by electrochemotherapy. The drug was injected intratumorally and thereafter electric pulses were delivered by plate electrodes. Several runs of electric pulses were delivered so that the whole tumor area was electroporated* **[3]**.

For optimal efficiency of such applications, one must select the appropriate duration and amplitude of the applied electric pulses for each specific target cell. The typical values used for each application are reported in Table 2.

Table 2. Typical duration-strength pairs of PEF used in the main electroporation applications.

APPLICATION	PULSE DURATION	PEF INTENSITY	Reference
Electrotransfer	5 to 10 ms	0.5 to 0.8 kV/cm	[6], [7]
Cell fusion	10 µs	~4 kV/cm	[29]
Trans-dermal Drug Delivery	100 ms (6/8 pulses@1Hz)	1.3 kV/cm	[9]
Electrochemotherapy	100 ms	1.3 kV/cm	[3], [5]

1.2.3 Shorter pulse-induced electroporation

"Nanoelectroporation" refers to the application of nanosecond pulsed electric fields (nsPEFs), using much higher field strengths of several hundred kV/cm for durations shorter than the charging time of the plasma membrane [35]. For a comparison, the rise time of classical electroporation pulses alone is often longer than the entire pulse duration of nsPEFs. For long pulse durations, ions accumulate along the plasma membrane, and a counter-field develops inside the cell that effectively shields the organelles from further exposure to the applied electric field. As a result, only the outer membrane is affected by the prolonged exposure and pores form once a cell-characteristic threshold voltage is reached [44] (Figure 1-11(a)). Conversely, with the short duration nsPEF, the membrane capacitance is completely short-circuited and the applied electric field penetrates into the cell and organelle membranes will be affected in the same way as the outer cell membrane (Figure 1-11(b)) [45].

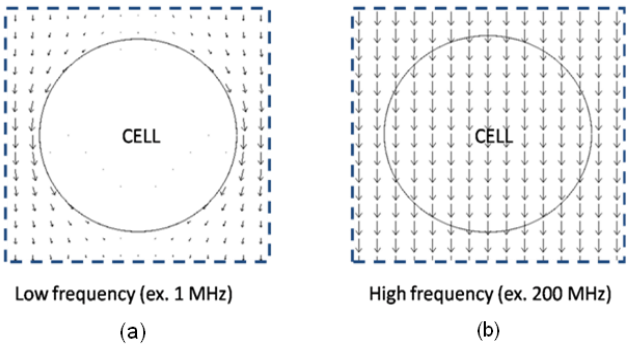

Figure 1-11: *Simulated distribution of applied electric field lines at the suspension/cell membrane interface* **[1]**.

Considering the high electric field strengths applied with nsPEFs, transmembrane voltages reach values of more than 1 V during the exposure and pore formation is also likely along internal membranes [46]. In addition to this direct effect on membrane structure, the intense fields affect voltage-gated channels and other protein structures in the membrane [47], [48]. Ca^{2+} stores, such as in the endoplasmic reticulum (ER) and mitochondria, are presumably targeted by the same mechanisms, causing the release of Ca^{2+} into the cytosol [34], [49]. Therefore, changes in $\left[Ca^{2+}\right]_i$ seem to be among the first physiological responses of the cell to nsPEFs.

Moreover, the application of shorter electric pulses may improve the DNA transfer technique to nucleous. Generally, the transport of material through the membrane during the time of electropermeabilization is relatively non-specific. This may result in an ion imbalance that could later leads to improper cell function and cell death. This limitation may be overcame with the application of short pulses (pulse durations of 1-100 ns; electric field amplitudes up to 300 kV/cm). Such a pulses with a duration shorter than membrane charging time may be able to impose selective field effects in a particular population of cells, making electroporation more specific. In [50], for example, the authors show preferential poration of intracellular membranes as well as selective electroporation of vesicles from a mixture of similar size distribution. In this case the different charging time of the vesicle membrane capacitance was used as a means to discriminate and select the electroporation target.

1.2.4 The impact of the pulse parameters on electroporation

The dynamics of transmembrane voltage induced by the applied electric field can be evaluated by a the Laplace's equation even in time domain [51]:

$$\Delta\Phi_m(t) = 1.5rE\cos\vartheta\left[1-\exp\left(-\frac{t}{\tau}\right)\right] \quad \textbf{(2)}$$

where 1.5 is a factor reflecting the electrical and geometrical properties of the cell when one assumes the membrane conductivity much smaller than the plasma and suspension conductivities and a spherical cell. In (2) r is the cell radius, E is the strength of the electric field (which has to be DC for this expression to be valid), θ is the angle between the normal to the membrane and the direction of the field, and τ is the charging time constant of the membrane. Apart from duration and amplitude, also shape, number and repetition rate of the pulses may have a relevant role in the electropermeabilization.

For a given pulse duration, the shape of an electric pulse is directly related to its rise and fall time (square, triangular or Gaussian pulse) and to the polarity of electric field (unipolar or bipolar pulse [52]). The time during which the pulse amplitude exceeds the threshold necessary for electroporation is important in order to determine the efficiency of the process. While for the unipolar pulse rise and fall time seem not play a detectable role, bipolar symmetrical pulse application decreases the amplitude required for the electropermeabilization and increases the permealized area of the membrane in comparison with unipolar pulses of the same duration [13]. Moreover, each temporal shape has a different spectral profile that represents the energy distribution in frequency. Since the electric properties of the cell depends on the frequency (see section 1.2), the cell response is strongly dependent on the shape of pulse temporal profile and its spectrum. Figure 1-12 shows the comparison between the spectral content of (a) bipolar and (b) unipolar pulse. Despite the energy content is the same, in the case of bipolar pulse this energy is at high frequency, where the cell is transparent to the electric field (c). Instead, when the energy is concentrated at lower frequencies, the plasma membrane shields the interior of the cell.

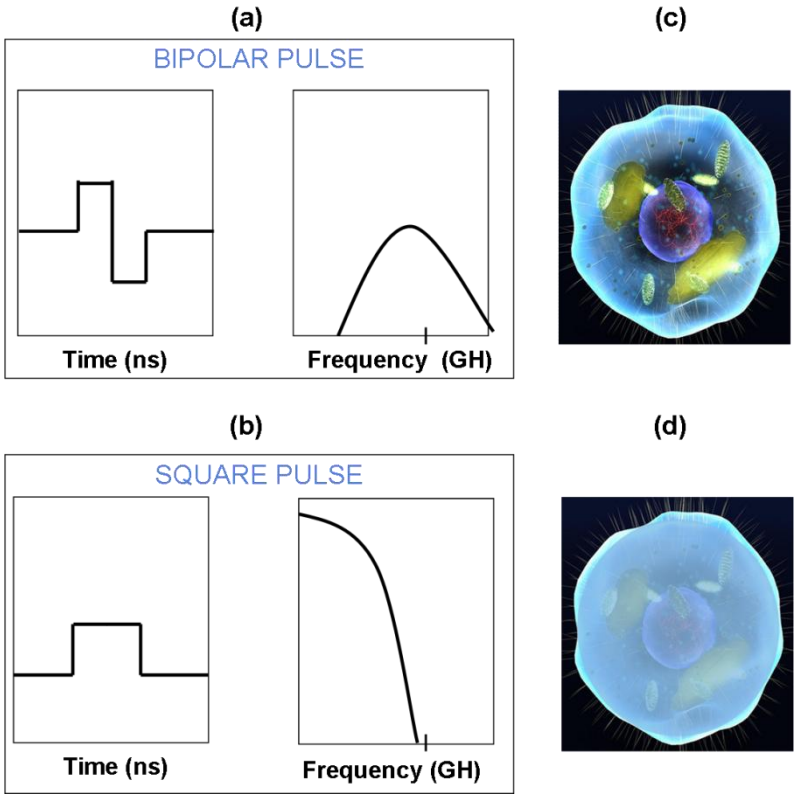

Figure 1-12: *Temporal and spectral profile of the bipolar (a) and square (b) pulses. (c) Biological cell is "transparent" to the high-frequencies components of bipolar pulse, while (d) it is "opaque" to the low-frequencies components of the square pulse.*

Several scientific works have shown that even a single pulse of suitable duration and intensity induces some effects on cell membranes [46], [47], [50], [53]; nevertheless, the most of electroporation studies consider the application of a train of pulses.

It would seem that the same elecropermeabilization efficiency can be obtained with both a high number of the pulses of weak intensity (hundreds of V/cm) and a lower number of pulses of higher intensity (a few kV/cm). However, an interesting study has found a correlation between the number of applied pulses and the electroporation efficiency [54]. In such study, the cell viability has been estimated in presence of different amount of an antitumor drug. The obtained results showed that a higher number of pulses for a reduction of the external drug concentration was necessary to kill the cell. In that case, the hypothesis was that an increased number of pulses might create additional or larger pores in the membrane. This hypothesis confirms the previous studies in which the number of the pulses was associated to the density and/or the size of the electropores [55], and an increasing in permeabilization of the mammalian cell membrane was observed [56].

The repetition rate of the applied pulses seems to have less influence on the efficiency of the electroporation. It may have a role in the determination of the voltage threshold for pore formation. In a study of Pucihar *et al*. [57] different repetition rates have been applied keeping duration, amplitude and number of pulses constant. They showed that the increase of pulse repetition rate didn't significantly reduce the peak of the antitumor drug uptake into the cell, but higher field strengths were required at higher repetition frequency. The study also highlighted the role of electric pulse repetition rate in improving elettrochemotherapy. Indeed, with higher pulse frequencies the therapy was better accepted by the patients because of a reduction of number of muscle contractions under electric pulse delivery.

1.2.5 Biological target parameters influencing electroporation

Current bioelectromagnetic researches are involved in understanding the bioeffects of the electric field at cellular level (human Jurkat T lymphoblasts and rat glioma C6 cells [33], [58], platelets [59], skin cells [60], human blood cells [39], [50]).

Such effects being specific for each cellular type permit to select the biological target in a heterogeneous population of cells [61], [62], useful for electrochemotherapy application, as we mentioned above. Therefore, the cell parameters such as the size, shape and state (physiological or pathological) have to be considered as well.

The size of the cell influences the interactions between electric field and biological target mainly in two ways [33]. Larger cell has a larger radius term r in the equation (1), thus concentrate the external field more than a smaller cell. As consequence, the transmembrane voltage is higher.
A larger structure will also have a larger capacitance (because of increased surface area) and thus will charge more slowly (larger τ_m) than a smaller structure.

The shape is another important element which influences the interaction, but the most part of scientific papers treats the simplest cell model, the homogeneous spherical-shell model as presented on Figure 1-5(a). This model is not a direct physical representation of cellular structure which is more complex, as we can see in Figure 1-2.
Cell model with three different shapes (spheroidal, prolate spheroid, oblate spheroid) is analyzed in a study of Hu and Joshi [63]. They have observed that electroporation occurs in all the cases but the prolate cells are more difficult to electroporate than oblate spheroids, for example.
Concerning the state of the cell, recent studies have compared different responses of normal and tumor cells [33], [58], [60], [64–66]. We have seen that the cell properties, such as conductivity, permittivity and membrane thickness play an important role in electroporation. It is well known that normal and malignant cells have different dielectric and geometric properties [64]. For example, rat glioma cells are more resistant to pulse exposure than normal Jurkat cells. The former require between 200 and 400 pulses at 40 kV/cm in amplitude and 10 ns in duration, a dose immediately lethal for Jurkat cells [58].

1.3 Secondary effects of PEFs

Whereas primary effects deal with structural changes of the cell membrane and can occur both with long and short pulse application, secondary effects represent changes in cell functions in response to short pulses. Dependent on the electropulsation conditions, various effects have been observed:

- intracellular calcium release [49],[34]
- externalization of phosphatidylserine residues [53]
- caspase activation [33]
- necrosis or apoptosis arise [33], [36].

The first three phenomena can be seen as initiation events of apoptosis. Apoptosis is the process of programmed cell death. Using this process cells eliminate efficiently themselves from a tissue when they are no longer functional or necessary. Apoptosis differs from necrosis in that it does not cause inflammation or damage to surrounding healthy cells. And, so, it may be an approach to destroy tumor cells [31], [33], [36]. Following to an apoptosis-induced stimulus, the death

process starts. Apoptotic death of human Jurkat cell, for example, has been observed with pulses of 10 ns in duration and up to 300 kV/cm in amplitude [36]. For longer pulses and electric field amplitude lower than the value required for apoptosis (more than 30 ns in duration and up to 50 kV/cm in amplitude [53], [58]), phosphatidylserine externalization occurs, and this can be interpreted as an apoptotic stimulus. In fact, during the initial phase of apoptosis the plasma membrane becomes marked by phosphatidylserine molecules on its surface. Another phenomenon involved in apoptosis signalling is the increase in intracellular calcium, stored in endoplasmic reticulum compartments and mitochondria, this phenomenon is observed for pulses with duration of 300 ns and amplitude of 12 kV/cm [49].

It is clear that the PEFs can induce several phenomena on the biological cells, depending on numerous parameters, like the intensity and duration of the applied electric pulses as well as the exposed cell type. A relevant role is played also by the exposure system used for the PEF application. It must to be suitable for the specific purpose of the study or application, and, thus, their design and fabrication required a detailed characterization. The state-of-the-art regarding the mainly used exposure system for electroporation study is reported below. The characterization of the particular exposure system typology used in this thesis work is described in the first part of Chapter 3.

1.4 Exposure system

An exposure system is composed of an electrical pulse generator and a delivery device that applies electrical pulses to biological sample and represents the load of the generator (Figure 1-13). In this section, different types of generators and delivery devices, suitable for biological applications, are presented. In the last section the most widespread electroporation detection techniques are introduced.

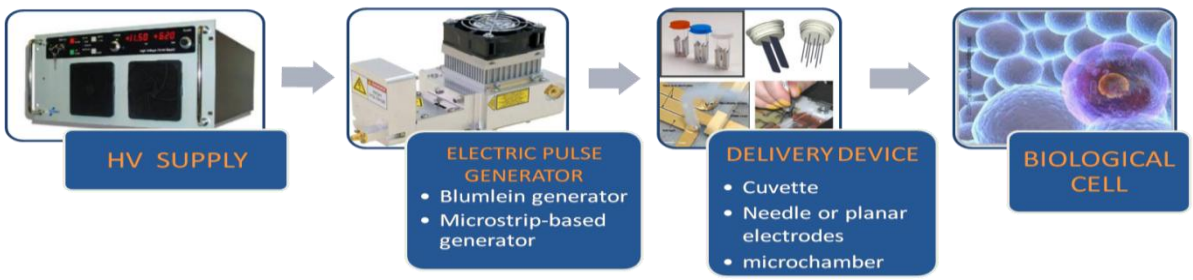

Figure 1-13: Block *diagram representing the main components and typologies of an exposure system for electroporation studies.*

1.4.1 Electrical pulse generators

A pulse generator is an electronic or optoelectronic system delivering pulses voltage of different amplitudes and durations. It is directly connected to the delivery device which transfers the stoked energy toward the biological medium. That transfer is realized without any losses by using a perfect impedance matching between the generator and the delivery device and between the latter and the biological sample (Figure 1-13). The generator must be adaptable to the exposure system that takes the form of a cuvette permitting to transfer energy toward several millions of cells or a microscope slide for real time images of few cells, in the most common cases. Additionally, it must allow controlling the pulses in terms of duration, shape, repetition frequency and amplitude.

Two main generator topologies are quickly described here: transmission line based on Blumlein principle and microstrip technology. Blumlein transmission line pulse generators are generally not flexible in changes of pulse parameters, but they are suited for high voltages and fast switching. The switching system can be represented by a Spark gap [67], a pressurized gas gap [46] , a solid state system as a MOSFET [9], [31], [61], [40], or a photoconductive semiconductor switch [15], [18].

Spark gap and pressurized gas gap are used for their very fast (~ 1 ns) switching time and for the flexibility in the control of the pulse amplitude by varying the gap distance.

The MOSFET technology is suitable for miniaturization on a microscope slide. It allows generating pulses with up to few kV in amplitude and a rise time of 3 ns [61], and consequently durations not shorter than tens of nanoseconds.

The photoconductive semiconductor switches are extremely versatile, being able to produce kV subnanosecond or nanosecond pulses with adjustable rise and fall time depending on the optical pulse delivered by the laser [15], [18] with lower than 1 ns switching time.

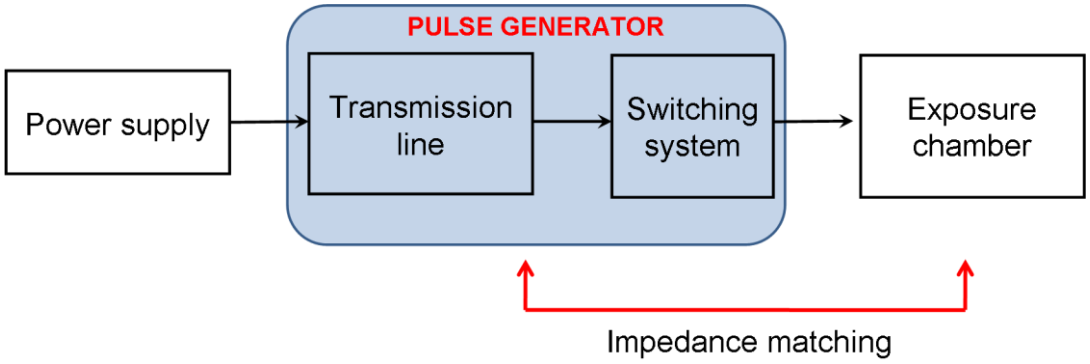

Figure 1-14: *Block diagram of the stimulation system; the pulse generator is detailed in the dark box.*

BLUMLEIN PRINCIPLE-BASED PULSE GENERATOR

The Blumlein generator is a pulse generator based on a pulse forming line (PFL) (Figure 1-15) [68]. The PFL is the simplest technique able to generate short pulses, starting from a CW high-voltage source.

The pulse width *T,* is twice the time taken by electromagnetic wave to travel the length of coaxial line in dielectric medium, filled between the coaxial conductors.

The pulse duration can be calculated by the following formula:

$$T = \frac{2L\sqrt{\varepsilon}}{c} \quad \textbf{(3)}$$

Where ε is the dielectric permittivity, c is the light velocity and L is the length of the transmission line.

The output voltage is equal to:

$$V_0 = V\frac{Z_L}{Z_L + Z_0} \quad \textbf{(4)}$$

where V is the supply voltage, Z_L and Z_0 the impedance of the load and the transmission line, respectively. The most basic configuration of a Blumlein generator consists of a transmission line connected to a high-voltage source via a high-impedance resistor that limits the bias current. After, the transmission line accumulates electric energy which is discharged into the load by a high-voltage ultrafast switch. The duration of the pulse depends on the length of the transmission line only and is, therefore, of a fixed duration.

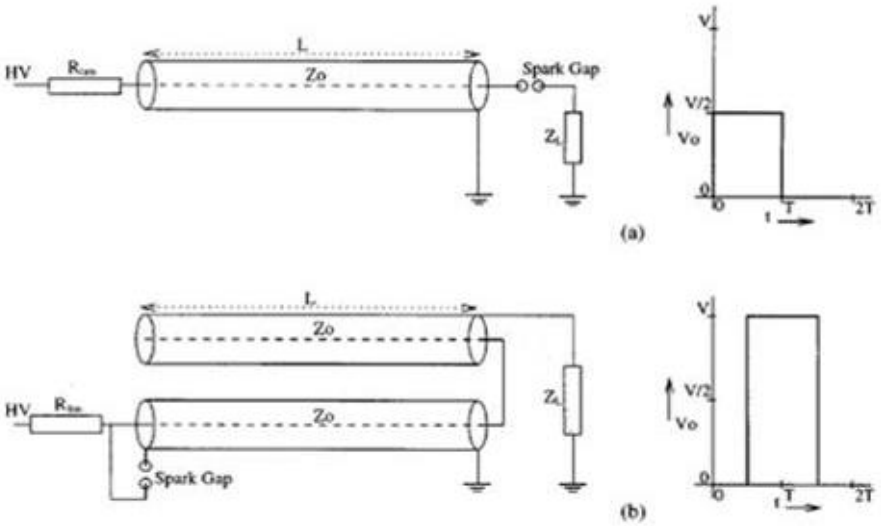

Figure 1-15: *Schematic and output waveform with matched load (a) in a simple pulse forming line and (b) in the Blumlein configuration PFL* **[68]**.

Blumlein generators have been used in various biomedical studies [61], [67–69], where the effects of high-voltage nanosecond pulses on biological cells were evaluated and have been suggested to reach the cell interior without affecting the cell plasma membrane. The main advantage of using a Blumlein generator is that it allows to generate pulses with the same amplitude of the high voltage supply. The main limit of this technology is the setting up of a synchronization system between the different switches. Moreover, this technology is limited to rise and fall times of a few nanoseconds by the switching time of the spark gaps or the high power electronic components [70]. To achieve more rapid transitions, alternative switching methods have to be employed as suggested in [71], [72], where laser triggered photoconductive switches are used on a planar microstrip forming line [15–18].

MICROSTRIP-BASED PULSE GENERATORS

The application of nsPEF during microscopy is demanding of miniaturization, pulse flexibility, and variations in load impedance. The solution that has been proposed is the microstrip-based transmission line, corresponding also to our choice in this work.

The microstrip-based transmission line is fabricated using printed circuit board (PCB) technology. It consists of a conducting strip separated from a ground plane by a dielectric layer known as the substrate. The microstrip line configuration proposed by our group [15–18] is composed of a microstripline and two photoconductive semiconductor switches (PCSS) placed at each line extremity as shown in Figure 1-16. The PCSS are triggered by the laser output. The line dimensions are chosen in order to obtain a characteristic impedance Z_0 matching with the load impedance. The microstrip technology has the advantages of being less expensive and more compact than traditional waveguide technology and provides a suitable solution for delivery pulses to systems such as microchambers.

A detailed description of such generator and of its working principle is made in Chapter 3.

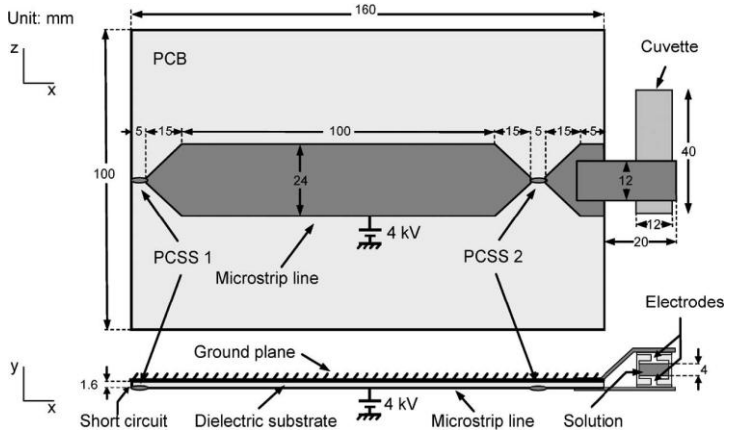

Figure 1-16: *Setup geometry of the generator and the electroporation cuvette, top and side views* **[16]**.

1.4.2 Electrical pulse delivery devices

The delivery device must be compatible with the biological sample under exposition and with the parameters of the electrical pulses. Nanosecond or sub-nanosecond pulses have a broadband spectrum and the delivery devices must allow applying pulses without spectral component losses. Moreover, in the design of any exposure chamber, impedance matching and rapid load replacement are the most significant challenges.

The most common available topologies of the delivery devices are: the biological cuvette [15], [61], [67], [68], the needle [47], [70] or planar electrodes [34], [46], [68], [73]. Recently, a topology of delivery device called "biochip", suitable for sample exposure on the microscope stage, has been proposed [74]. A similar microscope chamber is also used for electric pulse application in the system presented in this thesis.

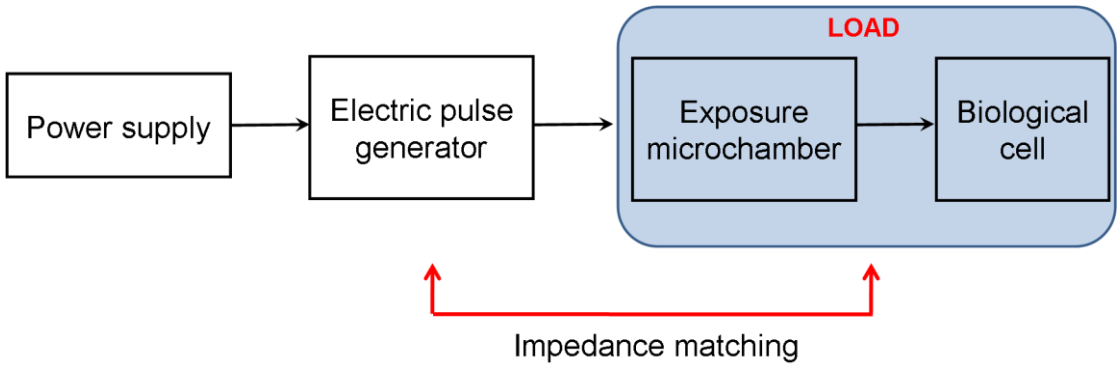

Figure 1-17: *Block diagram of the stimulation system; the load of the electric chain is detailed in the dark box.*

The biological cuvette

Among existing delivery systems, the biological cuvette is the most common one. The cuvette chamber consists in a Teflon housing containing two contact plates that are pressure mated to two opposing flat aluminium electrodes generally spaced 1, 2 or 4 mm. This design is suitable to expose cells suspended in their biological environment. The cuvette allows the application of pulses of tens ns in duration and electric field intensities from 80 to 130 kV/cm [75].

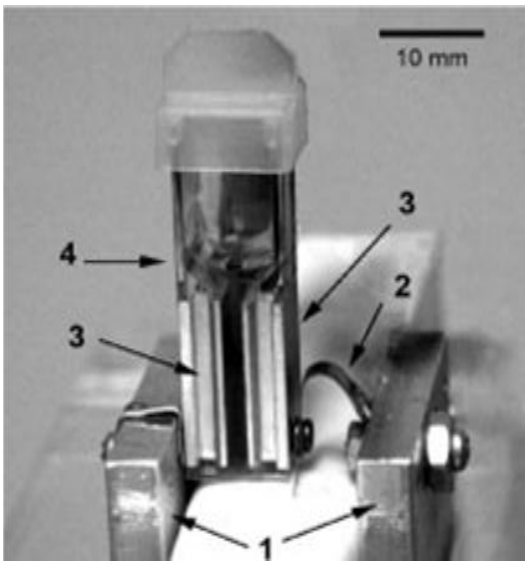

Figure 1-18: *A photo of an electroporation cuvette :1, the outer conductors connect the cuvette to the pulse generator; 2, spring cuvette holder; 3, aluminium walls of the electroporation cuvette; 4, meniscus of the cell culture sample* **[75]**.

Less and less such a system is employed in the electroporation experiments. Several studies have highlighted some relevant limits in using the biological cuvette as exposure system. First, the cuvette doesn't permit to observe cells in real time during the pulse applications which makes the study of their effects difficult. Secondly, such a system is impedance-matched up to about 30 MHz if the solution has a high conductivity [19]. Therefore, it is not suitable for exposure short or ultrashort pulses. Finally, as the electrodes are in contact with the biological medium, some electrochemical reactions occur, affecting the investigation on living sample. Among them, electrolysis of the solution, corrosion of the electrodes and introduction of small particles of the electrode material in the liquid are mainly observed [12], [76]. It seems that using symmetrical bipolar pulses instead unipolar ones would reduce the electrolytic contamination from the cuvette electrodes. Instead, the application of shorter pulses may limit the corrosion of the electrodes, and, consequently, avoid the introduction of electrode elements in the biological solution. Nevertheless, reducing the pulse duration results in a worst impedance matching. Indeed, at frequencies higher than 100 MHz the cuvette presents not negligible mismatching, as we can see in Figure 1-19 . Consequently, the biological cuvette is suitable for pulses longer than 10 ns, but is rather limited for ultra-short pulses [15].

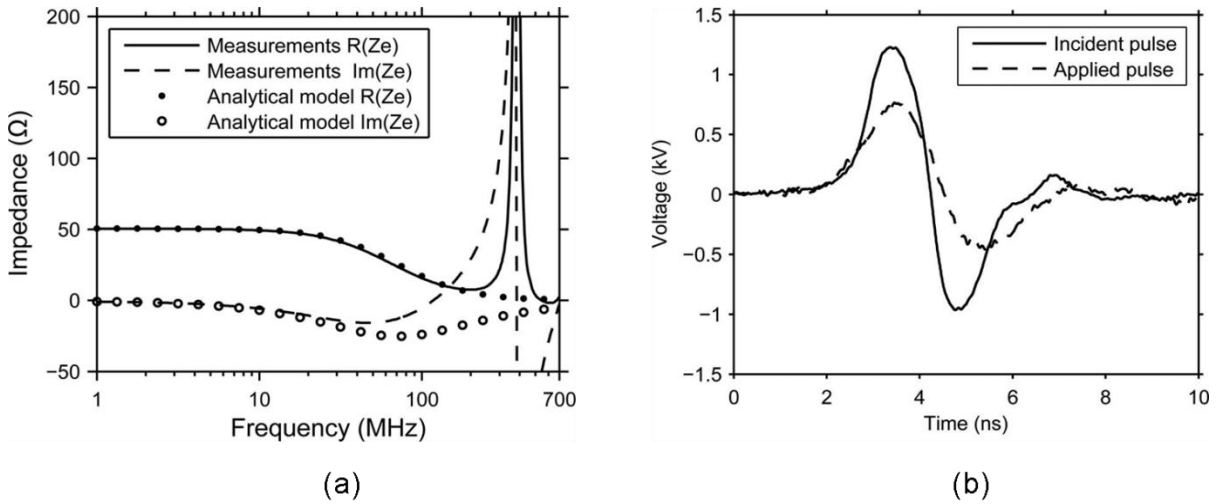

Figure 1-19: *(a) Real and imaginary parts of the cuvette impedance Z_e for solutions (σ = 0.31 S/m). Experimental and theoretical results. (b) Incident and applied voltages of the 2-ns bipolar-shape pulse* **[15]**.

Needle and planar electrodes

Needle electrodes are used for exposure of individual cells on a glass cover slip. nsPEFs are delivered to the selected cell by a pair of tungsten wire electrodes. In the paper of Pakhomov *et al.* [47] the electrodes have a diameter of 0.125 mm, and a gap between them of 0.31 mm. The electrodes are positioned with a micromanipulator at the sides of the cell, and are directly connected to a Blumlein line generator, built from two coaxial cables and matched with a 100-Ω resistor to deliver 60-ns rectangular electrical pulses (Figure 1-20(a)-(b)).

This system is able to deliver 22-24 kV/cm per 1 kV of bias voltage. The electric field does not noticeably change with a small (20-40 μm) imperfection of cell/electrodes placing. However, outside the gap between the electrodes, the electric field drops abruptly almost to zero within 50 μm. Thus, cells situated outside this distance could be considered unaffected by exposure.

Recently, Chen *et al.* [70] have presented three electrodes configuration for electromagnetic exposure of biological cells: single-needle, five-needle, and a flat-cut coaxial cable without electrodes (Figure 1-20(c)). For needle electrode delivery systems, all the electrodes are in center-symmetrical configurations. Stainless steel needles, 0.2 mm in diameter and 5 mm long are used. In the five-needle electrode design one needle is at the center, and the other four, equally spaced, are located on a 3.5 mm-diameter circle and laser-welded to the axial outer shield, and the end surface of the electrodes and the insulator are the same plane. The separating Teflon is 1.7 mm wide. The electrode assembly is fixed to an arm of the mechanical stage.

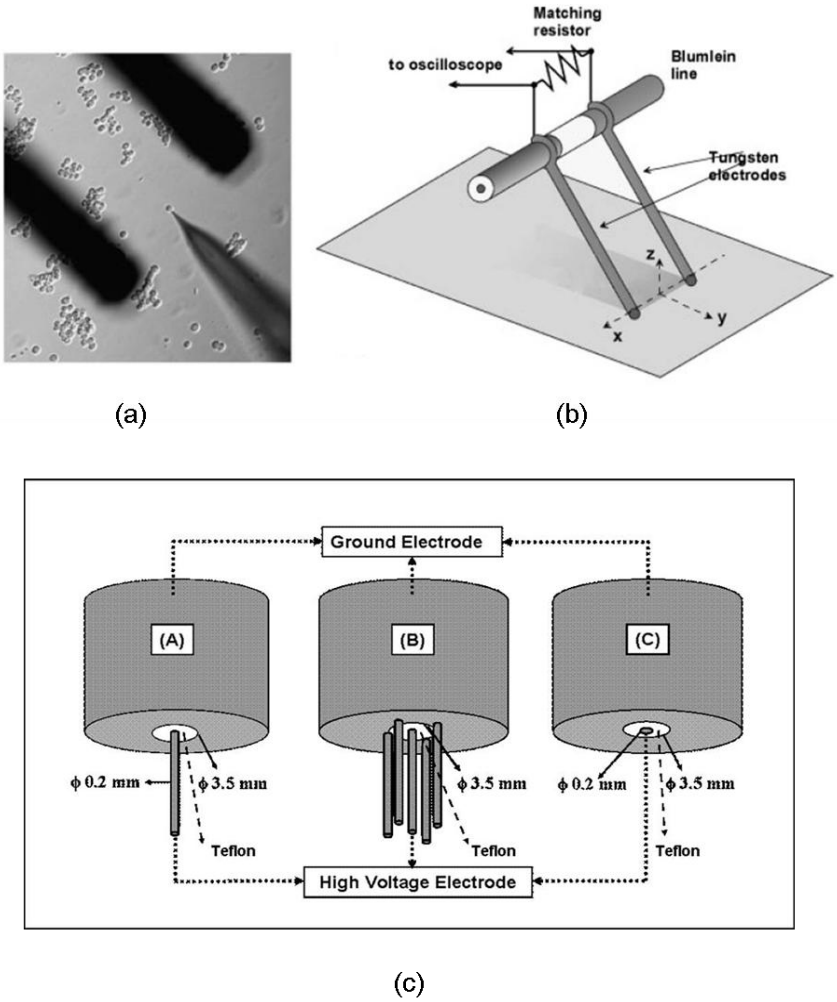

Figure 1-20: *nsPEF exposure of biological cells. (a): positions of pulser electrodes and a glass micropipette in contact with exposed cell, as viewed via the microscope. (b): a sketch of the nsPEF delivery system* **[47]***;* (c) three types of electrode configurations designed for nanoelectropulse treatment and cancer therapy. (A) single-needle, (B) five-needle array, and (C) flat-cut cable **[70]**.

When 10-kV, 15-ns electric pulses are applied to the center electrodes, the electric field is maximum at the center and decays to <10 MV/m at a radius of 0.4 mm for all three electrode configurations. Nevertheless, the flat-cut cable electrode has a higher electric field at the center of the exposure plane than the five-needle and single-needle electrodes. Moreover, the five-needle array is not cylindrically symmetrical. For a given radius the field at a point closer to a ground (outer) electrode will be greater than the field at a point farther away [70].

The planar electrode configuration allows to observe the temporal evolution of the cell (for example the changes in fluorescence) and is a very easy way to expose the cell on a microscopy stage.

We can summarize the common features of the planar electrode topology in six points:

1) Standard transparent glass microscope slide is used as substrate.

2) The channel dimension must accommodate the cell type and the inter-electrode distance appropriate for generating kV/cm electric fields (an example in Figure 1-21(c)).

3) Non-corroding conductive surface, unreactive with biological buffers and growth media and harmless to cells is needed; therefore, gold electrodes are generally preferred [73], but stainless steel electrodes are also used [46], [68].

4) The electrodes are glued with an epoxy layer or paraffin.

5) The chamber walls must be smooth and perpendicular to the chamber floor, obtaining a uniform electric field for all cells.

6) The length is chosen in order to observe a reasonable number of cells. We can also use a multichannel configuration (Figure 1-21(d), 12 mm x 100 μm x 30 μm [73]). Electrical signals may be switched independently to each channel.

This planar geometry permits to design mainly two types of delivery systems: the microelectrodes and the microchamber. The microelectrode system mainly consists in three layers: the microscope slide, the glue, and the electrodes. The electrodes are connected to the cable of the pulse generator directly (Figure 1-21(a)) [68] or through two metallic wires (Figure 1-21(b)) [46]. This configuration allows exposing the cells to 20-ns pulse and electric fields of about 3 MV/cm. The microchamber is specifically designed for microfluidic applications and is based on the superimposition of three layers: the cathode, the dielectric, and the anode (Figure 1-21(c)-(d)) [73].

The electrode gap forms a microchannel where the suspended cells are exposed. The channel geometry allows exposing and observing the cells sequentially. In order to improve the operational efficiency and provide more cells for experiments, several separated microchannels can be used, and the electrical signals may be switched independently to each channel [73]. The delivered pulse duration and electric field intensity are 10 ns and 2.5 MV/m, respectively.

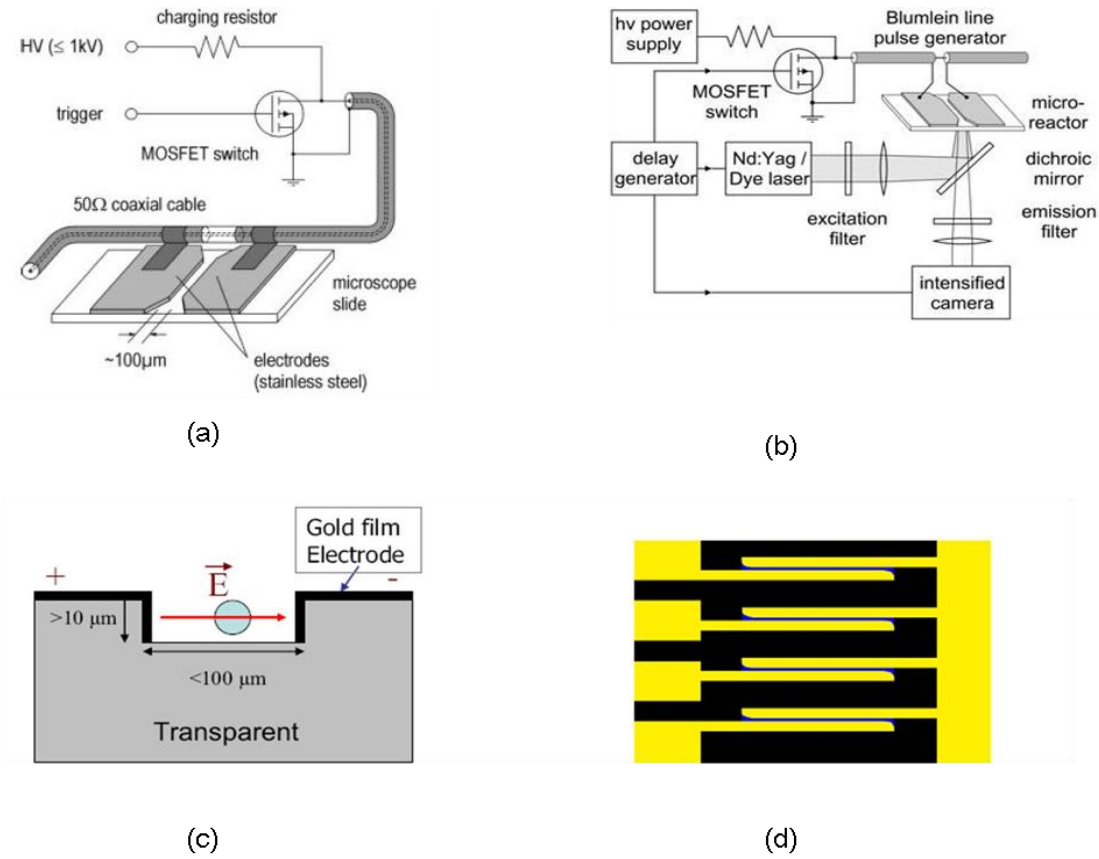

Figure 1-21: *Two examples of exposition systems. a) Conceptual drawing of a microscope-mounted Blumlein pulse generator for real time observation of individual cells* **[68]**. *b) Block diagram of the experimental setup used in* **[46]**: *nanosecond pulse generator, microreactor, and optical system. (c) Ideal microchamber cross section. (d) Design of the microchamber presented in* **[73]**.

THE "BIOCHIP": towards a real-time observation of living cell

In 2011 Dalmay and colleagues [74] have proposed a device to expose the cells to nsPEFs and study the electroporation effects. This exposure system, named "biochip" (Figure 1-22), is composed of a 50 µm thick SU8 microfluidic channel formed by two gold electrodes with a thickness of 25 µm, and a length of 30 mm, containing cells suspended in a biological medium. The distance between the electrodes is of 150 µm and permits to expose the cells to more intense electric fields. The microfluidic biochip was realistically modeled. A FDTD code was used for the numerical simulations, and experimentally characterized in frequency (impedance and reflection coefficient S11) and in time (the incident and reflected signals) [74]. The development of such biochips for the exposure of living cells to nsPEF and the study of electroporation permits the application of more intense (45 kV/cm) and short (3-5 ns) pulsed electric field, the real-time visualization of nsPEF effects, the continuous treatment of cells in flow and ensures a good viability of the cell without contamination.

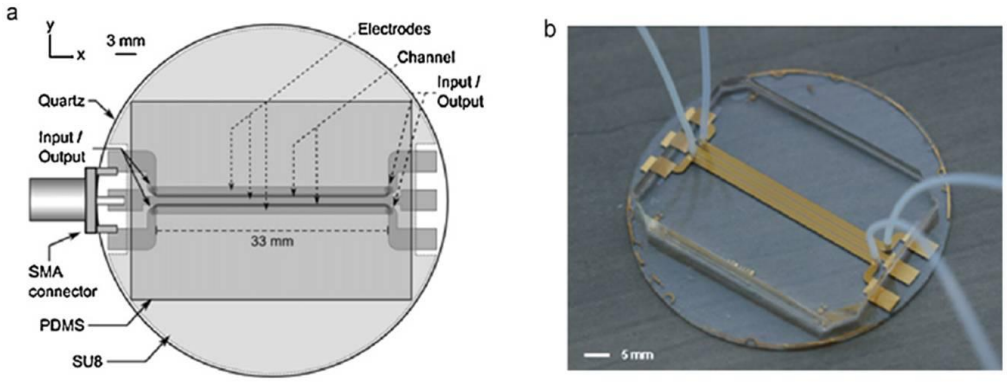

Figure 1-22: *(a) Scheme of the designed microfluidic biochip (top view); and (b) photo of the microfabricated microfluidic biochip* **[74]**.

In summery, an useful exposure system consists of a flexible electric pulse generator, able to provide the desired pulse durantions, intensities and shapes, according to the final applications. The generator is impedance-matched to the PEF application device that must to deliver the maximum energy to the sample, without losses or reflections backwards the generator and avoiding any temporal distortion of delivered pulses.

As the choice of all these parameters is directly linked to the method used to detect the induced bioeffects, in the next and last section of this chapter a comparison between the most common electroporation investigation techniques are reported.

1.5 Electroporation detection techniques

Several techniques have been developed in order to detect the electroporation process through the cell membrane. The most used are the patch-clamp technique, the flow cytometry and the fluorescence microscopy.

The patch-clamp is a technique used to record the current trough the ion channels present in the cell membrane. Neher and Sakmann developed it in the late '70s and received the Nobel Prize in Physiology and Medicine in 1991.

The patch clamp (Figure 1-23) uses as electrode a glass micropipette filled with a physiological solution that simulates the inside cell environment. The micropipette tip has a diameter of about 1 μm, a size enclosing a membrane surface area or "patch" that often contains just one or a few ion channel molecules (see section 1.1).

Generally, the micropipette is pressed against the cell membrane with a soft suction that allows sealing the electrode-membrane contact by producing a giga-ohm resistance (gigaseal).

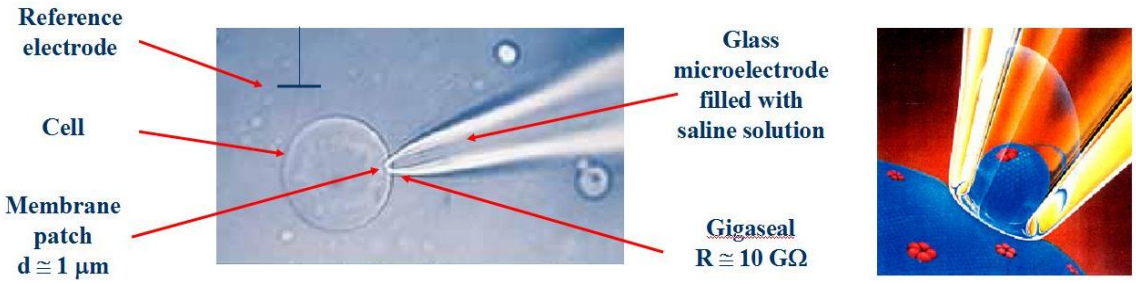

Figure 1-23: *Two images of the patch-clamp technique. On the left, a complete photo of the glass micropipette applied on the membrane patch (whole- cell) and the reference electrode. On the right, a detail of the microelectrode tip that draws a membrane patch for sealing* **[78]**.

The high resistance of this seal makes it possible to electronically isolate the currents measured across the membrane patch with little competing noise, as well as providing some mechanical stability to the recording.

There are different recording configurations for patch clamp [77]:

- *cell-attached* or *on-cell patch* which permits the recording of single channel without membrane rupture.
- *inside-out patch* which consists in putting the micropipette tip in contact with the membrane patch, ripping the patch off the cell leaving it attached to the micropipette, and exposing the intracellular surface of the membrane to the external media.
- *whole-cell patch* that allows recording ionic current of few channels at the same time.
- *outside-out patch* in which, after the whole-cell patch is formed, the electrode can be slowly withdrawn from the cell, allowing a bulb of membrane to bleb out from the cell. Outside-out patching gives the experimenter the opportunity to examine the properties of a single ion channel when it is isolated from the cell, and exposed to different solutions on the extracellular surface of the membrane.

Patch-clamp is perhaps the most powerful technique to analyse ion flows across membranes, and might be most useful for detection of hypothetical nanopores. Nevertheless, for nsPEF this technique presents some limits [47]: for example, existing nsPEF exposure systems [68] have not been designed for and would be inefficient in patch-clamp experiments, and additionally, the high voltages used to produce nsPEF could damage the sensitive electronic circuit of the headstage and patch-clamp amplifier, which are designed to measure millivolts and picoamperes.

Others techniques are fluorescence microscopy, based on the propriety of same molecules to generate photons at longer wavelengths than the excitation one, and multi-photon tomography. A comparison between the images that is possible to obtain is shown in Figure 1-24. The first optical method is the most used until now [83–86], [53], [66], but its major limit is the need for

labelling the cell with a fluorescent stain. There are many fluorescent molecules, called fluorophores or fluorochromes, which can be chemically linked to a different molecule which binds the target of interest within the sample. Fluorophores lose their ability to fluoresce as they are illuminated in a process called photobleaching. Photobleaching occurs as the fluorescent molecules accumulate chemical damage from the electrons excited during fluorescence. This process can severely limit the time over which a sample can be observed by fluorescent microscopy [79].

Fluorescence microscopy with fluorescent reporter proteins has enabled analysis of live cells; however cells are susceptible to phototoxicity, particularly with short wavelength light. Furthermore, fluorescent molecules have a tendency to generate reactive chemical species when under illumination which enhances the phototoxic effect.

Unlike transmitted and reflected light microscopy techniques fluorescence microscopy only allows observation of the specific structures which have been fluorescently labelled. For example observing a tissue sample prepared with a fluorescent DNA stain by fluorescent microscopy only reveals the organisation of the DNA within the cells and reveals nothing else about the cell morphologies. In order to avoid damaging of labelled cells, there are some techniques (for example multi-photon excited fluorescence [81]) that use the fluorescence of the endogenous fluorophores in the tissue such as NAD(P)H, flavins, elastin and collagen in the skin. Detection of autofluorescence makes labelling unnecessary, but provides only limited chemical selectivity, due to the relatively small number of fluorophores visible in the NIR (the wavelength range suitable for biological tissue investigations) and their overlapping absorption ranges, making them unsuitable for multi-color observations at the same time.

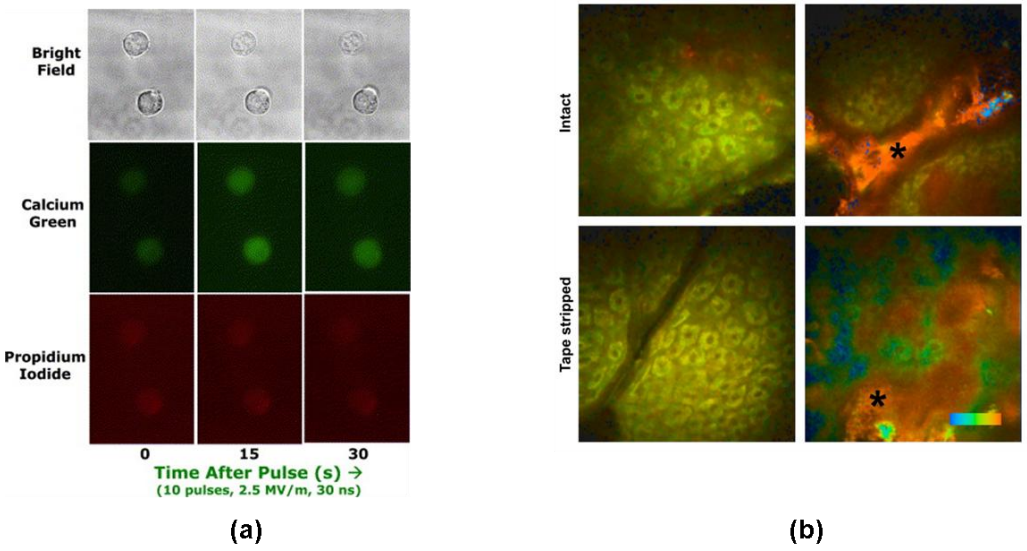

Figure 1-24: *Example of real-time imaging by (a) fluorescence microscopy* **[34]**, *and (b) multiphoton tomography* **[80]**.

In addition, the fluorescence microscopy is limited by the light diffraction, as well as every technique based on classical optical microscopy. Its spatial resolution is generally of the order of hundreds nm and this low resolution limits the use of fluorescence microscopy for studying the interaction at molecular level. Even if current researches have shown that it is possible to improve the spatial resolution from 200 nm to 10 nm thanks to new "super resolution" microscopes [82], [108], it comes at the expense of the acquisition speed. Living cells can potentially move molecules faster than "super-resolution" microscopes can capture images. Moreover, when super resolution moves into 3D, having adequate spatial resolution in a single image becomes difficult.

Recently a new imaging technique, called multiphoton tomography, has been introduced in the clinical practice (Figure 1-24(b)) [80]. This novel tissue imaging system uses an 80-MHz femtosecond near-infrared (NIR) titanium: sapphire tunable laser and is based on multiphoton absorption, a non-linear process occurs only in a tiny sub-femtoliter focal volume when using focusing optics of high numerical aperture (NA) and low (<40 mW) mean powers. Multiphoton tomography provides high-contrast optical images with single-photon sensitivity at submicron spatial resolution (3D), picosecond temporal resolution (4D), and spectral resolution (1–10 nm, 5D) [80]. It is therefore the clinical tissue imaging technology with the best resolution compared to others imaging techniques (ultrasounds, optical coherence tomography, magnetic resonance tomography, and Raman microscopy). The major disadvantage of multiphoton tomographs is the relatively high price (~300 k€) due to the use of femtosecond laser technology.

1.5.1 A promising electroporation detection technique: CARS microscopy

Our choice of using the CARS microscopy as detection technique for the electroporation mechanisms comes from some important features of this optical method that make it advantageous compared to the others techniques mentioned above. Moreover, the efficiency of CARS microscopy for detecting cell electroperturbation has been recently confirmed by some studies [83], [84].The key-points in favour of CARS microscopy are summarised in the following:

- CARS microscopy is a **label-free** technique, suitable for non-inavise imaging of living cell.
- As a coherent process, the CARS signals from different molecules have a well-defined phase relationship and they add up like the emission from an antenna array. **The coherent addition** also results in a quadratic signal increase with respect to the density of molecular oscillators.
- Since the CARS process has a temporal dynamic of the order of femtoseconds compared to the classical fluorescence (order of nanosecond), with a CARS performing microscope

we can foresee to obtain a **higher temporal resolution** that improves the real-time detection of the molecular dynamics.

- Thanks to the nonlinear dependence of the CARS signals on the excitation field intensity, CARS microscopy has an inherent **sub- micron 3D spatial resolution.**
- As CARS signal appears at a wavelength shorter than the excitation wavelengths, it is **not affected by the fluorescence background** in the detection window.
- During CARS process the molecule doesn't reach the excited state, as a consequence CARS is **not subject to photobleaching**.
- CARS technique is mainly preferred to lipid imaging because of its **high sensitivity to C-H bondings.**
- The possibility to use near infra-red (wavelengths less absorbed by water) excitation limits the absorption of the radiations from the biological sample, and, thus, **avoids the sample heating.**
- Several molecular dynamic models explain the pore formation as a potential rearrangement of water molecules at the interface cell membrane/suspension that should create a idrophilic channel trough the membrane [85–87]. Nowadays, no imaging technique has been able to give more information about this molecular mechanism. Instead, CARS microscopy can be used to **characterize the orientation of a symmetric molecule such as H_2O (water) or a functional group such as CH_2 (lipid chain)** in order to obtain information regarding the nature of the interfacial molecule interactions [88].

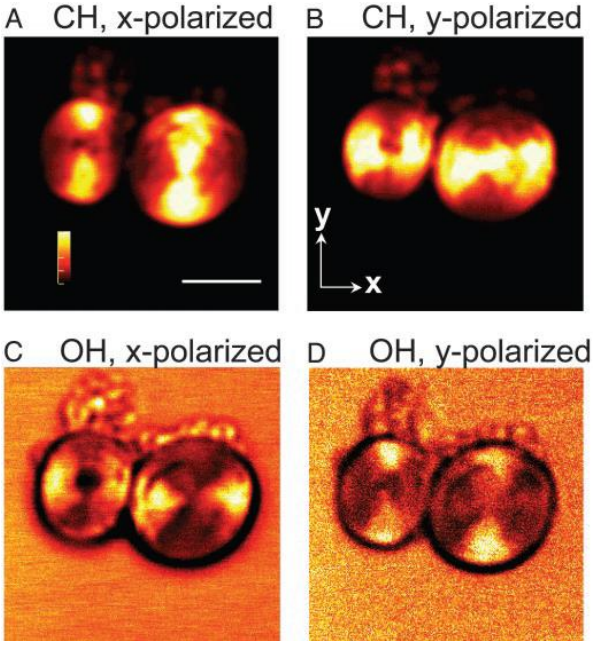

Figure 1-25: *Example of real-time imaging by CARS microspectroscopy* **[88].**

Chapter 2- Coherent anti-Stokes Raman (CARS) spectroscopy: a state-of-the-art

Among various nonlinear optical effects and nonlinear optical spectroscopic techniques, nonlinear vibrational spectroscopy is one of the most powerful methods, because it enables us to obtain molecular-level information from a sample using its vibrational spectra. In other words, it is a method of detection and analysis of the structure and the chemical composition of the molecules, through the determination of vibration frequencies of a molecule excited by light.

In particular, nonlinear Raman spectroscopy is a very efficient technique which is applicable to life, medical and material sciences, because the signal intensity is not affected by water and is noninvasive.

The Raman effect is an optical interaction phenomenon that has attracted attention from a basic research point of view since its discovery in 1927 [89], when two indians Raman and Krishnan observed an inelastical light scattering phenomenon, focalizing the sun light on different molecular matters through a telescope. In essence, this light-matter interaction phenomenon results in a frequency shift of the diffused photons compared to the incident ones. This shift, called Raman shift, is specific of the molecule exposed to the light excitation. A molecule has a structure composed of many interatomic vibrations and rotations. These roto-vibrational modes have a specific energy that they exchange with their environment and the Raman shift is the spectral signature of this energetic exchange with the light.

Advances in optical imaging techniques have revolutionized our ability to study the microscopic world. Simple microscopy techniques, such as bright field and differential interference contrast microscopy, have played a large role in cellular and molecular biology experiments but don't provide chemical specificity. Imaging modalities capable of identifying specific molecules have significantly improved our understanding of biological processes on the microscopic scale. Many of these techniques, however, require the use of exogenous labels that often perturb the system of interest, as we have mentioned at the end of the previous chapter. Among them there is the fluorescence imaging that offers molecular specificity but the number of endogenous fluorophores is limited.

Vibrational microscopy techniques, like infrared (IR) microscopy and Raman microscopy, offer intrinsic chemical selectivity, but they are limited by a number of difficulties including low

sensitivity due to the non-background-free detection, low spatial resolution and water absorption for IR microscopy due to its long wavelength. The Raman microscopy has its major limitation in the long data acquisition times due to the extremely weak spontaneous Raman signal and, consequently, requires high laser power and long integration times of 100 ms to 1 s per pixel [90]. These factors severely limit the application of Raman microscopy to the study of living systems. In this context a new technique has been proposed [91], named coherent anti-Stokes Raman scattering (CARS) microscopy, that largely improves the microscopic techniques based on the Raman effect.

In the following of the chapter is reported a description of Raman physical phenomena, a synthetic review of CARS optical techniques, and the contribution of optical fiber advent to the broadband sources for CARS microspectroscopy.

2.1 Radiation-matter interaction physical effects

When the radiation interacts with the matter, different cases are possible [92], [93]. The radiation energy can match a possible transition to a higher energetic level; therefore, the absorption occurs and the energy of the initial wave is lost by increasing the matter temperature. In another case, the radiation interacts with the matter but it does not cause any transitions. In this case the diffusion occurs. There are two possible way of diffusion (Figure 2-1): an elastic (or Rayleigh) diffusion, in which a smaller part of the radiation spreads elastically in every directions without lost of energy, at the same radiation frequency; and an inelastic diffusion (Raman scattering), in which the smallest part of the radiation spreads inelastically, namely, it can exchange energy with the system (Raman Stokes and Raman anti-Stokes). The intensity of spreading radiation (smaller of the incident one) depends on the contribution of elastic and inelastic scattering, and these contributions depend on the chemical structure of the molecules responsible of the radiation diffusion.

A typical spectrum of the diffused light is often given by the intensity versus frequency shift with respect to that of the stimulating radiation. Stokes and anti-Stokes lines are symmetrically placed with respect to Rayleigh line and the gap of energy represents the energy acquired from or given to the molecule in the variation of the initial vibration level. Therefore, we refer to Stokes diffusion in the case of a red-frequency-shift, and to anti-Stokes diffusion if we observe a blue-frequency-shift.

Often is suitable to use anti-Stokes lines, even if they are less intense that Stokes lines, because the interference in the detection of Stokes-shift is stronger in the case of fluorescent substances. The ensemble of the emission frequencies of the molecules affected by incident light composes the Raman spectrum of the compound.

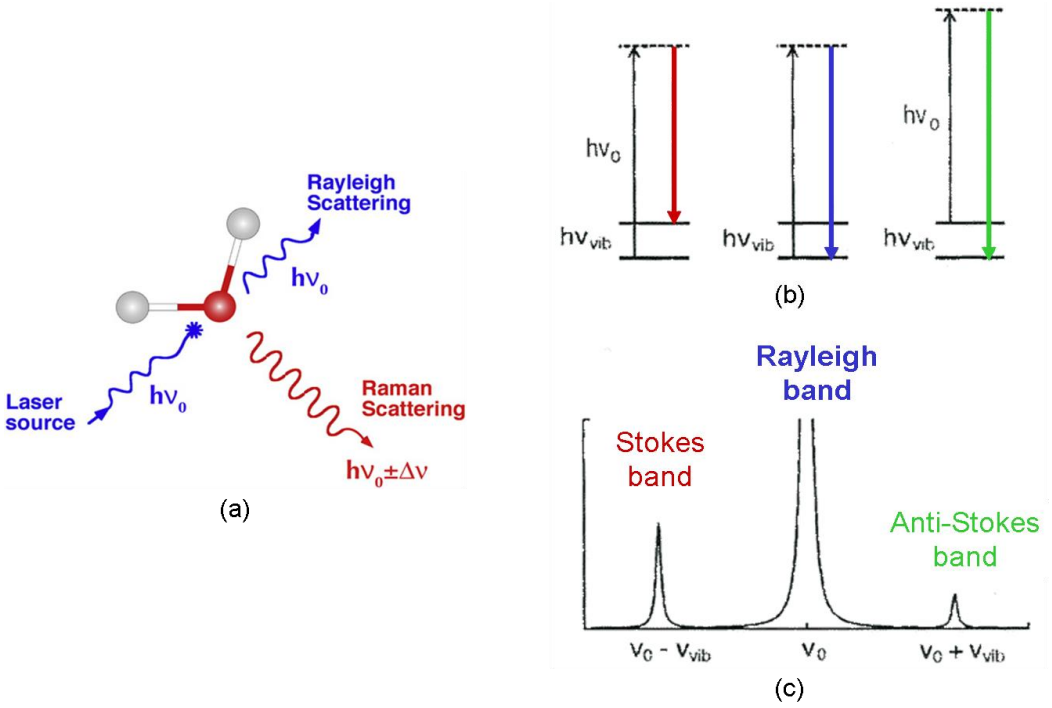

Figure 2-1: *(a) Simple representation of the interaction between the laser radiation and a dipole. (b) Energy diagram of the Rayleigh and Raman interactions, and (c) spectral position of the Rayleigh, Stokes, and anti-Stokes bands.*

The Raman effect is a powerful tool for spectroscopy because it permits to determine the chemical composition of the molecules by illuminating the sample with a monochromatic source and recording the diffusion spectrum that is related to the atomic bonds representing the structure of the matter under investigation.

However, this spontaneous Raman effect produces a weak signal (as said before, photoconversion efficiencies are lower than 1 in 10^6-10^8 events) and the Raman spectroscopy requires high laser powers and long integration times [94], [95]. These factors have limited the application of Raman spectroscopy to the study of living systems until laser advent in 1960. This event opened the way to new techniques of nonlinear optics. In 1961, Frenkel and colleagues [96] for the first time demonstrated the Second Harmonic Generation (SHG) in a quartz crystal. In the same year Kaiser and Garret [97] observed the fluorescence in two-photon excitation. In 1962 Eckhardt *et al*. [98] showed Stimulated Raman Scattering (SRS) from organic liquids, and in 1965 Maker and Terhune [91] studied, both theoretically and experimentally, the third order nonlinear effects. Among them Four-Wave Mixing (FWM) is a parametric phenomenon that later will be combine with the Raman one to give birth to the CARS. Since the first systematic study of CARS carried out by Maker and Terhune at Ford Motor Co., CARS spectroscopy has become the most extensively used nonlinear Raman technique.

2.2 Coherent anti-Stokes Raman scattering (CARS): a third order nonlinear process

CARS is a stimulated Raman process that permits to obtain stronger vibration signals from the Raman interaction with the medium. In the CARS process (Figure 2-2), two laser beams are used for excitation; the first one named *pump beam* at the oscillation frequency ω_{pump} has got the same role than the classical Raman beam, and excites the molecules from a ground state to a very short life time virtual state (around 10^{-14} seconds). From this virtual vibration state, the molecules reach a real vibration state thanks to a coherent relaxation initiated by the second laser beam named *Stokes beam* at the oscillation frequency ω_s. Once the real vibration state is reached, the initial pump excites the electrons at this state with the beam named now *probe beam* at ω_{probe}. This third beam initiates the excitation of the molecule from the vibration state to another virtual state and this virtual state finally relaxes on the ground level by the emission of an anti-Stokes photon. This process is named four-wave mixing because three beams, pump, Stokes, and probe beam are temporally and spatially overlapped on a sample and they produce a fourth beam, *anti-Stokes beam*, at the oscillation frequency $\omega_{as} = \omega_{pump} + \omega_{probe} - \omega_s$. Generally, the pump and the probe are chosen to be provided by the same laser beam and, so, they have the same oscillation frequency ω_p.

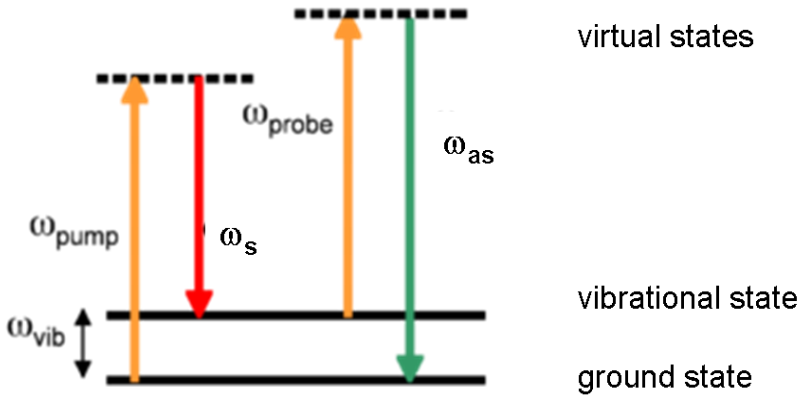

Figure 2-2: *Energy diagram of CARS process.*

In other words, CARS is a third order non-linear optical process in which a pump field $E_p(\omega_p)$ and a Stokes field $E_s(\omega_s)$ interact with a sample to generate a signal field E_{as} at the anti-Stokes frequency of $\omega_{as} = 2\omega_p - \omega_s$.

When $\omega_p - \omega_s$ is tuned to be resonant with a molecular vibration, the CARS signal can be significantly enhanced, producing a vibration contrast and so resonance Raman studies of selected components of a sample or part of a molecule can be performed. This interaction phenomenon more efficient in comparison with a classical Raman process is forced by the difference of frequency between the pump and the Stokes laser waves. Beyond the efficiency, another interest is the coherence of the CARS beam that is emitted in a given direction with a low divergence. That spatial beam distribution is governed by the phase matching process given by the following equation: $k(\omega_p) + k(\omega_p) + k(\omega_S) = k(\omega_{AS})$.

When a system is immersed in an electric field, three distortions can be observed on a molecule: bending, stretching and rotation of its atomic bonds (Figure 2-3).

The molecule polarizes, changing the distribution of its electron cloud. An induced moment of dipole p is generated:

$$p = \varepsilon_0 \chi E \quad \textbf{(5)}$$

where $\varepsilon_0 \chi$ represent the property of the system to polarize.

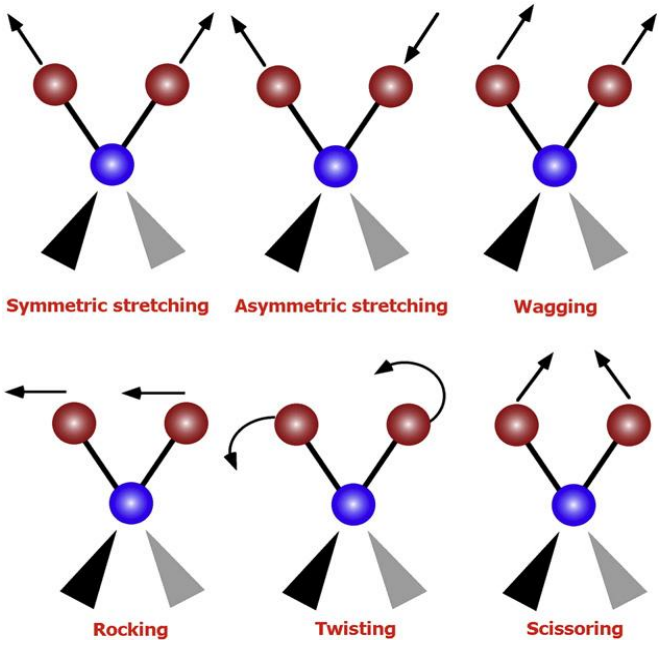

Figure 2-3: *Simple layouts of the vibrational modes associated to a molecular dipole moment change detectable in an IR absorption spectrum. In addition to the two stretching modes, the four different bending vibrations are shown.*

CARS is a non-linear process that induces a polarization vector expressed by:

$$p = \chi^{(1)} E + \chi^{(2)} E + \chi^{(3)} E \quad \textbf{(6)}$$

where:

– $\chi^{(1)}$ represents linear polarization of the matter after field application;

– $\chi^{(2)}$ represents the property of the matter to change in intensity of the emitted radiation with the wavelength of light. This term takes into account different effects as two-photon fluorescence excitation, second harmonic generation;

– $\chi^{(3)}$ represents the response of the system to four-wave process as the stimulated Raman scattering (CARS) which includes four photons: 2-"pump" photons, 1-Stokes photon and 1-anti-Stokes photon [92].

CARS is a coherent emission that is proportional to the square of the pump beam intensity, directly proportional to the Stokes beam intensity and the square of the sum of response of all the molecules (proportional to the square of the concentration molecules contributing to $\chi^{(3)}$).

Then we obtain the following expression:

$$P_{as} = \varepsilon_0 \chi^{(3)} E_p^2 E_s \quad \textbf{(7)}$$

The electric fields must be important to induce a strong polarization because the third order susceptibility is generally weak in silica fibers.

In details, the third-order susceptibility is given by [99]:

$$\chi^{(3)} = \frac{A_R}{\Omega - (\omega_p - \omega_S) - i\Gamma_R} + \chi_{nr}^{(3)} + \frac{A_t}{\omega_t - 2\omega_p - i\Gamma_t} \quad \textbf{(8)}$$

Ω in equation (8) is the vibrational frequency. Γ_R and Γ_t are the half-width at half-maximum of the Raman line and that of two-photon electronic transition, respectively. A_R and A_t are constants representing the Raman scattering and the two-photon absorption cross sections. The first term is a vibrationally resonant contribution (Figure 2-4(A)). The second term is a nonresonant contribution that is independent of Raman shift (Figure2-4(B)). The third term is an enhanced nonresonant contribution due to two-photon electronic resonance (Figure2-4(C)).

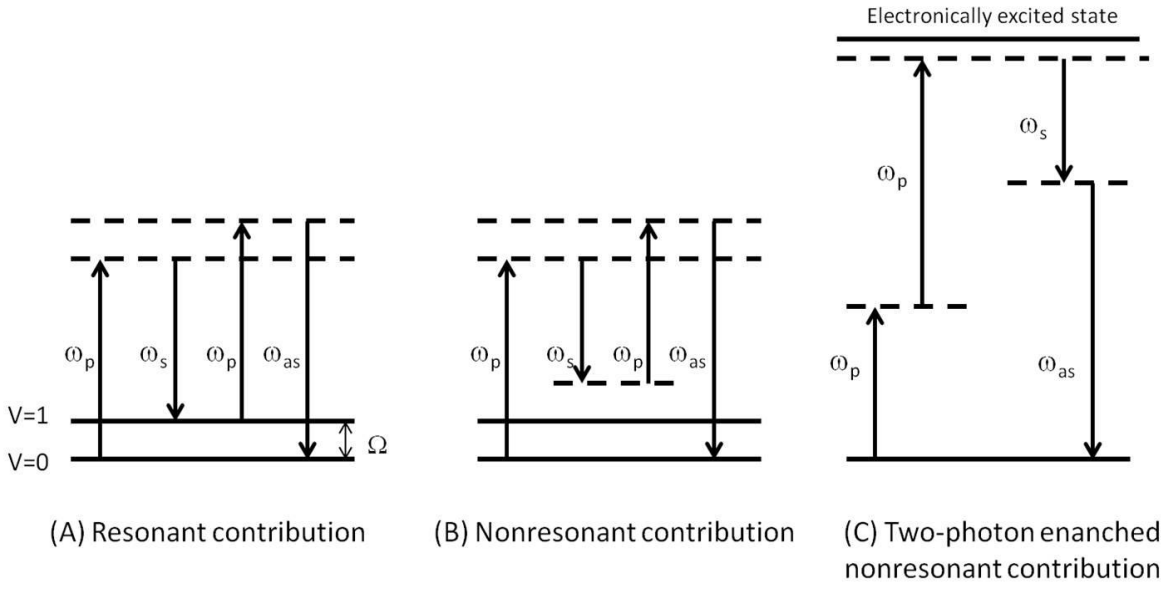

Figure 2-4: *Energy diagram of CARS. (A) Resonant CARS characterized by the first term of equation (4). (B) Nonresonant CARS from an electronic contribution (second term in (8)). (C) Electronic contribution enhanced by a two-photon resonance of the pump beam associated with an excited electronic state.*

Thus CARS process needs high peak power to induce material polarization and then emits CARS signal under phase-matching condition, expressed as:

$$\left|k_{AS} - (2k_p - k_S)\right| L < \pi \quad \textbf{(9)}$$

where k_p, k_s, and k_{as} are wave vectors of pump, Stokes and CARS fields, respectively, and L is the light-sample interaction length. Constructive interference occurs when the field-sample interaction length L is less than the coherence length L_c (namely, the length beyond which the laser beam loses its coherence), at which the CARS signal reaches the first maximum.

In the past few years, the range of excitation wavelengths has been extended to the near-infrared (NIR) region, in which background fluorescence is reduced and photo-induced degradation from the sample is diminished. High-intensity NIR diode lasers are easily available, making this region attractive for compact, low cost Raman instrumentation. Further, the development of low noise, high quantum efficiency multichannel detectors (charge coupled device (CCD) arrays), combined with high throughput single-stage spectrographs used in combination with holographic laser rejection filters, has led to high-sensitivity Raman spectrometers [89]. Then, in 1982 the nonlinear Raman spectroscopy was applied to microscopy for the first time, leading to CARS microspectroscopy.

2.3 CARS microscopy

The first attempt toward using CARS as a microscopy technique was made by Duncan *et al.* in the 1980s [100–102]. Using two picosecond visible dye lasers, non-collinear beam geometry (where pump and Stokes propagates with different directions, Figure 2-5(B)), and a charge-coupled device (CCD) detector to record the signal at the phase matching direction, the authors acquired CARS images of D_2O distribution in onion skin cells. However, the non-collinear beam geometry in their work limited the image quality and the excitation with visible wavelength resulted in a large nonresonant background.

Zumbusch and co-workers [103] revisited CARS microscopy in 1999 by using near-infrared laser pulses that avoid two-photon electronic enhancement of the nonresonant background, and a collinear beam geometry, significantly improving the imaging quality.

Nevertheless, the femtosecond pulses used in the work of A. Zumbusch *et al.* are not optimal for vibrational spectroscopy because their spectral widths are broader than Raman bandwidths. In that case a low spectral resolution is obtained reducing the efficiency of CARS method.

In 2001, Volkmer *et al.*, conceived a new CARS microscope with two synchronized picosecond lasers, which not only provided better spectral resolution but also improved the signal background ratio [104]. One year later, Cheng *et al*. developed a laser-scanning CARS microscope with two near-IR picosecond pulse trains and achieved a rapid acquisition rate, allowing visualization of fast cellular processes [105].

The application of the CARS process to the microscopy gives a new method of chemical imaging. In CARS microscopy, the temporally and spatially overlapped pump and Stokes laser pulses are tightly focused into a sample to generate a signal in a small excitation volume (< 1 μm^3). A CARS image is acquired by scanning the sample by means of laser beams.

CARS microscopy offers several unique advantages.

1. It provides a good contrast based on the intrinsic molecular vibrations of a specimen, without need for labelling. This advantage is important for imaging small molecules as lipids or drugs for which the labelling may significantly affect the molecular properties.

2. It is order of magnitude more sensitive than spontaneous Raman microscopy, permitting video-rate vibrational imaging at moderate excitation powers. In fact, the coherent addiction of optical fields results in a quadratic signal increase with respect to the molecular oscillator number, versus the linear increase of the spontaneous Raman signal.

3. The high directionality of CARS output makes easy the signal collection.

4. The nonlinear nature of the CARS process automatically improves its capability of three-dimensional sectioning, which is essential for imaging thick tissues or cellular structures. When using near-infrared excitation wavelengths, CARS microscopy can penetrate to depths of nearly 0.4 mm, allowing 3D imaging.

5. The anti-Stokes signal is blue-shifted from the pump and Stokes frequencies, and is therefore easily detected in the presence of one-photon fluorescence.

6. As the CARS process occurs on the ground electronic state, sample photodamage is minimized, especially when picosecond and femtosecond pulses are used to reduce multiphoton effects and incident energy respectively.

7. Thanks to the freedom of polarization configurations in the coherent anti-Stokes Raman it is also possible to identify chiral molecules during various biochemical reactions [106].

The major disadvantage of CARS microscopy is the existence of the nonresonant background that is coherently mixed with the vibrationally resonant signal and limits the sensitivity of CARS in detecting weak Raman bands. Additionally, given the quadratic dependence of the resonant CARS signal with respect to molecular concentration, the detection of low-concentration molecules is difficult. In the past few years many efforts have been spent on suppressing the nonresonant background and improving the detection sensitivity limit. We will go back on the strategies used to suppress the nonresonant background later.

2.3.1 New features of CARS under Tight Focusing condition

As a nonlinear coherent process, CARS signal generation needs to fulfil the phase matching condition (9) that is the simple translation of the motion quantity conservation of the pump, Stokes and anti-Stokes photons involved in the CARS process.

In the CARS technique with a collinear geometry, the dispersion of the refractive index $(n_j,\ j = p, s,\ \text{and}\ as)$ introduces a wave vector mismatch which can be written as: $(n_{as}\omega_{as} - 2n_p\omega_p + n_s\omega_s)/c$ (where c is the light velocity in vacuum). In order to obtain CARS signal, that quantity must be minimized. However, the phase matching condition (9) is generally relaxed and fulfilled in the collinear beam geometry because of the small interaction distance. However, the collinear beam geometry requires filtering the output signal from the input beams because they propagate in the same direction. An alternative is provided by non-collinear beam

geometries such as BOXCARS geometry [107], used to spatially separate the CARS signal from other incident wave-mixing components without need for dirchoic mirrors.

For the CARS microscopy set-up presented in this work, we have chosen the collinear geometry; therefore, we did not care for fulfilling the phase-matching conditions (Figure 2-5).

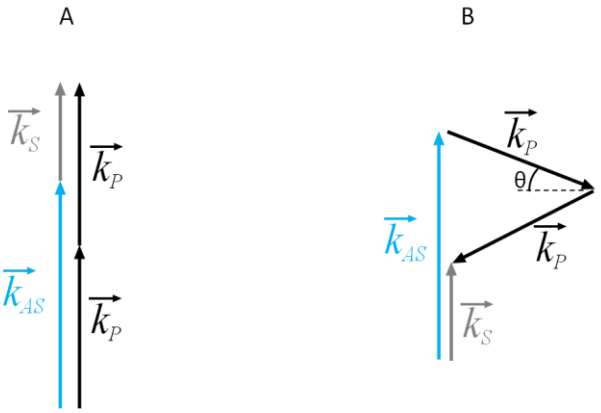

Figure 2-5: *(A) Collinear, and (B) non-collinear beam geometries satisfying the phase-matching conditions in a non dispersive medium.*

2.3.2 Detection configuration of CARS signal

Unlike fluorescence emission and spontaneous Raman scattering, the radiation pattern in CARS microscopy is highly dependent on the size and shape of the scattering objects, the nonlinear susceptibilities of the object, and the local environment. Indeed, the output CARS signal is the result of summation of elementary CARS radiations coming from an ensemble of coherently induced Hertzian dipoles inside the scatterer. All the elementary CARS radiations propagate in all the space with a coherent sum of the contributions only in the direction satisfying the phase matching condition. There are different configurations for collecting CARS signals. They are briefly discussed here. In the case of forward CARS (F-CARS), the excitation beam is focused on the sample through a high–NA objective. A condenser lens is used to collect the forward signal that is a coherent addition of the CARS radiation from the scatterers. That coherent sum gives birth to a directive CARS beam easily collected by standard optics. The CARS signal is then separated from the excitation beams by using band-pass filters. In this configuration both resonant and nonresonant signals are collected, producing images with noise. Polarization CARS (P-CARS) is generally used to suppress the nonresonant background in CARS microscopy applications, by taking advantage of different polarizations between the electronic and the vibrational resonance.

In the case of backward-propagating radiation (E(epi)-CARS), the CARS signal is collected with the same objective used for focusing the laser beams. There are three mechanisms for the

generation of the backward radiation [108]. In the first mechanism, E-CARS signal is generated from objects whose the size is small enough $(\lambda_p/3)$ for incomplete destructive interference to occur in the backward direction. In the second mechanism the epi-propagating signal is due to the discontinuities in $\chi^{(3)}$, because they are essentially infinitely small objects that break the symmetry of the focal volume. The third mechanism occurs when the sample contains many local changes of the refractive index that redirect forward-propagating photons in the backward direction (as in turbid samples, for example the skin).

In general, for objects that are much smaller than the excitation wavelengths, the phase matching condition is relaxed and the CARS radiation goes forward and backward symmetrically, as that from a single Hertzian dipole.

Because the CARS signal from the surrounding solvent goes forward, F-CARS is limited by the large nonresonant background from the solvent, and so E-CARS provided a sensitive means to detect small objects embedded in a bulk medium [109].

F-CARS is also suitable for imaging objects of a size comparable to or larger than the excitation wavelength. In fact, if the size of scatterer is larger epi-directed fields from dipoles across the object run out of phase with each other leading to destructive interference of E-CARS signal [110].

2.3.3 Suppression of nonresonant background

In order to suppress the nonresonant background from the solvent surrounding the sample and the others scatterers and consequently improve the CARS signal quality, several techniques have been proposed between the 1970s and 1980s [111–116].

The mainly schemes are summarized as follows.

Detection with large wave vector mismatch

This method introduces a large wave vector mismatch, which acts as a size filter that rejects the signal from the bulk solvent and allows high-sensitivity imaging of small objects. E-CARS microscopy has been demonstrated as an effective way to reject solvent background, as said above. Another way to suppress the nonresonant signal from the solvent is the counter-propagating CARS (C-CARS), in which pump and Stokes beams propagate collinearly but in the opposite directions. Both E-CARS and C-CARS are suitable for imaging small dense particles in a nonlinear medium [112–114].

Polarization-sensitive detection

Polarization-detected CARS (P-CARS) utilizes the different polarization properties of the resonant and the nonresonant components of $\chi^{(3)}$. For example, in the CARS-ROA scheme, the

achiral compound background can be suppressed by polarization-selective CARS measurements because the polarization of chirality-induced CARS signals is orthogonal to that of the achiral background [106], [111].

Detection by Time-Resolved CARS

With femtosecond pulse excitation, the vibrationally resonant signal can be temporally separated from the nonresonant electronic contribution by the use of pulse-sequenced detection. Indeed, Time-Resolved detection is based on different free-induction decay rates of the resonant and nonresonant contributions. With a flat profile in the spectral domain, the nonresonant background contributes to an instantaneous spike in the time domain due to electronic dephasing. The resonant part involves a vibrational transition and has a longer dephasing time (on order of 1 picosecond) that is related to the spectral width of the corresponding Raman line. Thus, the nonresonant background can be eliminated by introducing a suitable time delay between the femtosecond pump/Stokes pulses and the probe pulse [116].

Interferometric CARS

Interferometric CARS method separates the real and imaginary parts of $\chi^{(3)}$ by using a local oscillator to interfere with the CARS signal from a sample. Moreover, this approach amplifies the signal level because the detected signal is the interference term between the resonant signal and the local oscillator [117].

2.4 Towards a molecular selectivity: multiplex-CARS microspectroscopy

While CARS microscopy allows high-sensitivity vibrational imaging of particular molecules, CARS microspectroscopy provides molecular structure information about microscopic samples. Since the live matter is composed by partially ordered atoms which constitute the molecules, every molecular bond is characterized by a given resonance frequency, so it is desirable to have a spectroscopic technique that allows to obtain the vibration information for a wide frequency band in only one measurement. Whereas a measurement with simple CARS technique gives information about only one vibration frequency, multiplex-CARS (M-CARS) technique allows to excite simultaneously a larger number of chemical bonds which represent the molecular structure of the matter. M-CARS spectroscopy was first demonstrated by Akhmanov *et al.* in 1974 [118] and permits fast data acquisition of plenty of vibrational transition frequencies.

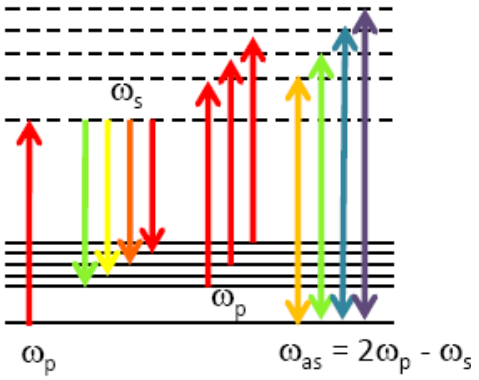

Figure 2-6: *Energy diagram of M-CARS process.*

Recently, M-CARS microspectroscopy has been developed for fast spectral characterization of microscopic samples [119], [120], [121], [122]. The physical principle of M-CARS is similar to the classical CARS technique, but instead of focusing a monochromatic Stokes beam on the sample, a polychromatic beam, called supercontinuum (SC), is used (Figure 2-6). Thus, all the electrons on the excited virtual states are coherently relaxed through Stokes beam on different vibration energy states, and produce the excitation of the whole molecule bonds at the same time. Then the same process than the classical CARS occurs simultaneously for each chemical bond, and a broadband coherent anti-Stokes relaxation beam is obtained.

It is important to remark that all the components of all beams (the monochromatic pump and the polychromatic Stokes beam), must be superposed in time and in space in order to obtain the signature of the most of the chemical bonds.

2.4.1 Laser sources for M-CARS microspectroscopy

Developments in laser sources have been essential for the advances in CARS microscopy [123]. CARS microscopy needs synchronized pulsed sources for pump and Stokes beams. One solution consists in using a femtosecond laser, coupled to an optical parametric amplifier (OPA) or an optical parametric oscillator (OPO). This approach was first chosen in 1999 by Zumbusch *et al.* [103], which used two synchronized femtosecond pulse trains at high repetition rate, generated from a Ti:sapphire amplifier operating at 855 nm and homebuilt OPO and OPA operating at 1.1-1.2 μm. This system permitted to cover a Raman shift range between 2600 and 3300 cm^{-1} (a typical region for $C-H$ and $N-H$ vibrations, Figure 2-7).

Since it is difficult to distinguish the molecular species in the high-frequency region of CH , OH , and NH stretching vibrations, the extension of the observable Raman-shift region to the fingerprint region is very important (Figure 2-7). In 2000 Haschimoto *et al.* [124] proposed, for

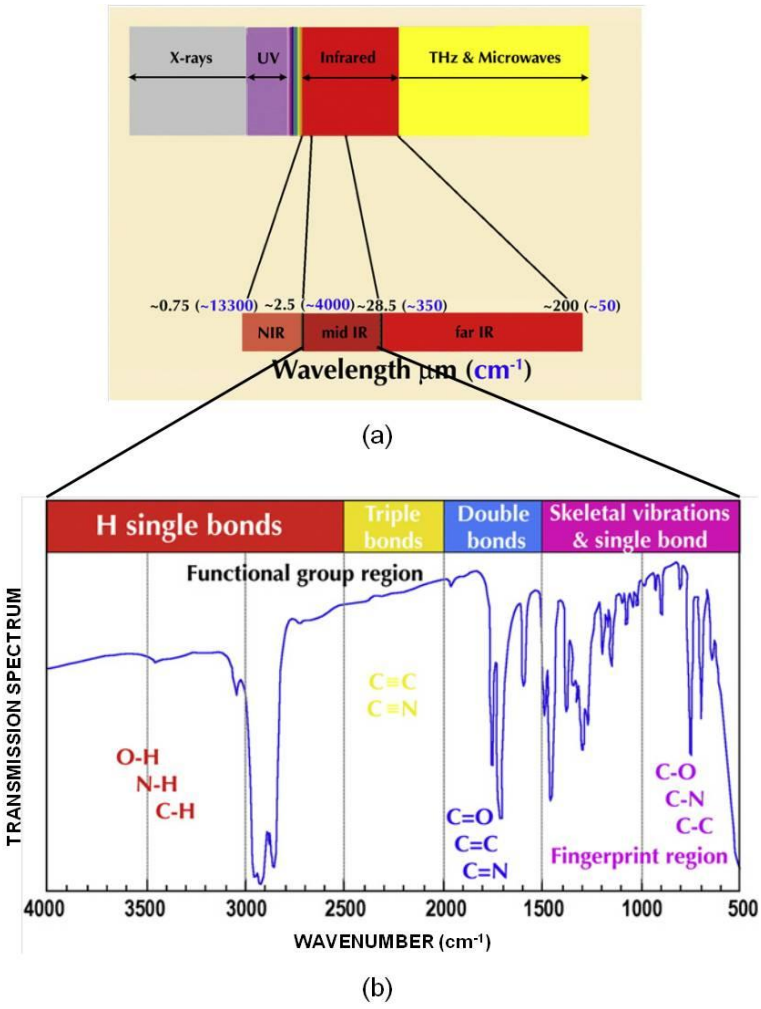

Figure 2-7: (*a) The wide IR range covering more then three orders of magnitude in the unit of wavelengths (or wavenumbers). (b) A typical mid-IR transmission spectrum showing in a schematic way typical absorptions lines associated to vibrational modes of molecules, organic components and others contributions of biological and non-biological nature.*

the first time, a tunable laser system running in the picosecond regime. It consisted in a tunable picosecond OPA (Stokes beam) coupled to a picosecond regenerative amplifier (pump beam). In this case, the observable Raman-shift region was 900-1750 cm^{-1}.

In order to expand the biologically interesting region of the vibrational spectrum (from 500 to 3500 cm^{-1}) two passively mode-locked picosecond Ti:sapphire lasers were implemented [125].

An important challenge in using two independently running optical oscillators is the control of the time coincidence of the individual laser pulses. In fact, the timing jitter among the pulses leads to signal fluctuations that, in turn, degrade the image. A solution, proposed by Potma and colleagues [125] consisted in the use of two oscillators (the one being the master, the other the slave) temporally synchronized by means of a fast piezo-transducer assuring active feedback control of the repetition rate.

Another solution was the light source presented by Evans *et al.* [126], that provides excellent power stability and intrinsic synchronization of the pump and Stokes pulse trains, which are essential for high-sensitivity video-rate imaging. This system was composed of a 1.064-nm-mode-locked Nd: YVO4 laser, delivering picosecond pulse train. A part of the output was used as the Stokes beam, and the remaining part was used for synchronously pumping an OPO to generate the pump beam.

With the advent of the photonic crystal fibers new laser sources for M-CARS microspectroscopy were introduced and made easier the generation of a broadband beam without the need for more-complex lasers, as mentioned above. Because of their high nonlinearities and high tunable dispersion properties (that we will discuss in the next sections) these fibers provide unique media for nonlinear interactions at low powers. Paulsen *et al*. in 2003 [127] demonstrated a CARS microscope based on a femtosecond Ti:sapphire oscillator. The setup was composed of a 40-mm-long PCF in order to generate a frequency-shifted beam used as the pump beam and of a fundamental 795-nm-beam used as the Stokes beam.

In another study, instead, a broadband Stokes beam generated from femtosecond oscillators and a tapered fiber [128], or a photonic crystal fiber [104], was used to perform for the first time a CARS microscope that could acquire simultaneously spectral information over at least 2500 cm^{-1} (SC spans in the range 500-1100 nm).

In 2006 Ganikhanov *et al.* [129], presented a broadly tunable OPO in the picosecond regime, based on a periodically poled crystal (PPKTP), synchronously pumped by the second harmonic-532-nm-output of a mode-locked laser, obtaining a frequency-shift region from 100 to 3700 cm^{-1}.

Another very promising alternative to the current state-of-the-art is represented by nanosecond or subnanosecond lasers, proposed for the first time by Okuno *et al.* [130–132].

From 2007 they have developed an ultrabroadband-M-CARS microspectroscopy using a sub-nanosecond microchip laser source. A few-meter-long PCF specifically designed for sub-nanosecond SC generation has been used to obtain ultrabroadband Stokes radiation that has permitted vibrational excitation in the range 800-3000 cm^{-1} [130–132].These studies are the result of the collaboration between Xlim laboratory and the University of Tokyo.

Despite the benefits of the nanosecond and sub-nanosecond sources (including a higher spectral resolution and easier pump/Stokes pulse synchronization), the spectro-temporal structure of the nanosecond Stokes wave remains more complex and less theoretically understood than that obtained in femtosecond domain [104]. In fact, the mechanisms leading to the SC generation in a PCF depend both on the parameters of the input pulses (peak power, duration, shape, spectrum, stability, wavelength) and on parameters of the PCF (dispersion profile, effective modal area, birefringence, length, losses). All these parameters are mixed with nonlinear phenomena as:

self-phase modulation (SPM), cross-phase modulation (XPM), four-wave mixing (FWM), stimulated Raman scattering (SRS), and solitonic propagations, in order to produce a broadband stokes beam. Unfortunately the dynamics of the nonlinear effects gives birth to large temporal instabilities with the build-up of solitons and rogue solitons propagating in presence of large Raman perturbation which drastically distorts the input signal. All these phenomena are not completely understood and must be properly studied in order to better design CARS system. For all these reasons, we have been performed a characterization of such phenomena in time and spectral domains, that is described in the Chapter 4.

2.4.2 A new approach: sub-nanosecond laser source

I would like to stress the main innovation of the SC laser source, represented by sub-nanosecond regime of pump, for better understanding the reasons of the choice made in our work.

The use of nanosecond pump regime in the CARS technique is not surprising. In fact, the first studies of the continuum generation, conducted by Lin and Stolen in 1976 [133], utilized a 20-kW, 10-ns dye-laser pulse. Later, Mussot *et al*. demonstrated that sub-nanosecond microchip laser could advantageously replace the nanosecond system in order to produce SC in microstructured fibers [134]. After that first demonstration, the concept of compact SC sources using microlaser has been largely studied [135], [136].

An ideal CARS imaging source would be a compact, turnkey laser system that optimizes the spatial and spectral resolution, acquisition time, penetration depth, and nonlinear photodamage. Moreover, for a nanosecond time-resolved spectroscopy both the excitation and the continuum probe should be of nanosecond duration [133].

With the use of PCFs it is possible to eliminate the need for more-complex laser systems, i.e., cavity dumped oscillators or two synchronized oscillators [105], [125], because of their high nonlinearity and the possibility to easily modify the dispersion curve profile and, consequently, change the zero-dispersion wavelength [137], [138], these fibers provide a unique media for nonlinear interactions and particularly for generating the broadband signal used as Stokes waves in multiplex CARS experiments.

As regards the spectral resolution we have to consider the pulse duration regime. It is generally valid that femtosecond pulses provide a high peak intensity that is needed for nonlinear optical processes (CARS signal is proportional to the square of the pump beam intensity and directly proportional to the Stokes beam intensity), and would result in higher sensitivity but in a low spectral resolution [139]. Indeed, in the spectral domain, the spectral width of a femtosecond pulse (~45 nm for 50 fs pulse duration) is much broader than the width of most Raman lines. As a result, most of the energy only contributes to the generation of non-resonant background. On

the contrary, the spectral width of a sub-nanosecond pulse is shorter than the Raman line width, thus the excitation energy can be easily focused on a single Raman band. Beyond the spectral resolution [124], the use of sub-nanosecond pulse increases the ratio between resonant signal and non-resonant background [139].

The use of sub-nanosecond excitation in the multiplex-CARS technique drastically improves the temporal superposition of all the wavelengths involved in the nonlinear processes and makes multicolor images recording easier [130–132], [140].

2.5 The optical fiber: a M-CARS technique improvement for SC generation

The phenomenon known as SC generation refers to the particular process that occurs when narrow-band incident pulses undergo extreme nonlinear spectral broadening to yield a broadband spectrally continuous output wave. SC generation is first reported by Alfano and Shapiro in 1970 [141] in bulk glass, and has since been the subject to several studies in a wide variety of nonlinear media, including solids, organic and inorganic liquid, gases, and optical fibers.

In the first observation Alfano and Shapiro reported the generation of a white light spectrum (the term SC has been introduced later by Manassah *et al.* in 1984) covering the entire visible range from 400 to 700 nm after propagating 5-mJ-picosecond pulses at 530 nm in bulk BK7 glass. In the case of bulk media, the broadening of the input pulses is mainly due to self-focusing phenomenon (a bulk medium whose refractive index increases with the field intensity acts as a focusing lens for the laser beam). It was observed [141–143] that the SC threshold coincided with the critical power for beam collapse that leads to an explosive increase of the peak intensity, giving rise to a range of higher-order nonlinear effects [144]. These effects produce the formation of an optical shock at the back of the pump pulses, multiphoton absorption, avalanche ionization, and the formation of a free-electron plasma [145] whose role is simply to arrest the collapse of the beam and to prevent the optical breakdown of the material. From the numerous investigations present in literature it is clear that SC generation in bulk material is a highly complex process involving both spatial and temporal effects.

In contrast, SC generation in optical fibers involves purely temporal dynamical processes. This optical waveguides represent a valid way to generate spectral broadening that propagates for long distances without significant losses, and the involved nonlinear effects (see section 2.5.3) can be controlled by changing the opto-geometric properties of the fiber. Another important advantage of the optical fibers is the possibility to realize the waveguide with different materials

(silica, tellurium...) or to introduce doping ions that change its refractive index and, consequently, modify the dispersion behavior.

The most straight-forward application for SC sources is a replacement of incoherent, white-light sources used in many characterization setups like interferometer-based dispersion measurements, broadband attenuation characterization and numerous spectroscopy and microscopy setups. The major advantage of continuum source with respect to the other systems is its high spatial coherence which allows to produce very high intensity on a very small area and during short or ultrashort time.

2.5.1 Optical fiber characteristics

Conventional optical fibers (Figure 2-8) consist typically of two concentric glass cylinders of different refractive indexes. The inner cylinder is named *core*, and the outer one is named *cladding*. If the refractive index of the core n_1 is higher than that of the cladding layer n_2, then the guidance occurs through total internal reflection at the core-cladding boundary. The possibility to modify the guidance properties by introducing a microstructure in the refractive index profile of optical fibers was suggested in the 1970s [146] and the fabrication of such fibers has become technologically commonplace since 1996. The idea was to fabricate a fiber in which light was confined and guided through a photonic band-gap effect, the term photonic crystal fiber (PCF) was introduced [147].

Photonic crystal fibers can be classified in two categories depending on the nature of the core as is shown in Figure 2-9. Microstructured fibers (MFs) possess a solid core made of materials such as silica or non-silica glasses whereas photonic bandgap fibers (PBFs) exhibit a hollow core or a core made of a dielectric whose refractive index is lower than that of silica.

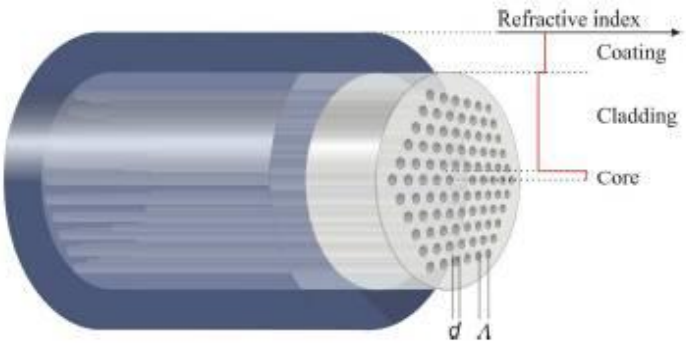

Figure 2-8: *Schematic of the classical triangular cladding single-core photonic crystal fiber. A solid core embedded in a triangular lattice of air holes with a size d and a pitch Λ, and a high index polymer of protection* **[148]**.

In the case of MFs, the air-holes around the core allow for lowering the refractive index of the cladding. Therefore light can be guided inside the core according to the principle of total internal reflection as in standard optical fibers [149]. In PBFs, the periodicity of the air-hole lattice enables to trap the light in the core by a two-dimensional photonic bandgap structure. In this class of fibers only light with a given wavelength range can be guided in the hollow or dielectric core. Figure 2-9 (bottom) illustrates the guiding principles of these two types of fiber. Photonic bandgap fibers are not generally used in the SC generation experiments, therefore, only the properties and applications of microstructured fibers will be discussed in the following paragraphs.

Two parameters that characterize the optical fiber are the relative core-cladding index difference:

$$\Delta = \frac{n_1 - n_2}{n_1} \quad \textbf{(10)}$$

and the so-called V parameter defined as:

$$V = k_0 a \left(n_1^2 - n_2^2 \right)^{1/2} \quad \textbf{(11)}$$

where $k_0 = 2\pi\lambda$, a is the core radius, and λ is the wavelength of light. The V parameter determines the number of modes supported by the fiber (generally $V < 2.405$ for single-mode fibers).

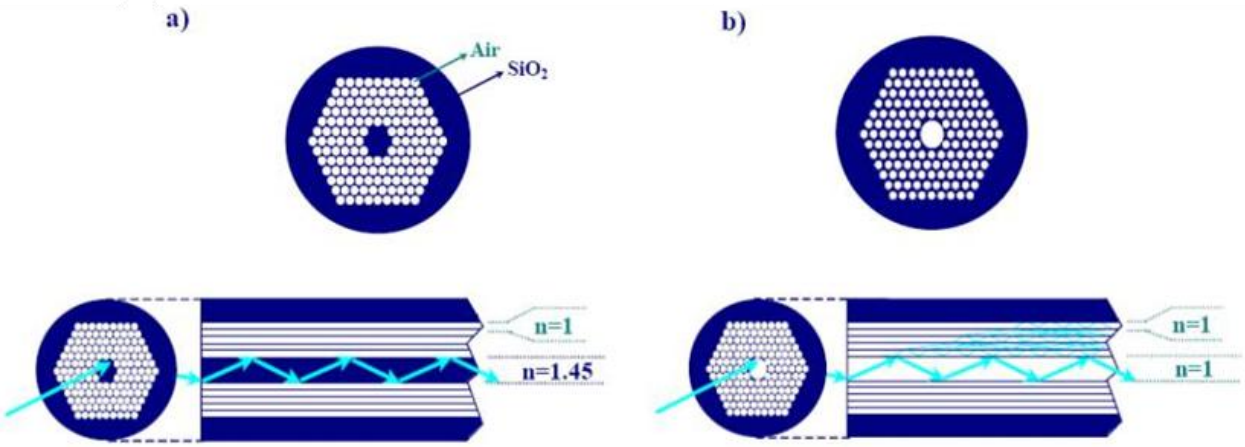

Figure 2-9: *Schematic cross-section (top) and guidance principle (bottom) of a microstructured fiber (a) and a photonic bandgap fiber (b).*

2.5.2 Linear properties of optical fiber

Fiber losses

An important parameter of the fiber is represented by the losses of the incident power through the fiber propagation. These losses depend on both the fiber material and the input wavelength. The transmitted power is defined as:

$$P_T = P_o e^{-\alpha L} \quad \textbf{(12)}$$

where α is the attenuation coefficient, and L is the fiber length. Generally α is expressed in dB/km, using the relation

$$\alpha_{dB/km} = -\frac{10}{L}\log\left(\frac{P_T}{P_0}\right) = 4.343\alpha \quad \textbf{(13)}$$

Figure 2-10 shows the loss spectrum of a silica fiber. Several factors contribute to the loss spectrum among which material absorption and Rayleigh scattering contributing dominantly. This fiber exhibits a minimum loss of about 0.2 dB/km near 1.55 μm. Losses are considerably higher at shorter wavelengths, related to the Rayleigh scattering, reaching a level of a few db/km in the visible region.

Silica glass has electronic resonances in the ultraviolet (UV) region and vibrational resonances in the far-infrared (FIR) region beyond 2 μm but has low absorption in the wavelength region: 0.5-2 μm. However, even a relatively small amount of impurities can lead to significant absorption in that wavelength window. From a practical point of view, the most important impurity affecting fiber loss is the OH ion (peak near 1.4 μm in Figure 2-10). Special precautions are taken during the fiber-fabrication process to ensure an OH-ion level of less than one part per hundred million.

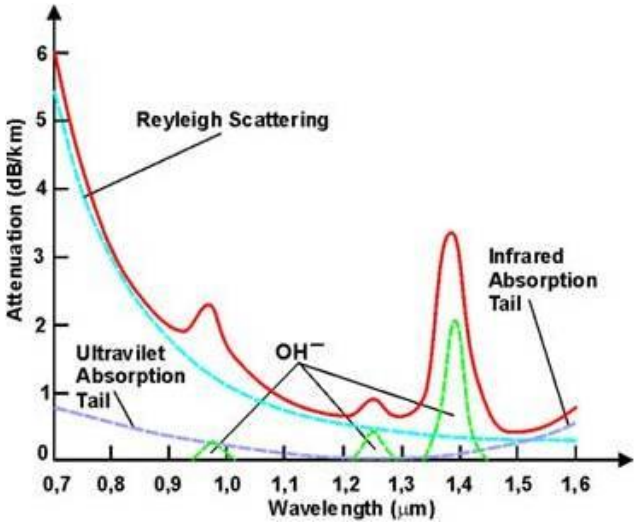

Figure 2-10: *Spectral attenuation of a silica optical fiber.*

Chromatic dispersion

An optical fiber is characterized by a specific dispersion profile (some examples in Figure 2-11) that depends on the fabrication process and on the opto-geometric proprieties of the fiber. The total dispersion can be expressed as:

$$D = D_{material} + D_{guide} \quad \textbf{(14)}$$

Consequently, it is possible to control the chromatic dispersion by doping the fiber material or by varying the guide geometry. Physically speaking, the envelope of an optical pulse moves at the group velocity while the parameter β_2 represents dispersion of the group velocity and is responsible for pulse broadening. This phenomenon is known as the group-velocity dispersion (GVD), and β_2 is the GVD parameter, equal to:

$$\beta_2 = \frac{1}{c}\left(2\frac{dn}{d\omega} + \omega \frac{d^2 n}{d\omega^2} \right) \quad \textbf{(15)}$$

Since the chromatic dispersion is due to the dependence of the nonlinear refractive index to the wavelength of the input pulses, in the optical fiber domain it is customary to express its value in $ps/(nm \cdot km)$ by the following formula:

$$D(\lambda) = -\frac{2\pi c}{\lambda^2}\beta_2(\lambda) \quad \textbf{(16)}$$

As regard the dispersion curve profile, the wavelength at that GVD vanishes, is referred to as the zero-dispersion wavelength and is denoted as λ_p. Dispersion becomes negative for shorter wavelengths, and we refer to this region as the normal dispersion regime of the fiber (D<0, β_2>0). Instead, the dispersion is positive for longer wavelength than λ_p, in the anomalous dispersion regime (D>0, β_2<0).

Nonlinear effects in optical fibers can manifest qualitatively different behaviors depending on the sign of the GVD parameter. In the normal-dispersion regime, high-frequency (blue-shifted) components of an optical pulse travel slower than low-frequency (red-shifted) components of the same pulse. By contrast, the opposite occurs in the anomalous dispersion regime. As seen in Figure 2-11, silica fibers exhibit anomalous dispersion when the light wavelength exceeds the zero-dispersion wavelength $(\lambda > \lambda_p)$. The anomalous-dispersion regime is of considerable interest for the study of nonlinear propagations because in this regime optical fibers support solitons through a balance between the dispersive and nonlinear effects, as will be discuss in the following.

An important feature of chromatic dispersion is that pulses at different wavelengths propagate at different velocities inside a fiber because of a mismatch in their group velocities.

The group-velocity mismatch plays an important role for nonlinear effects involving the SC generation in the fiber.

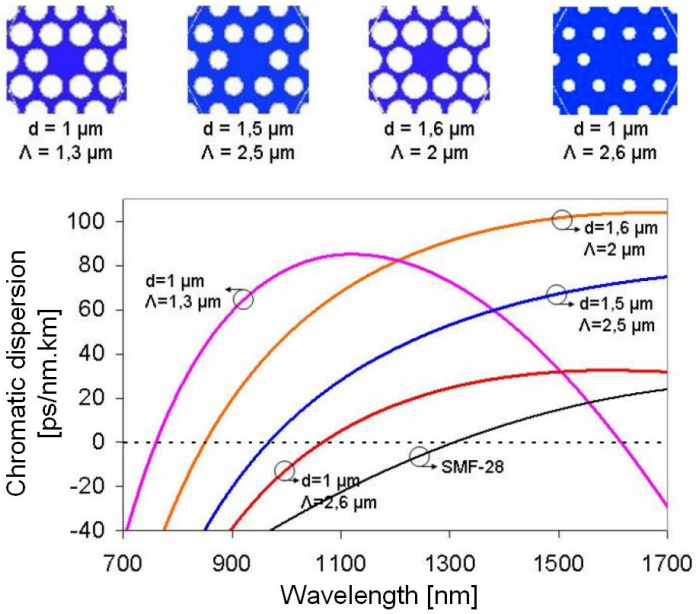

Figure 2-11: *Chromatic dispersion curves of the fundamental mode for different PCFs and for a standard single mode fibre SMF-28* **[150]**.

Birefringence

A beam light can be composed of two orthogonal electrical vector field components that vary in amplitude. Polarization occurs when these two components differ in phase or amplitude. Even a single-mode fiber is not truly single-mode because it can support these two degenerate modes. Under ideal condition (perfect cylindrical symmetry and stress-free fiber) a mode polarized in the x-direction would not couple to the mode in y-polarization state. In real fiber, because of slightly asymmetry in the fiber core cross-section along the length and because of external stresses applied on the fiber, the two polarization states are mixed.

Mathematically, the mode propagation constant β becomes slightly different for the mode polarized in x and y directions. This property is referred to as a modal birefringence and is defined as:

$$B_m = \frac{\left|\beta_x - \beta_y\right|}{k_0} = \left|n_x - n_y\right| \quad \textbf{(17)}$$

where n_x and n_y are the modal refractive indices for the two orthogonally polarized states.

The value B_m of the microstructured fibers is higher than that of conventional ones. This feature permits more efficient frequency conversions by parametric processes and represents one of the advantages of the microstructured fibers in comparison of the conventional ones.

2.5.3 Nonlinear effects in optical fiber

An electromagnetic (EM) field propagating in a medium induces a polarization of the electric dipoles. The evolution of the electromagnetic field in the medium can be described by a propagation equation derived from the general wave equation:

$$\nabla^2 E - \frac{1}{c}\frac{\partial^2 E}{\partial t^2} = -\mu_0 \frac{\partial^2 P}{\partial t^2} \quad \textbf{(18)}$$

where E is the electric field, P the induced polarization, μ_0 the vacuum permeability and c the velocity of the light in vacuum. For intense radiation such as laser pulses, the response of the medium becomes nonlinear and the induced polarization consists of a linear and a nonlinear part. In the scalar approximation, the linear and nonlinear polarizations are related to the EM field as:

$$\begin{aligned} P_L &= \varepsilon_0 \chi^{(1)} E \\ P_{NL} &= \varepsilon_0 \sum_{j=2}^{3} \chi^{(j)} E^j \end{aligned} \quad \textbf{(19)}$$

where ε_0 is the vacuum permittivity and $\chi^{(j)}$ is the j^{th} order susceptibility of the medium.

The inversion symmetry of silica glass at the molecular level allows to neglect the second higher-order susceptibilities [151]. Therefore, the relevant nonlinear effects in optical fibers are induced by $\chi^{(3)}$.

Generally, the strength of the nonlinear effects for a given waveguide mode can be characterized by a single parameter , called nonlinear coefficient [151]:

$$\gamma = \frac{n_{NL}\omega_0}{cA_{eff}} \quad \textbf{(20)}$$

where n_{NL} is the nonlinear refractive index (see (21)), and A_{eff} is the effective area of the propagation mode in the core which depends on fibre parameters such as the core radius and the core-cladding index difference but also varies with respect to the wavelength. So, for wavelengths much smaller than the core diameter, the propagation mode is mainly confined into the core. For wavelengths of the same order of the core diameter, the propagation mode tends to

widen thus increasing the effective area. Finally as the effective area is a function of wavelengths also the nonlinear coefficient turns to be wavelengths dependent.

Optical nonlinear processes can be divided in two categories: elastic processes which correspond to photon-photon interactions realised without losing energy during the process. Such effects include SPM, XPM, FWM, and modulation instability (MI).

Inelastic processes correspond to photon-phonon interactions, which leads to energy transfer between the electric field and the nonlinear medium. Such effects include SRS, and soliton self frequency shift (SSFS).

The solitonic effects in optical fibers, discussed in the end of this paragraph, are due to a combination of the effects mentioned above (i.e. SPM, dispersion, and Raman phenomenon).

Self-phase modulation (SPM)

Self-phase modulation originates from the propagating optical field intensity-dependence of the silica refractive index (Kerr effect):

$$n = n_L + n_{NL} I(t)$$
$$n_{NL} = \frac{3}{8 n_L} \mathrm{Re}(\chi^{(3)}) \quad \textbf{(21)}$$

where n_L is the linear part of the refractive index, $I(t)$ the optical field intensity, and n_{NL} the nonlinear coefficient. The refractive index increases with increasing optical intensity and this variation induces a nonlinear phase-shift of the optical wave as it propagates along the fiber. This nonlinear phase is expressed as:

$$\Delta\Phi_{NL}^{SPM}(t) = \frac{2\pi L}{\lambda} n_{NL} I(t) \quad \textbf{(22)}$$

where L is the fiber length. Due to its time-dependence, this nonlinear phase-shift translates into broadening of the optical spectrum as the pulse travels inside the fiber. In fact, in the frequency domain,

$$\Delta\omega(t) = -\frac{d\Delta\Phi_{NL}^{SPM}(t)}{dt}\ , \quad \textbf{(23)}$$

the time dependence of $\Delta\omega$ is referred to as frequency chirping. The chirp induced by SPM increases in magnitude with the propagated distance. In other words, new frequency components are generated continuously as the pulse propagates through the fiber. These SPM-generated frequency components broaden the spectrum over its initial width.

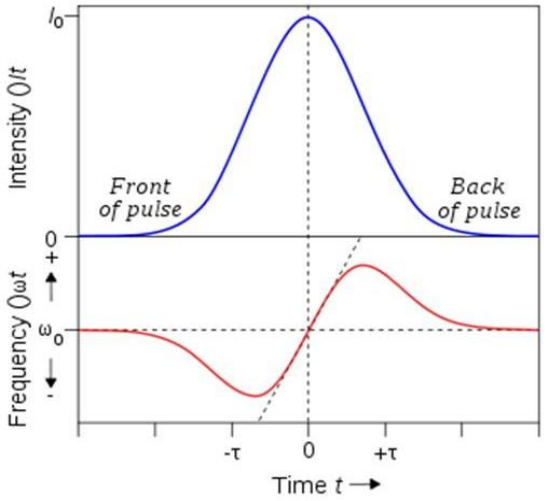

Figure 2-12: *A pulse (top curve) propagating through a nonlinear medium undergoes a self-frequency shift (bottom curve) due to self-phase modulation. The front of the pulse is shifted to lower frequencies, the back to higher frequencies. In the centre of the pulse the frequency shift is approximately linear.*

Cross-phase modulation (XPM)

When two optical fields with different wavelengths co-propagate in a fiber, the refractive index seen by one of the fields not only depends on its own intensity but also on the intensity of the other field. Consequently, the optical field with a center wavelength λ_i experiences a nonlinear phase-shift induced by the co-propagating optical field at wavelength λ_j such that:

$$\Delta\Phi_{NL}^{XPM}(t) = \frac{4\pi L}{\lambda_i} n_{NL} I_j(t) \quad \textbf{(24)}$$

We refer to this phase-shift as cross-phase modulation (XPM). This phenomenon requires the optical fields to overlap temporally.

Four-wave mixing (FWM)

Four-wave mixing is a nonlinear recombination process of photons of different energies through the third-order susceptibility. This parametric generation is only possible if there is a matching between the different phase velocities and if the total energy is conserved. There are two types of FWM process. The first corresponds to the case in which three photons transfer their energy to a single photon at the frequency $\omega_4 = \omega_1 + \omega_2 + \omega_3$. This effect is responsible, for example, of Third Harmonic Generation in optical fibers. In general, it is difficult to satisfy the phase-matching condition for such processes and to occur in optical fibers with high efficiencies. The second type of FWM (Figure 2.7) corresponds to the case in which two photons at frequencies

ω_1 and ω_2 are annihilated with simultaneous creation of two photons at frequencies ω_3 and ω_4 such that

$$\omega_1 + \omega_2 = \omega_3 + \omega_4 \quad \textbf{(25)}$$

The phase-matching condition is easy to satisfy in the case where $\omega_1 = \omega_2 = \omega_p$ .This partially degenerate case is most relevant for optical fibers, and it physically manifests in a way similar to the Raman scattering process described at the beginning of this chapter.

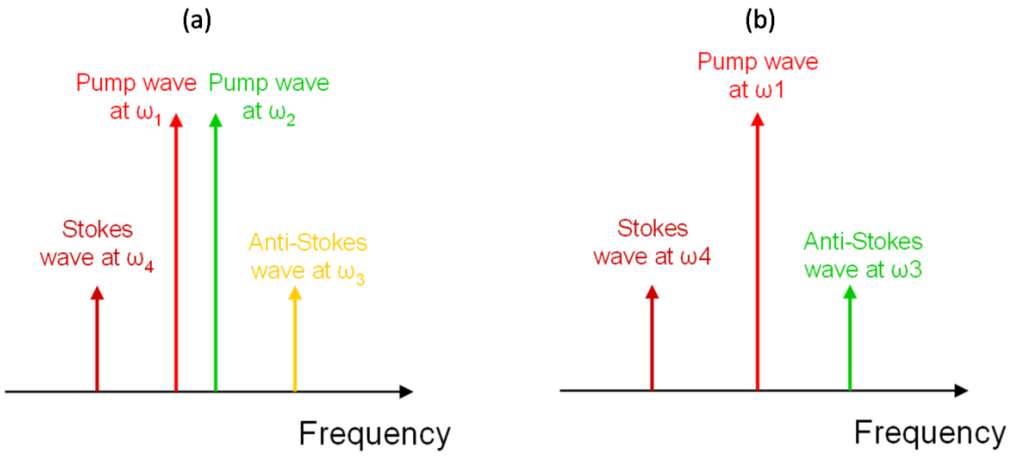

Figure 2-13: *Schematic representation of FWM in the case of (a) two pump waves and of (b) only one pump wave (degenerate case).*

Stimulated Raman scattering (SRS)

We have already treated SRS process before. Here, we briefly recall it.

SRS is a photon-phonon interaction in which the energy from an intense pump beam is shifted to lower frequencies (Stokes waves) through scattering from vibrational modes of the material molecules. Shifting of energy to higher frequencies (anti-Stokes waves) can also occur but is less efficient. SRS yields gain for a probe wave co-propagating with the pump wave and whose wavelength is located within the Raman bandwidth.

Solitonic effect

The interplay between nonlinear and dispersive effects leads to a self-induced modulation, referred to as modulation instability (MI) that requires anomalous group-velocity dispersion (GVD) and manifests itself as break-up of the continuous radiation into a train of ultrashort pulses. The physical mechanism behind MI is self-phase modulation that leads to self-amplitude modulation in the anomalous dispersion regime [152]. A consequence of MI is evident in the optical spectrum by the appearance of two symmetrical sidelobes around the pump (Figure 2-14). The combined effect of GVD and MI gives rise to solitary waves, called solitons. From a

mathematical point of view, a soliton is a particular solution of the nonlinear Schrodinger equation, whose initial symmetric amplitude can be represented by:

$$A(T, z = 0) = N \sec h\left(\frac{T}{T_0}\right) \quad \textbf{(26)}$$

In this expression, N is the order of the soliton. The case $N = 1$ corresponds to the fundamental soliton, a state in which the effects of SPM and dispersion are in balance and allows for the wave to maintain its shape as it propagates. Higher-order solitons periodically change their shape and spectrum while propagating along the fiber due to interference between the different constituents. A small perturbation affecting the relative group-velocities of the fundamental components will lead to their subsequent separation. Such process is often referred to as soliton decay or soliton breakup [153], [154]. These perturbations include higher-order dispersion, the self-steepening effect (discussed in the next subsection) and stimulated Raman scattering.

Moreover, if the temporal width of the soliton is small enough for its spectral overlapping with the Raman gain, SRS transfers continuously energy from blue part of the pulse spectrum to the red part. This energy transfer results in a shift of the center frequency of the soliton towards the infrared as the soliton propagates along the fiber. This process is commonly referred to as the soliton self-frequency shift (SSFS). As the soliton propagates along the fiber its amplitude may decrease due to the linear loss mechanisms. In that case, in order to counteract this effect, the soliton temporally broadens and this results in slowing-down the frequency-shift rate. The soliton eventually reaches a state where its optical spectrum does not overlap with the Raman gain and its central frequency does not shift any further.

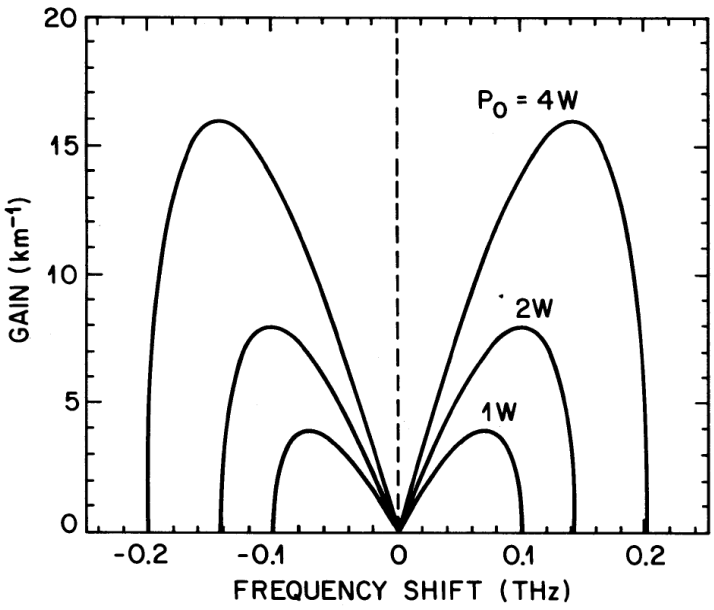

Figure 2-14: *Gain spectra of modulation instability at three power levels* **[151]**.

Self-steepening (SS)

Self-steepening (SS) results from the dispersion of the third-order susceptibility, i.e., the red frequency components experience a lower nonlinearity than blue frequency components. In the time domain, SS can be thought as the intensity dependence of the group velocity: the peak of the pulse moves at a slower velocity than the wings which induces the trailing edge of the pulse to become steeper as the pulse propagates [155]. In combination with SPM, self-steepening results in a more pronounced broadening of the blue frequency components compared to the red ones.

2.5.4 SC generation in photonic crystal fiber (PCF)

The first SC generation experiences in conventional optical fiber date back to 1976 by Lin and Stolen [133]. They used a visible ~kW peak power pulses from a nanosecond dye laser as pump beam and the generated SC was attributed to cascaded stimulated Raman scattering and SPM.

The further experiments between 1980s and 1990s, using visible pump pulses in picoseconds and nanosecond regimes, clarified the importance of the mutual interaction between Raman scattering and SPM, as well as the role of XPM and FWM in providing additional broadening [156–158]. In particular, the Raman and SPM-dominated broadening in these experiments was observed in the normal GVD domain. Instead, in the anomalous GVD regime, spectral broadening arises from soliton-related dynamics. Hasegawa and Tappert in 1973 first suggested the possibility that soliton propagation was involved in the SC generation process. Then, subsequent studies showed the existence of both fundamental and higher-order solitons that propagate in a complex manner consisting of spectral and temporal compression and splitting, followed by periodic recovery to the original pulse shape [156], [159].

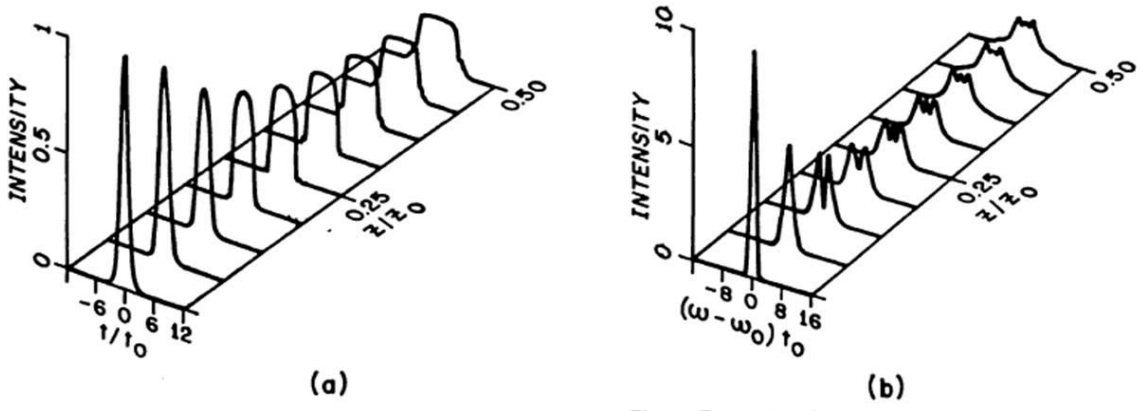

Figure 2-15: *(a) Temporal and (b) spectral shapes for a pulse as a function of the distance along a fiber for the case of normal GVD.*

In 1986 [160], [161], the interest in the solitonic phenomena lead to analyze the sensitivity of soliton propagation to perturbations such as SRS and higher-order dispersion. Intrapulse Raman scattering was found to lead to SSFS. A year later, studies on soliton fission (beak-up of the N-order soliton in N fundamental solitons) were performed [153], [154], and by 1989, also thanks to numerical simulations [162], [163], clarified that the SC generation process occurred broadly in three phases:

(i) an initial period of spectral broadening and temporal compression (due to the balance between nonlinear effects and dispersion),

(ii) a fission into a series of distinct fundamental soliton components (soliton break-up),

(iii) a continued frequency shift of these solitons (SSFS).

In particular, the second phase is interpreted, for the first time, in term of modulation instability [162], [163]. The last phase was associated with a continuous frequency shift to longer wavelengths through the Raman scattering and the generation of corresponding dispersive waves on the short-wavelength side of ZDW.

The advent of a new class of optical fibers, the photonic crystal fiber (PCF), in the late 1990s attracted widespread interest throughout the scientific community, and has led to a revolution in the generation of SC that combines ultrabroadband spectra with high brightness [164–166], a combination offered by not other technology.

The characteristics of PCF that have attracted interest relate to their guidance properties that yield single-mode propagation over broad wavelength ranges, their enhanced modal confinement and therefore elevated nonlinearity, and the ability to engineer their group velocity dispersion [167]. Moreover, the design freedom of the PCF allows to generate supercontinua by using a larger range of pump source parameters than is possible with bulk media or conventional fibers. For example, experiments have reported SC generation using input pulses from the femtosecond [127], [104], [168] to nanosecond [130], [135], [136] temporal ranges.

First Ranka *et al*. in 2000 [164] have experimentally identified the nonlinear effects responsible of SC generation in the anomalous dispersion regime of a microstructured silica fiber excited by femtosecond pump pulse. These effects, including SPM, modulation instability, soliton propagation, pulse compression, gave birth to a continuum extending from the violet to the infrared. Later, picoseconds and nanosecond sources were used to generate similar broadening in a large variety of microstructured optical fibers. SC generation in PCFs has subsequently been widely applied in interdisciplinary fields such as optical coherence tomography, spectroscopy and microscopy, telecommunications, and in optical frequency metrology [169–171].

A more exhaustive description of the nonlinear phenomena leading to SC generation is reported in Chapter 3 in our work specific case.

Chapter 3- Electro-optical pump-probe system for nsPEF bioeffect investigations

In the context of bioelectromagnetic studies, an innovative electro-optical pump-probe system specifically designed to study the interaction between electromagnetic fields (pulsed signals within the nanosecond and picosecond ranges) and biological cells was conceived during this PhD work, giving particular attention to nanoelectroporation investigations. To our knowledge, such a system is introduced for the first time in the research area of bioelectrics. The idea came from the growing interest to understand the mechanisms leading to nsPEF-induced electroporation. Real-time imaging techniques at molecular level could probably bring further advances in understanding how electric fields interact with living cells. However, the investigations at molecular level are limited by the lack of advanced instrumentations. Nowadays, the electroporation mechanisms are not yet well known because of the difficulty in performing real-time detection of this ultra-rapid and subcellular-scale phenomenon and the lack of exposure system adapted to microscopy and biological environment. Consequently, imaging of cell membrane is useful for precisely describing the events leading to membrane electropermeabilization. For all these reasons, a nonlinear imaging technique, i.e. CARS imaging, was used in conceiving an electro-optical system that serves as both electrical stimulation and optical M-CARS probe at the same time (Figure 3-1). More specifically, it consists of a fundamental laser source which is later divided in two paths: the one serves as optical trigger for the electric nanopulse generation, and the other goes to the optical probe (M-CARS source).

The Chapter 3 is organized as follows: first the electrical pump set-up is fully described and characterized; next the M-CARS set-up is presented, and finally, some preliminary results are discussed.

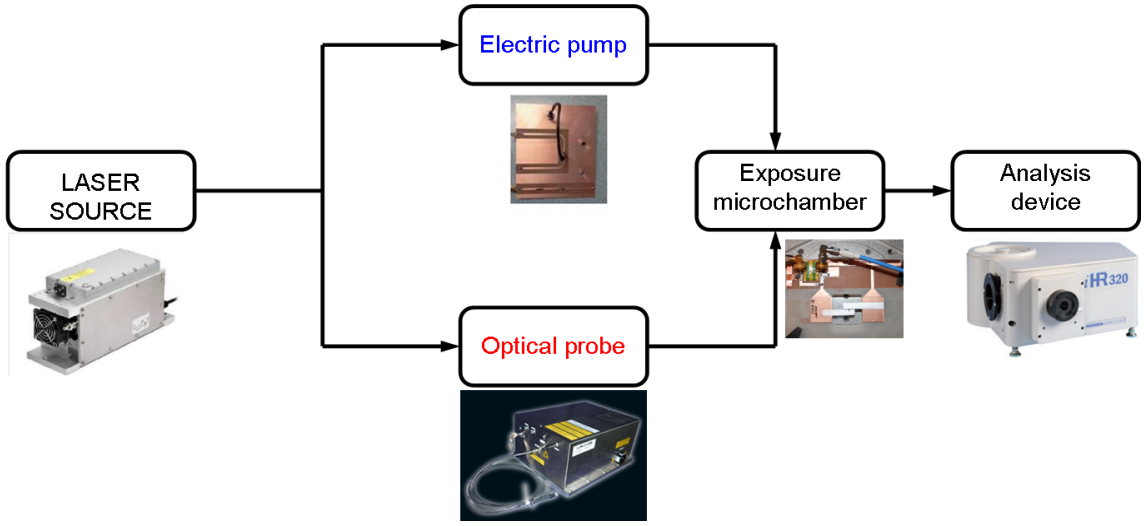

Figure 3-1: *Electro-optical illumination system layout, and the different components pictures of the system.*

3.1 The innovative feature of the system

Several electric pulse generators have already been introduced in the electroporation literature in order to provide the electrical stimulation conditions suitable for the specific investigations, as we have seen in Chapter 1. Equally, in Chapter 2 are mentioned numerous scientific papers describing white-beam laser source specifically conceived for M-CARS microscopy. The main innovation brought by the work of this thesis consists of the common sub-nanosecond laser source, used for coupling two separated systems, the electrical and the optical one, in a single compact device (Figure 3-2). Moreover, the use of sub-nanosecond regime has several advantages that lead to an easy synchronization between the two parts of the system.

The common optical source is a compact passively Q-switched powerchip laser emitting sub-nanosecond (full width at half of the maximum value, FWHM, 500 ps) pulses at 1064 nm with repetition rate of 500 Hz and average power of about 55 mW (Figure 3-2 (a)-(b)).

An overview of the electro-optical system is reported in Figure 3-2(c).

In the next sections the two main components of the system (blue and red boxes in Figure 3-2(c)) are described in detail.

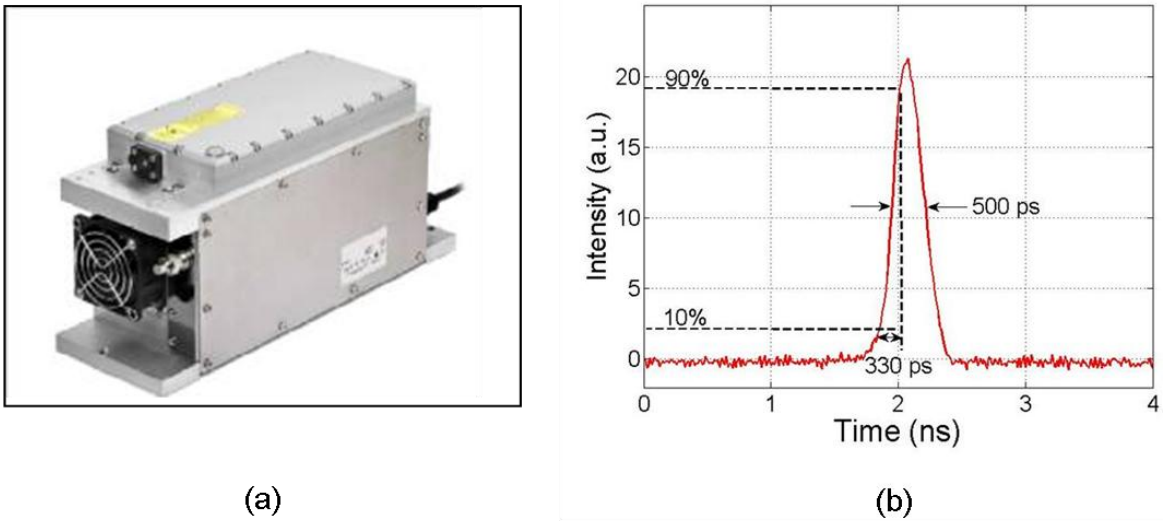

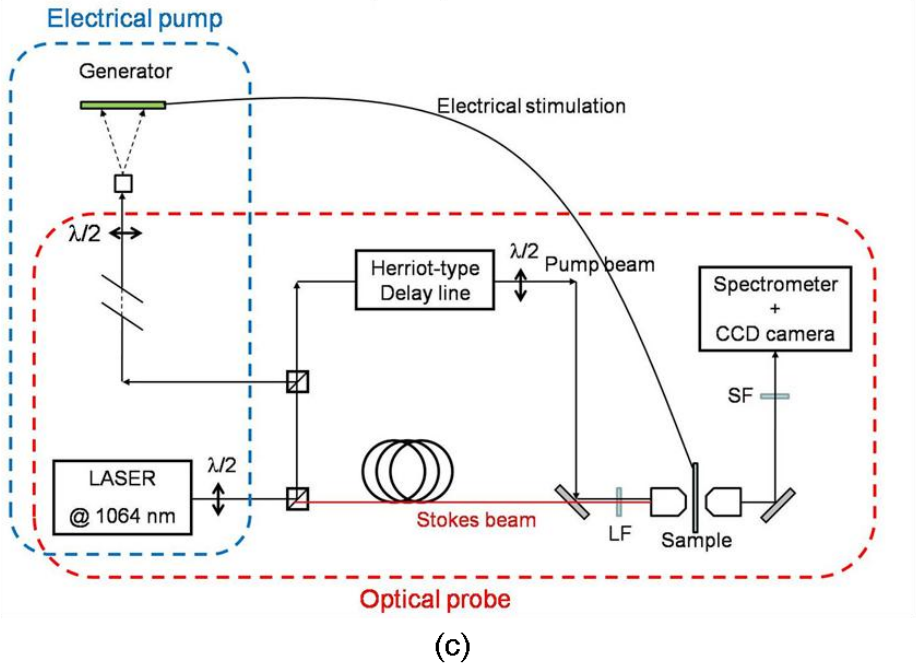

Figure 3-2: *(a) Picture of the powerchip laser source used in our set-up. (b) Powerchip laser output; pulse profile. (c) Electro-optical illumination system design. Electrical pump and optical probe set-ups are highlighted by the blue and the red box, respectively.*

3.2 Electrical pump setup

The setup is composed of three parts: optical control, generator and recording device for pulse visualization. The optical control is provided by a powerchip laser at 1064 nm producing sub-nanosecond pulses (500ps FWHMI - Figure 3-2(b)) at low repetition rate (500Hz). The laser beam is driven to the electric pulse generator through an optical pathway composed by lens in order to focus the optical energy on the switches of the generator, half-wave plate and beam

splitters (BS) to control this optical energy, and a delay-line composed by mirrors (M3-M6 in Figure 3-3) for an optimal synchronization with CARS system.

The electrical part refers to the generator and high-voltage supply source.

Finally the generated profiles are recorded by a 16 GHz oscilloscope, connected to the generator output through a SMA connector, a coaxial cable, and an attenuation chain (-76 dB at all) that guarantees a tension lower that 1 V at the oscilloscope gate. A picture of each component is reported in Figure 3-3.

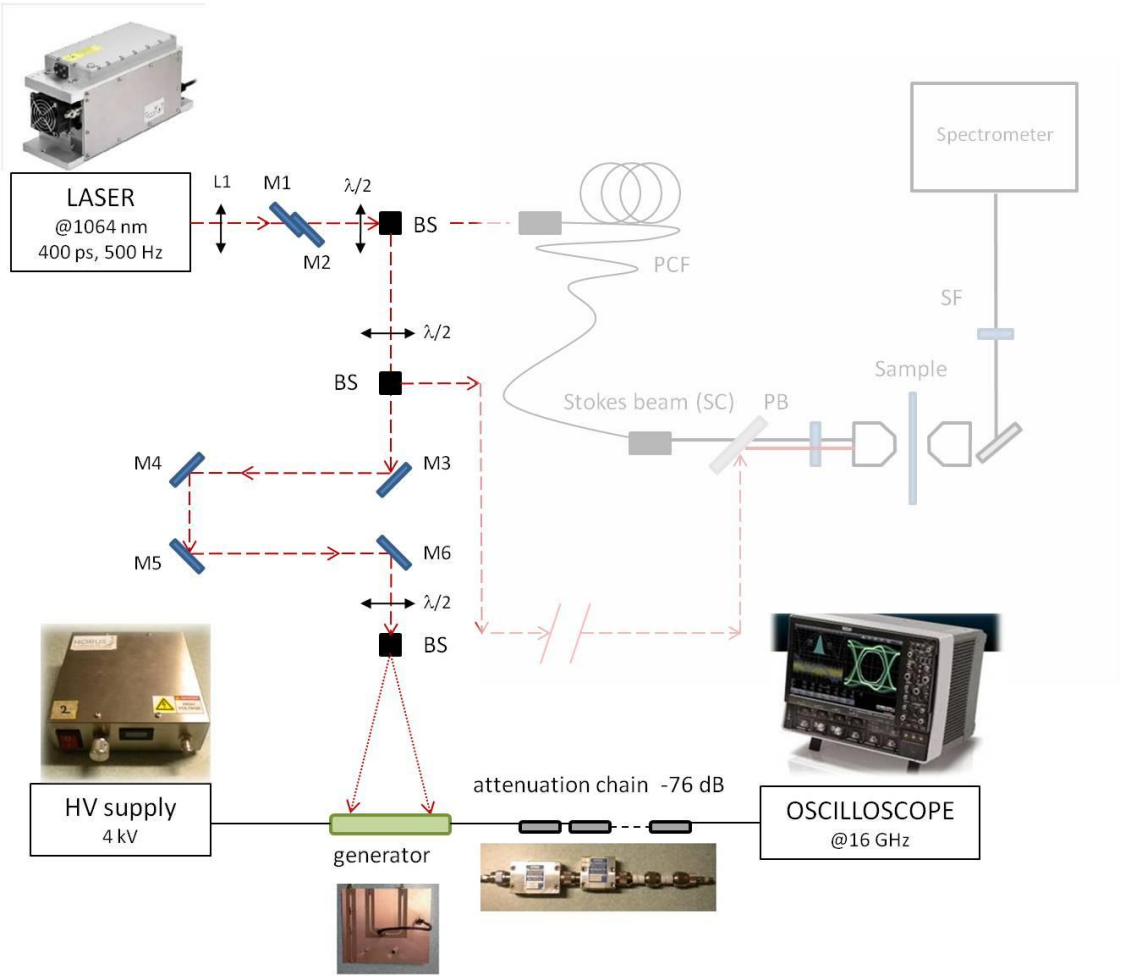

Figure 3-3: *Electric pulse measurement set-up.*

3.2.1 Frozen wave principle-based generator

This type of generator is composed of a transmission line (metallic microstrip) of a given width and length, depending on the desired line impedance and electrical pulse duration, respectively, separated from the ground plane by a dielectric substrate, as illustrated in Figure 3-4(f).

Two semiconductor switches are placed at the shortcut end and at the output end of the line, respectively. The output end of the transmission line is connected to a coaxial cable that drives the generated pulses to the matched load impedance (generally 50 Ω).

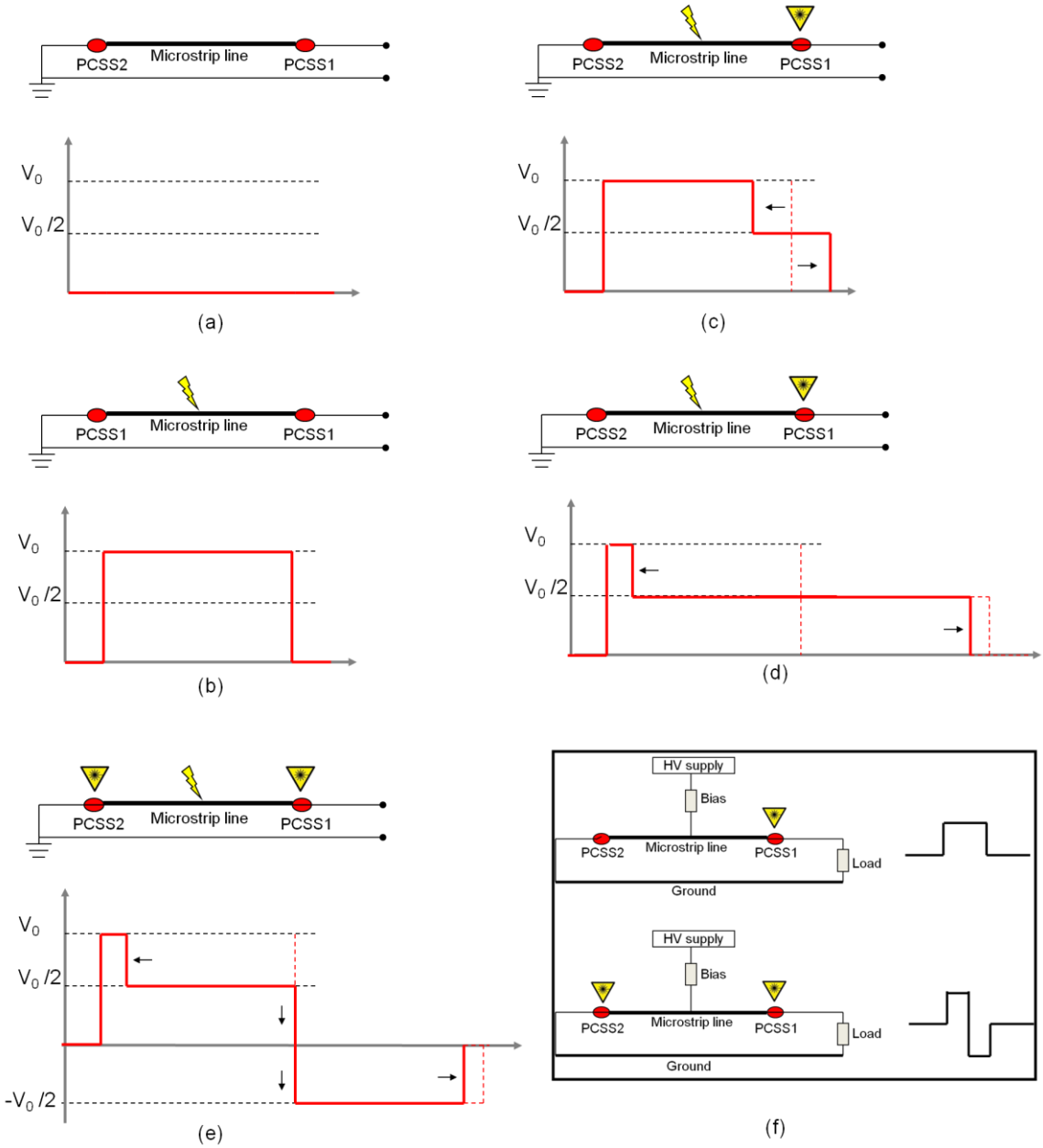

Figure 3-4: *The generator operating principle: (a) PCSSs opened; (b) the generator is charged by DC high voltage V_0, a stationary wave is generated between the PCSSs in off-state; (c) PCSS2 is illuminated by laser beam and (d) the transmitted progressive wave form an unipolar pulse; (e) if PCSS1 and PCSS2 are illuminated at the same time, both the progressive and the regressive waves are transmitted, generating a bipolar pulse. In the inset, the two triggering configurations and the respective generated pulses are reported.*

The transmission line is connected to the high voltage source (a few thousands of V) through a specific bias resistance of several hundreds of kΩ.

The operation principle is the following (Figure 3-4): (a) the supply voltage fully charges both ends of the open-circuited transmission line during the off-state. (b) A progressive wave ($V+$) towards the load and a regressive one ($V-$) towards the ground are generated and they contra-propagate through the line generating a stationary wave between the two PCSSs. (c)-(d) If only the output end switch is activated the forward output wave $V+$ delivers a pulse with the same polarity as the bias voltage to the load and with half amplitude of the bias voltage. In this case, an unipolar pulse is generated (top of the inset (f) in Figure 3-4). The pulse duration is directly dependent on the charged line length (FWHM is equal to the double of the propagation time along the line) and can be designed to produce pulses of different durations. (e) If both switches are closed simultaneously by laser beam illumination, the forward output wave $V+$ delivers a pulse like that of the previous case. The backward wave $V-$ is reflected from the short-circuited end, and undergoes an inversion of its polarity. Thus, a pulse of opposite polarity is delivered to the load, immediately following the forward pulse and a bipolar pulse is generated (bottom of the inset in Figure 3-4). In the case of a delay between the activation of the two switches, the generator is able to produce two asymmetric electrical pulses inducing large evolution of the spectral content. A detailed characterization of such generators is reported in the PhD thesis of Saad El Amari [17] as well as in [18], [72], [172].

The frozen wave generator has several advantages. For example, it permits to generate ultrashort bipolar pulses with a low amount of optical energy (order of μJ). Short pulses (shorter than a few of ns) are advantageously used to study the biological cell response because they limit ordinary electroporation effects dominant at long pulses (order of μs or ms). The high frequency components allow manipulating and exciting the internal part of the cell as nuclei and mitochondria.

Generator design and realization

The procedure for designing the microstrip line of our generator is reported in the Appendix A at the end of the manuscript. The design of the generators is presented in Figure 3-5(a). Once the line dimensions calculated and their configuration established, we have manufactured the printed circuit board (PCB) for obtaining the generators in Figure 3-5(b). The PCB consists of a thin layer of copper foil (the conductor) 35-μm thick laminated to one, or both sides of an FR-4 glass epoxy panel (the dielectric with ε_r=4.6) 1.6-μm thick. The lines are drilled through the board using an automated drilling machine. Following drilling, the board is scrubbed to remove fine copper particles left by the drill (Figure 3-5(b)). The width of the microstrip is 3 mm, such a width has been calculated for obtaining microstrip line impedance of 50 Ω (Appendix A). Next, we completed the PCB with the supply and load connections (SMA connectors) and the laser-triggered PCSSs.

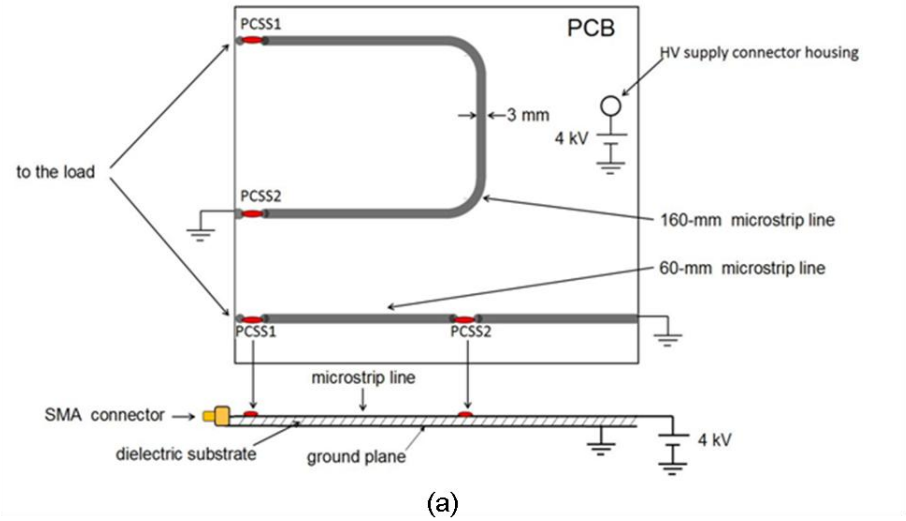

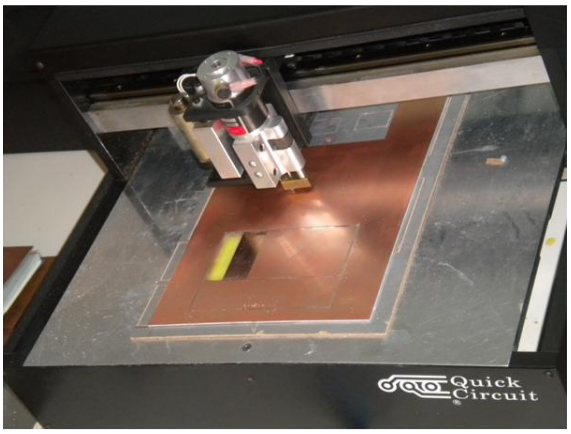

(b)

(c)

Figure 3-5: *(a) Schematic design; (b) picture of the automated drilling machine used to print the microstrip line on PCB; (c) manifactured nanosecond generators; 2-ns pulse generator on the top and 1-ns pulse generator on the bottom.*

Because of the main role played by the PCSS in the pulse generation, the following section is dedicated to the description of the optoelectronic component in order to clarify the reasons of our choices.

Optoelectronic switching for ultrashort electrical pulse generation

In its general definition, a switch can be described as two terminals device separated by a material medium (Figure 3-6). In the 'open' state (off-state) the switch medium is a good electrical insulator while in the 'closed' state (on-state), the switch medium is a good electrical conductor. The process of switching is thus the process of changing the switch medium from an insulator to a conductor by producing a specific carrier density related to the desired switch

conduction resistance. In particular, a photoconductive semiconductor switch is an optoelectronic device based on the conversion process from light to current or voltage. In our case the switch is realized by using a fast semiconductor diode designed on a silicon substrate (Figure 3-6). When a photon of sufficient energy strikes the diode, it creates electron-hole pairs. If the absorption occurs in the junction's depletion region, or one diffusion length away from it, these carriers are swept from the junction by the built-in field of the depletion region. Thus holes move toward the anode, and electrons toward the cathode, and a photocurrent is produced. This photocurrent is the sum of both the dark current (without light) and the current induced by incident photons. In all cases, the dark current must be minimized to enhance the sensitivity of the device.

The PCSS shown in Figure 3-6 consists of a block of semiconductor material of length h_s , width w_s, and thickness d_s . Thickness d_s should be more than or equal to optical absorption depth d_o to ensure that all of the optical energy is being absorbed in the bulk of the switch. The length of the switch h_s is determined by the dielectric strength of the semiconductor surface in (Figure 3-6(a)).

$$h_s = \frac{V_o}{E_m} \quad \textbf{(27)}$$

where V_o is the maximum voltage that is applied to the switch, and E_m is the operating surface electric field with a value of up to 90 kV/cm for Silicon and 140 kV/cm for Gallium Arsenide (GaAs) [173]. The width w_s of the switch is determined by the current density required to avoid filamentary conduction, in which a relatively small area carries a large amount of current (a current flow restricted to smaller area is called as filament). The insulating, photoconductive medium is changed into a conductor by illuminating the face of the switch with a uniform optical intensity between the contacts.

Figure 3-6: (*a) schematic design and (b) section photo of the PCSS used for the generator.*

We can classify the switches according to their operation mode in linear and avalanche (or non linear) switch.

Linear PCSS

The linear mode is characterized by one electron-hole pair produced for each photon absorbed. Therefore, the conductivity of the material is, to the first order, linearly proportional to the total photon flux illuminating the semiconductor material, and the switch conductivity approximately follows the rise time of the optical pulse. The switch closes as the optical intensity increases, remains closed while illuminated, and opens with a characteristic time constant related to the carrier lifetimes after the optical pulse is removed.

Non-linear PCSS

In a non-linear PCSS, like as GaAs switch, when the bias electric field across the switch exceeds a threshold (approximately 4-8 kV/cm), a transition occurs to a nonlinear mode that exhibits high gain and extended conduction. This is referred to as the lock-on mode [174]. In the lock-on mode the field across the switch drops to 3-5 KV/cm, but the current does not decrease and continues to flow as if it has locked on to a value. In the lock-on state the laser pulse can, if strong enough, determine the closing time of the switch, as in the linear mode, but the switch then remains closed or "locked-on" until the current is interrupted by the external circuit.

In summary, when the non linear electric field threshold for GaAs is reached, the turn-on speed of the switch is determined by the avalanche process, in which carriers are generated by impact ionization, independent of the laser rise time. The pulse amplitude locks on to a characteristic electric field until the current through the switch is turned off.

If the laser rise time is shorter than the avalanche rise time and the laser amplitude is high enough, the optically generated carriers can dominate, and the switch turn-on time is shorter than its characteristic avalanche time. The switch will still lock-on even though the optical pulse from the laser may have ended.

We chose the linear Silicon PCSS for our generator because of its very easy optical control (two switches can be closed within an adjustable temporal difference from picoseconds to several nanoseconds by adjusting the optical path length from a common optical source to the switch), low conduction losses and a very low jitter [175].

In the characterization of the PCSS we need to consider the PCSS physical and electrical parameters: recombination rate, open resistance and closed resistance. The recombination rate depends on material properties, electric field, temperature and surface conditions. Without electric field the carriers freely move following a Brownian movement with a velocity that

depends on the temperature as well as the effective electron mass. In presence of electric field the carrier movement is accelerated and their energy increases with collisions. Whenever the thermal equilibrium is disturbed, processes exist to restore the system equilibrium. In the case of the injection of excess carriers, the mechanism is the recombination of minority carriers with the majority carriers. The recombination rate is made faster by the presence of impurities in the semiconductor. The open or "off state" resistance, R_{off} of the switch is determined by the dark or steady state resistivity of the semiconductor slab, ρ_0 (h_s, w_s and d_s being semiconductor dimensions, see Figure 3-6(a)):

$$R_{off} = \frac{\rho_0 h_s}{w_s d_s} \quad \textbf{(28)}$$

The conduction or "on state" resistance of the PCSS is given by [176]:

$$R_{on} = \frac{h_s^2 E_p}{(1-r)\mu_s q_e E_0} \quad \textbf{(29)}$$

under the assumption that the material recombination time T_r *is* much greater than the electrical pulse, where

h_s = height of switch

E_p = photon energy

q_e = electron charge

E_0 = total optical energy incident on the photo-switch

μ_s= sum of hole and electron mobility

r = surface reflection coefficient

A linear photo-switch is desirable because the conduction resistance can be determined by controlling the optical source. In this case, electric energy is linearly proportional to the optical energy. One can consider two cases. If the recombination time is much shorter than optical pulse duration, then the electrical pulse profile follows the optical one (Figure 3-7(a)). On the contrary, if the recombination time is much longer than optical pulse duration, the rise front of the electric pulse follows the optical one, but its duration depend on the number of the stored charges and the fall time correspond to recombination time (Figure 3-7(b)).

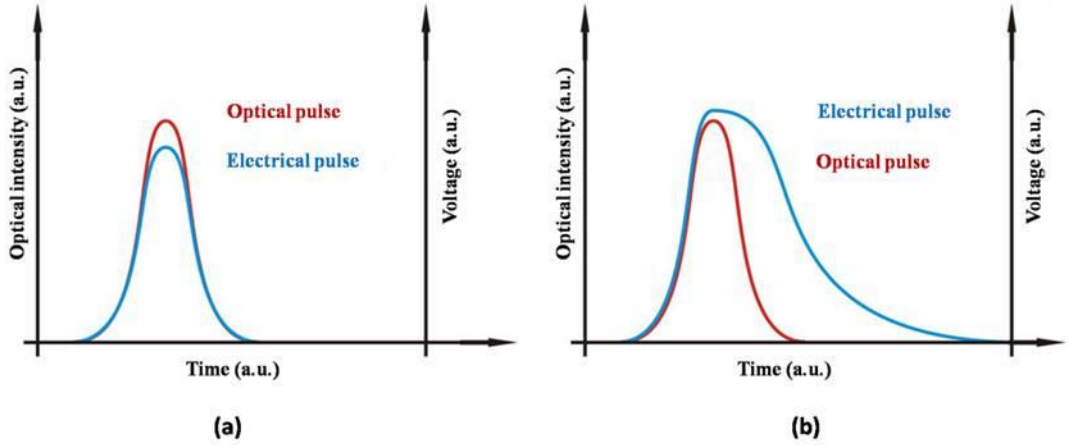

Figure 3-7: *Example of electrical pulse controlled by the optical one in the case (a) Tc << optical pulse duration, and (b) T_c >> optical pulse duration.*

Moreover, we need to obtain R_{on} as small as possible in order to maximize the transmitted energy to the load.

An estimation of the conduction resistance and efficiency has been made and published in collaboration with Saad El Amari by using the following electrical scheme [172].

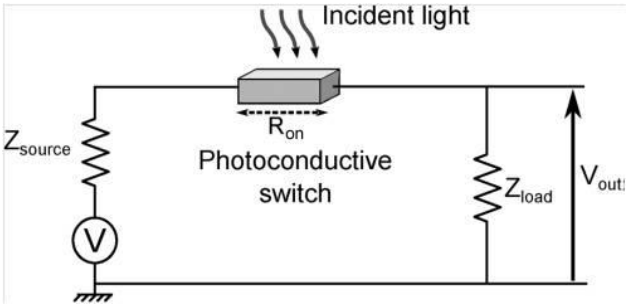

Figure 3-8: *Equivalent circuit of pulse shape generator in the on-state* [172].

Practically, the switch conduction resistance is chosen to be a small fraction of the sum of the source and load impedances [176]. Consequently, in order to experimentally determine R_{on}, we used the following expression:

$$R_{on} = \frac{(V - V_{out}) \times Z_{load}}{V_{out}} - Z_{source} \quad \textbf{(30)}$$

where V is the bias voltage, V_{out} is the output voltage, Z_{load} and Z_{source} represent the real part of the respective impedances of the load and the generator.

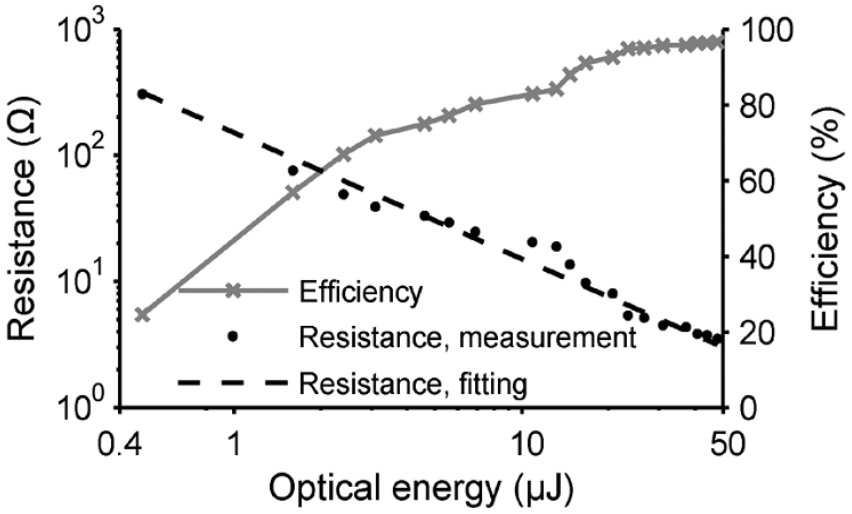

Figure 3-9: *PCSS resistance and voltage-switching efficiency versus the optical pulse energy for 4-kV bias voltage* [172].

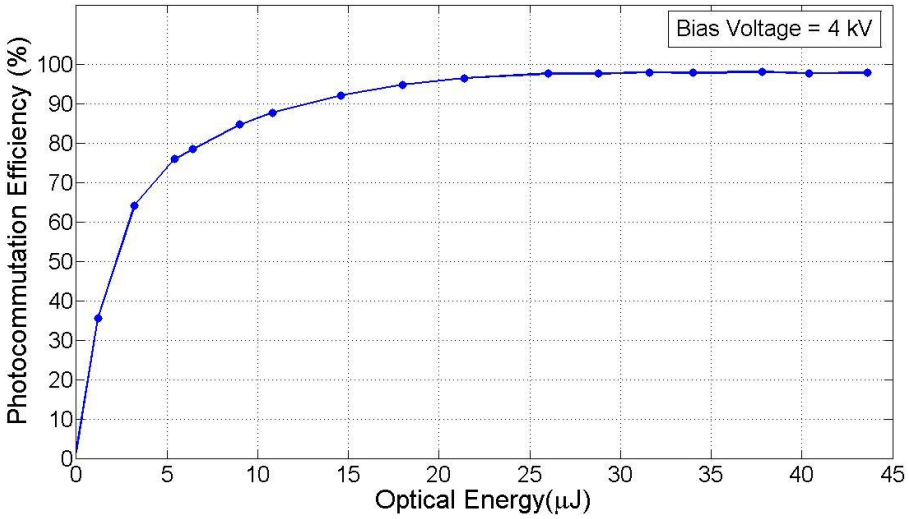

Figure 3-10: *Photocommutation efficiency of the PCSS versus optical energy sent on the switch.*

The photocommutation efficiency in percentage is estimated as:

$$Efficiency(\%) = \frac{V_{out}}{V/2} \times 100 \quad \textbf{(31)}$$

Figure 3-9 shows the PCSS resistance and voltage-switching efficiency as a function of the optical energy. The "on state" resistance of the photoconductive device decreases proportionally to the inverse of the optical energy. The small value reached by the semiconductor resistance (3.8 Ω) guarantees a large optoelectronic switching efficiency for a generator designed with a 50 Ω coaxial line [172]. In addition, we show that in the case of 4 kV linear Si switches polarized with 300 V, a 7 μJ optical energy is sufficient for obtaining efficiency > 95%, while for polarization

voltage of 4 kV, photocommutation efficiency is > 95% with optical energy equal or higher than 20 µJ. This optical energy evolution is induced by the central absorption wavelength shift of the semiconductor under bias voltage increase [177]. These results agree with the efficiency estimation of the switch used in our generator configuration (Figure 3-10).

PCSSs can be fabricated from Si or any other semiconductor material (GaAs or Ge for example). The basic requirement is that it should be able to support a high voltage bias in the off-state and allow for a fast rise time in the on-state that means more energy transfer to the load. Additionally, the absorption spectrum of the semiconductor has to match the wavelength emission of compact pulsed laser sources.

Table 3 summarizes the intrinsic properties of each semiconductor. GaAs is preferred over Si because of its superior electrical characteristics, nevertheless, for ultrashort electrical pulse generation, embedded in such an electro-optical system, we prefer silicon semi-conductor because it permits an easier synchronization between electrical and optical pulses.

Additionally, silicon can be activated with infrared laser source emitting radiation close to 1.06 µm which are largely developed and commercialized. Mode locked or Q-switched lasers producing powerful picosecond to nanosecond pulses are easily available.

The detailed study and characterization of optoelectronic components of our generator permitted to estimate the optimal conditions in terms of semiconductor material and optical energy for an efficient photocommutation.

Table 3. Intrinsic characteristics of Silicon, Germanium and Gallium arsenide**.**

Features	Si	GaAs	Ge
Energy gap (eV) at 300 K	1.115	1.4	0.665
Carrier intrinsic density (cm^{-3}) at 300 K	$1.5\ 10^{10}$	$1.1\ 10^{7}$	$2.4\ 10^{13}$
Intrinsic resistance (W cm) at 300 K	$2.3\ 10^{5}$	10^{8}	47
Electron mobility ($cm2\ V^{-1}\ s^{-1}$)	1350	8500	3900
Carrier mobility ($cm2\ V^{-1}\ s^{-1}$)	480	400	1900
Wavelength (nm)	1128	886	1870
Recombination time (s)	10^{-5}	1	1

The features of our PCSS are:

- high dielectric strength up to 20 kV;
- low jitter (< 2 ps) permitting the synchronization between our generator and the real time imaging optical system;
- low intrinsic resistance (< 3 Ω) for diminishing the transmission line discontinuities
- linear regime of working permitting reproducible electrical pulse generation
- optical energy sent to each switch of 20 μJ for a bias voltage of 4 kV
- optical absorption close to 1 μm.

3.2.2 Characterisation of generated ultrashort pulses

For recording the generated ultrashort pulse profiles we used a 16-GHz band-pass oscilloscope, connected to the generator output by SMA cables and a chain of attenuators (-76 dB) for avoiding a voltage higher than 1 V at the oscilloscope input gate. The PCB generator is mounted on a support translating along x, y, and z axis for easily and better switch illumination. The switches are illuminated by the optical beam of the powerchip laser that represents the optical control and permits to send optical pulses with energy up to 20 μJ at a repetition rate of 500 Hz. In Figure 3-11 unipolar and bipolar profiles of the electrical pulses generated by the shorter and the longer line respectively, are showed.

Because of the bias voltage is 4 kV we expect the amplitude is 2 kV for unipolar pulse and 4 kV (peak to peak) for bipolar ones (Figure 3-11). As we can see, the longer line that generates 2 ns (FWHM) pulse (Figure 3-11(b)) presents best performances than the shorter one (1 ns FWHM), with an amplitude equal to 97% of the expected value for the unipolar case. In the bipolar pulse we obtain a peak-to-peak amplitude not higher than 84% of the bias voltage. The profile degradation that we observe in the negative lobe is due to the residual resistance of the switches which is equal to about 3 Ω [17] and not to zero as in the ideal case. Additionally, the regressive wave giving birth to the negative pulse part propagates through two PCSSs before reaching the load, instead the progressive wave passes through only one PCSS. In these conditions a difference of amplitude is observed between the positive and the negative pulse lobes constituting the output signal.

At constant input optical power, the R_{on} residual resistance of the PCSS is bias voltage dependent because of the F. Keldish effect which shifts the absorption of the semiconductor toward higher wavelengths. Then, for a given input optical energy, the switching efficiency can be reduced. The shorter pulse obtained with the 60-mm long microstrip line generator (see Figure 3-5) does not have the expected shape and peak-to-peak voltage. Indeed, since the optical pulse rise time has

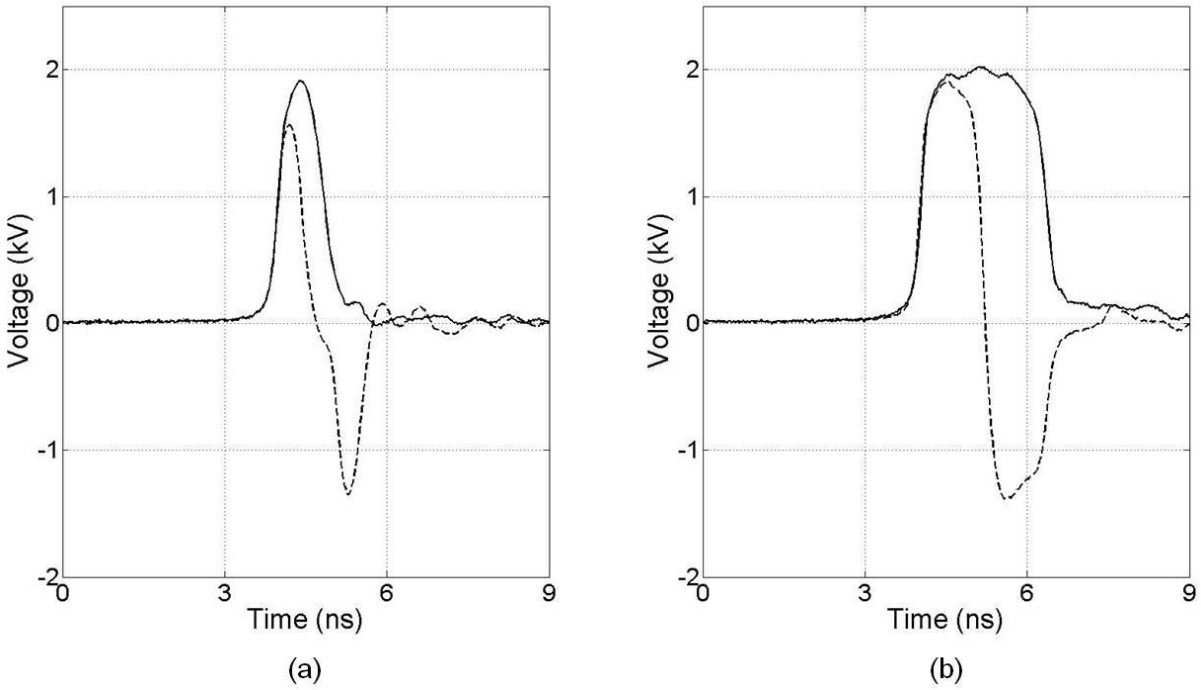

Figure 3-11: *Unipolar and bipolar pulse profiles generated by (a) the shorter line and (b) longer line.*

longer duration than the propagation time of the electrical pulse along microstrip line, the progressive wave reaches the load before a complete and efficient switching. Then, the Ron is larger and the peak to peak output pulse voltage is reduced. Additionally, an indirect transition between positive and negative components of the bipolar pulse is visible (Figure 3-11(a)). That effect is due to the microstrip line located between the second semiconductor and the ground. Before reaching the progressive wave, the regressive one has to propagate all along that path which induces a temporal delay between the two negative and positive pulse components.

We also simulated the generated pulse with PSPICE software. The SPICE model is reported in Figure 3-12, where the main generator components are shown including the power supply (4 kV) with a bias resistor of 1 kΩ, two PCSSs, an ideal transmission line (TXL), and a matched 50 Ω load.

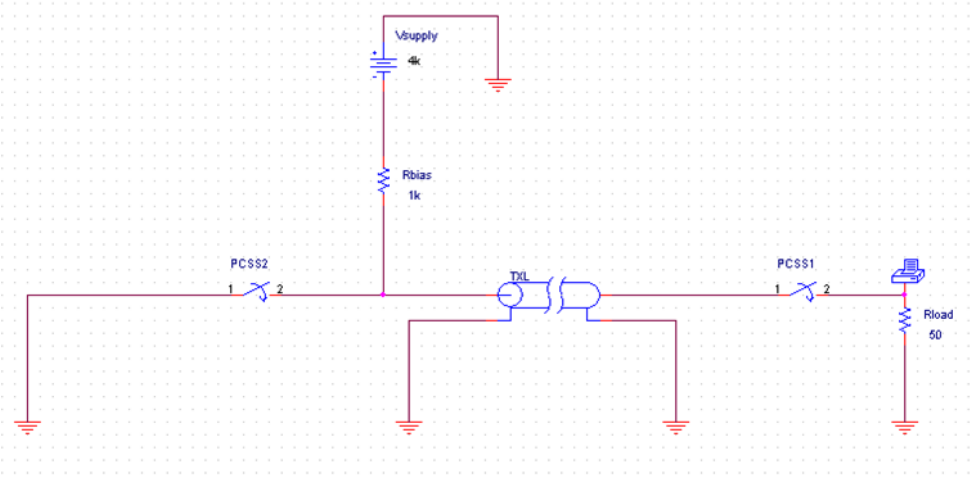

Figure 3-12: *SPICE model of longer frozen-wave-principle based generator.*

The commutation time of PCSSs is set to 230 ps, the resistance of open and closed state is of 1 MΩ and 1 Ω, respectively. Moreover, the propagation delay of the transmission line is equal to half of the pulse duration, and then is set at 500 ps and 1 ns for simulating the shorter and the longer line, respectively. As we can see in Figure 3-13 we obtained a good match between the simulated (continuous red curve) and the measured (dashed black curve) profiles. However, the duration of the simulated pulses is shorter than the measured ones. This difference is due to the delay of the transmission line fixed in the simulations (Figure 3-5(b) on the bottom).

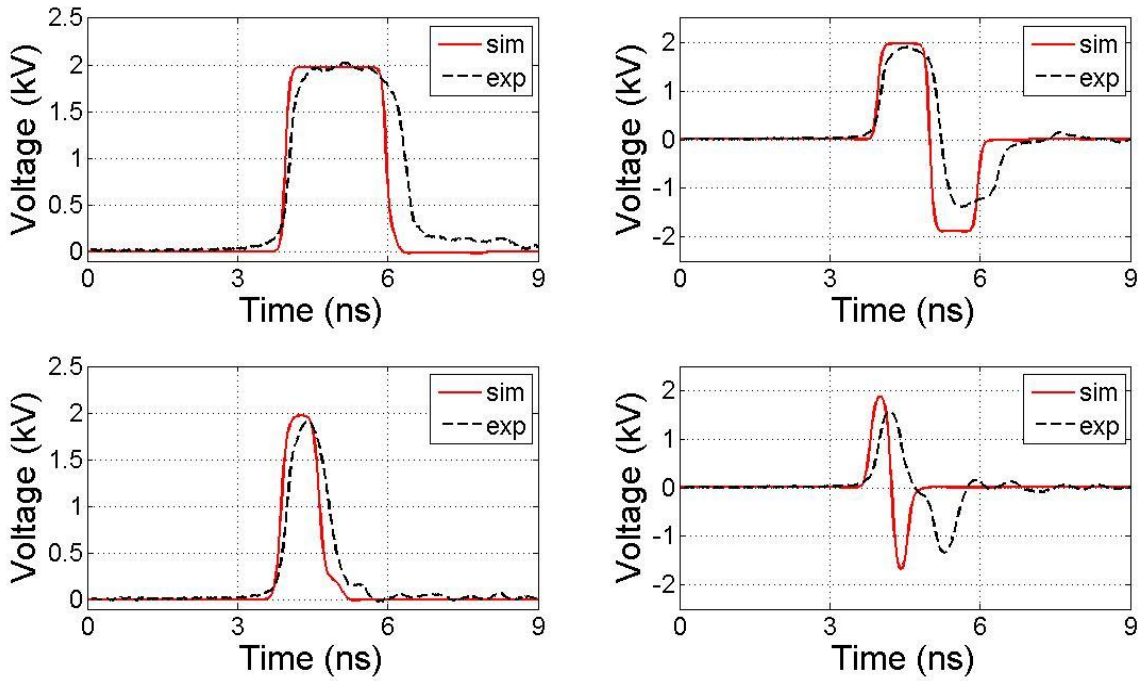

Figure 3-13: *Simulated (continuous red line) and generated experimental pulses (dashed blue line).*

In a second time, in order to confirm our hypothesis about the causes of the mismatches between the simulated bipolar pulses and the recorded ones, a residual resistance of 3 Ω is introduced in the simulation and the transition time of each switch is increased. Next, a transmission line is also added, taking into account the line connecting the PCSS2 and the ground in the shorter pulse generator (Figure 3-14). The comparison between the new simulated and experimental profiles is shown in Figure 3-15.

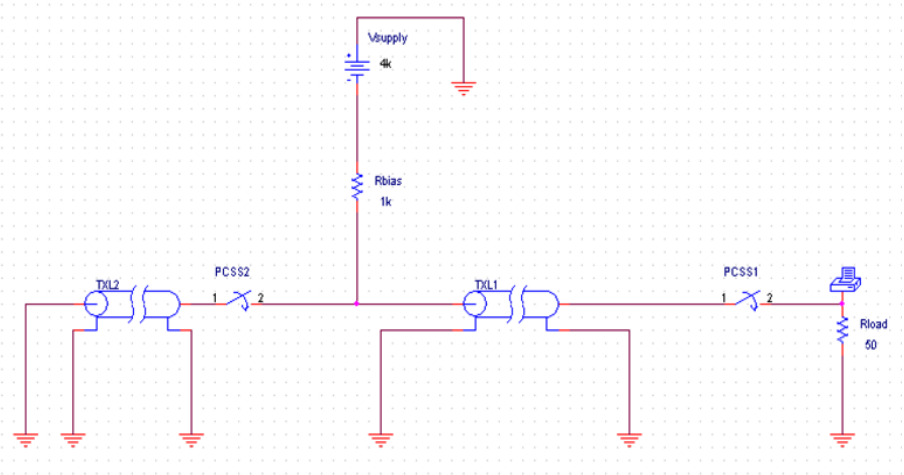

Figure 3-14: *SPICE model of shorter frozen-wave-principle based generator.*

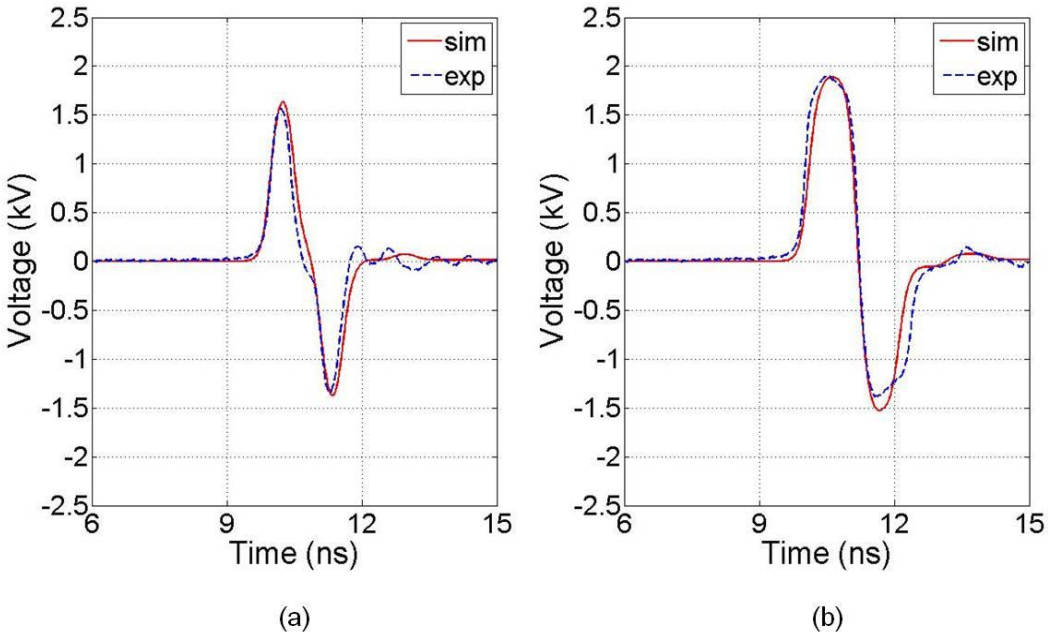

Figure 3-15: *Bipolar pulse profiles simulated by introducing the losses (continuous red line) and experimental pulse profiles (dashed blue line), for (a) the shorter pulse generator and (b) the longer one.*

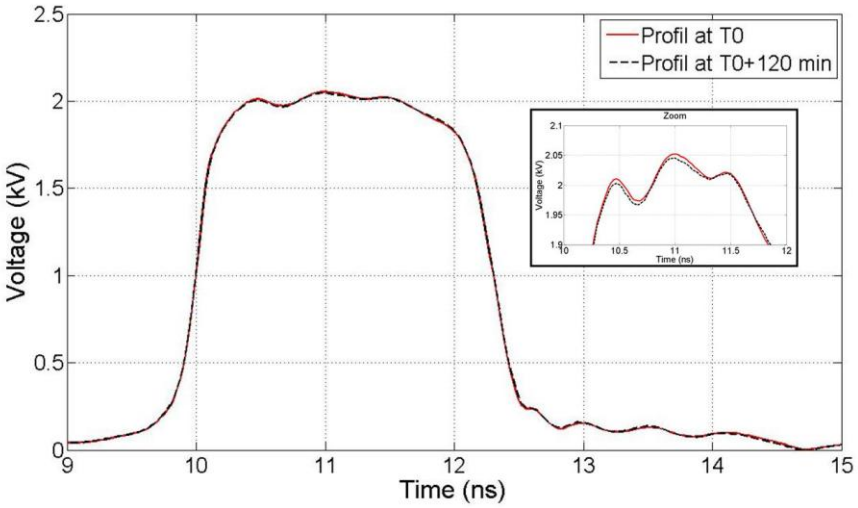

Figure 3-16: *Pulse profiles recorded a T0 and after 2 hours for testing the generator stability.*

For a complete characterization, we experimentally analysed the generator stability by recording pulse profiles at T0 and T0+120 minutes. As we can see in Figure 3-16 the generator shows an amplitude stability of > 99%. After 120 minutes the pulse duration is exactly the same of the first measure.

We also verified the optimum pulse shape reproducibility (Figure 3-17) by recording the electrical pulse after removing and replacing several times the generator ahead the incident optical beam and with a delay of 10 days. Minor differences are observed which clearly show the performances of our generator.

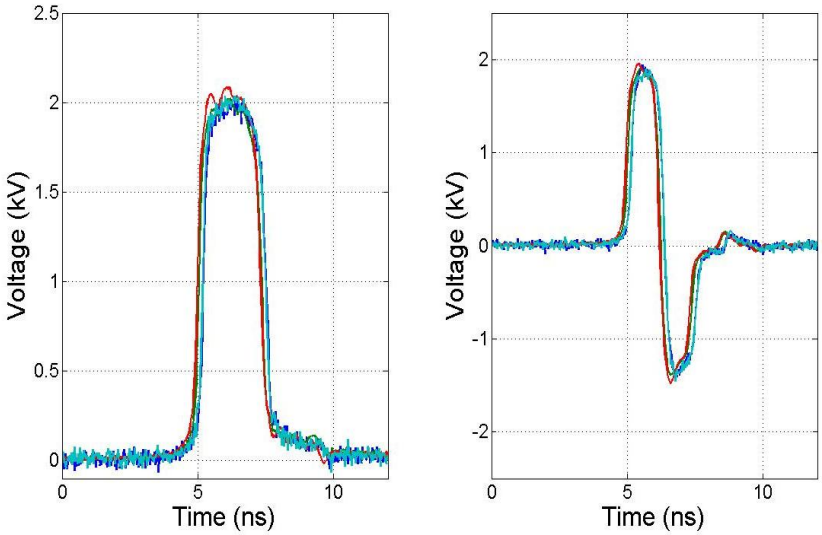

Figure 3-17: *Four generated pulse profiles recorded by changing the measurement parameters and in different days for testing the reproducibility.*

3.3 A nanopulse delivery device prototype

Since a complete exposure system consists of an electric pulse generator and an delivery device that allows electric pulses to be applied on the sample, we have designed a prototype of microchamber (Figure 3-18), useful for cell real-time detection under microscope, on the base of that described in [20]. The microchamber is composed of two electrodes, pasted in parallel so as forming a channel on the microscope glass where cells in solution can be injected (Figure 3-18). The electrode material is generally platinum or gold for their electrical properties and their good biocompatibility [178]. The channel height is represented by the electrode thickness, whereas its width is adjusted with electrode distance depending on the electric field to apply (order of several MV/m). The channel length is generally chosen for obtaining a load impedance of 50 Ω.

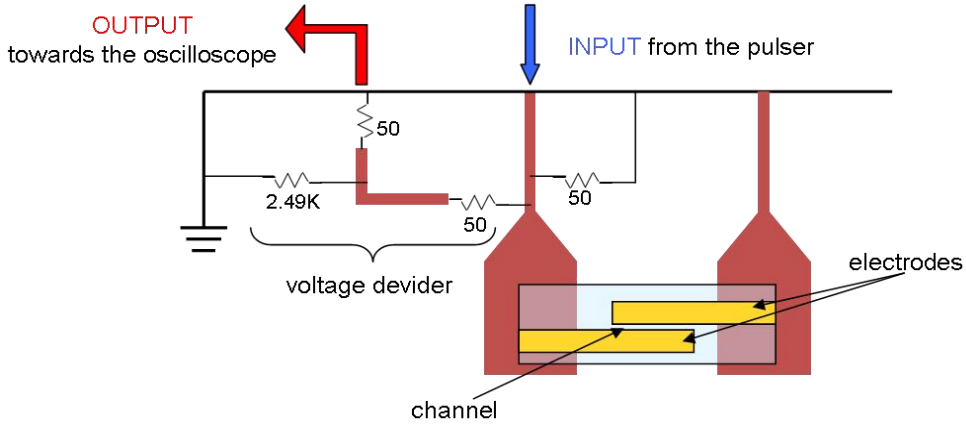

(a)

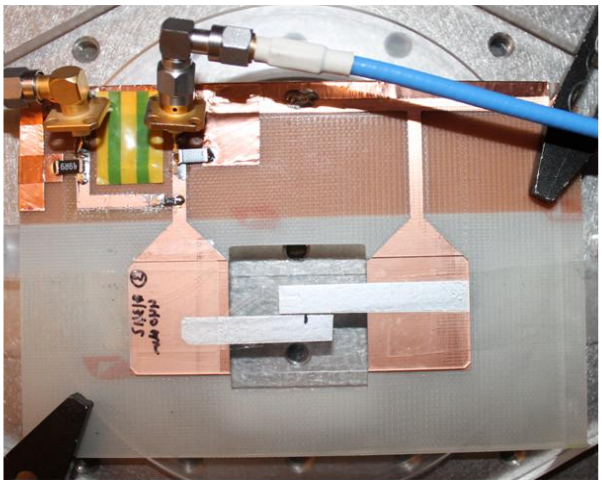

(b)

Figure 3-18: *(a) Design of delivery device prototype; (b) picture of the realized delivery device.*

We can describe the microchannel with a parallel GC model, where:

$$C = \varepsilon_r \frac{hL}{d} \qquad G = \sigma \frac{hL}{d} \quad \textbf{(32)}$$

Then, the load impedance results:

$$Z_{load} = \frac{1}{G + j\omega C} = \frac{d}{hL(\sigma + j\varepsilon_0 \varepsilon_r \omega)} \quad \textbf{(33)}$$

As we can see from the equation (33), the load impedance depends on the microchamber dimension and the electromagnetic properties of the biological medium (conductivity σ=1.4 S/m and relative permittivity ε_r=78 [74]). At low frequencies, the impedance is manly provided by the conductivity σ. At the transition frequency ($f_t = \frac{\sigma}{2\pi\varepsilon_0\varepsilon_r} = 231MHz$), the contributions of σ and $\varepsilon_0\varepsilon_r\omega$ are equal. Beyond this frequency, the imaginary part of the impedance is no longer negligible. According to these frequency indications, we can estimate the pulse duration that can be applied without too much distortion. Considering the spectral range of the applied pulse (0-500 MHz for 2-ns pulse, up to 1 GHz for the <1ns pulse), the transition frequency should be extended by increasing the biological solution conductivity in order to apply ultrashort pulses (< 10 ns). Regarding the microchamber impedance, in order to match the 50-Ω impedance generator, we would need a channel dimension larger than that permitted by the microscope stage where the microchamber is mounted. With the allowed dimensions we obtain a microchamber impedance of several hundred of Ohms. Consequently, an easy way out is to put a 50-Ω resistance in parallel to the high biological solution resistance (~400 Ω at low frequencies). The microchamber prototype is provided also with a voltage divider stage for pulse measurement. The voltage devider consists of a 2490-Ω resistance in series with the parallel of a 50-Ω resistance and the 50-Ω input resistance of the oscilloscope (Figure 3-18).

Before passing to the description of the optical probe, the key-points of the electrical pump presented here are summarized. The electric field exposure system consists of a nanosecond high voltage pulse generator and the delivery device. The pulse generator is designed in order to provide a robust, flexible and user-friendly device. For satisfying these requirements, a generator based on the photocommutation principle has been realized. The photocommutation is possible thanks to photoconductive semiconductor switches, working in linear regime. That means the rise front of the electric pulse follows the optical one and the generated electric pulse is synchronized with the optical trigger. Moreover, such a generator results in a high reliability, depending on the laser source stability, and efficiency higher than 85% with a low amount of

optical energy (about 10 μJ for 4-kV bias voltage). Finally, it is a compact and adjustable pulser, suitable to be integrated in our system. The delivery device is a microchamber composed of two biocompatible electrodes, arranged to form a channel where the cells in suspension are injected. The main requirement for the delivery device is to match the pulse generator impedance in order to transfer the maximum of energy to the load, i.e. the biological medium.

3.4 M-CARS microspectroscopy set-up

The M-CARS laser source set-up is shown in Figure 3-19.

The pump source is the same that we use for the electrical generation. The laser beam is divided in two parts with adjustable energy by using a half-wave plate and a polarizer. The first beam (average power ~ 1.7 mW) is launched into a small-core (4.2 μm), 7-meter-long air-silica PCF for the generation of an incoherent SC Stokes wave, whereas the second one (average power ~ 36 mW) is divided again in two beams: the greatest part (~ 70%) is used as pump radiation of CARS system while the remaining fraction (~ 20%) is used as optical trigger of the electrical pulse generator, as said before.

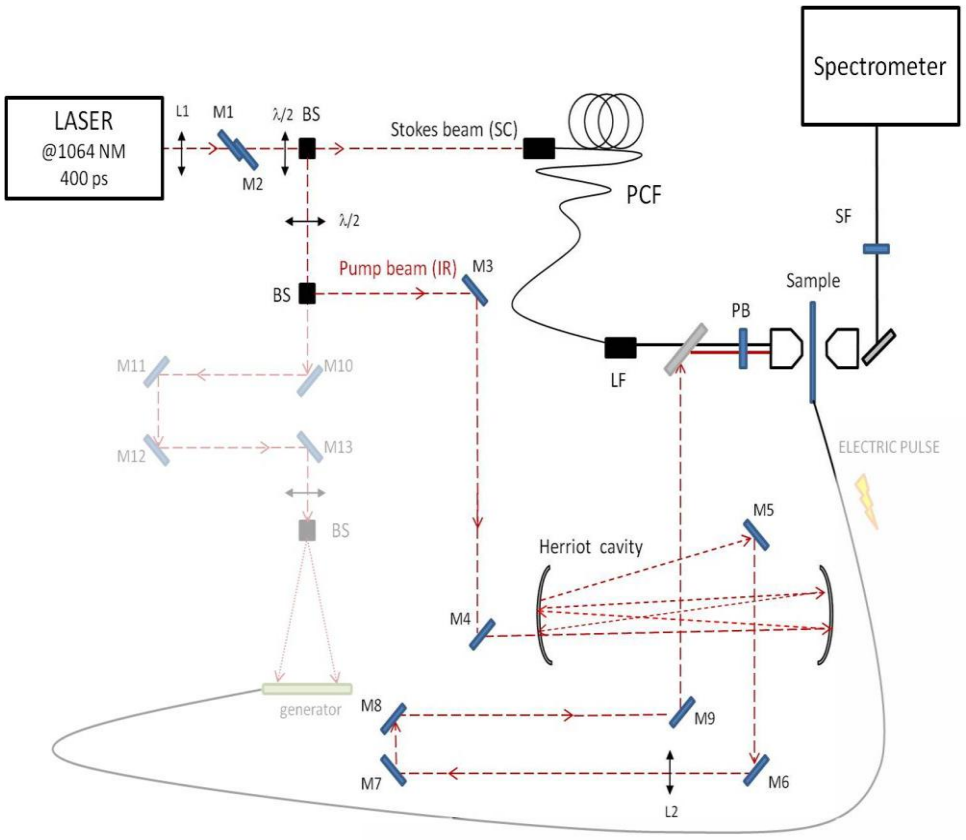

Figure 3-19: *Full electro-optical illumination system design. In evidence, the M-CARS setup. Legend: L, lens; M, mirrors; BS, beam splitter; SC, supercontinuum; IR, infrared; LF, long-pass filter; SF, short-pass filter.*

The core diameter of the PCF is 1.5 µm whereas the hole diameter and the hole-to-hole spacing are 1 µm and 2.3 µm, respectively (Figure 3-20 (a)). The zero-dispersion wavelength for the fundamental guided mode is closed to 990 nm (Figure 3-20 (b)). The fabrication technique of such a microstructured fiber is based on the stack-and-draw process and is described by Russell in [165] and in Appendix B. The dispersion curve (Figure 3-20 (b)) is calculated by a specific software, "COMSOL Multiphysics Simulation Software", of the COMSOL society. Starting from the geometric structure of the fiber, one can calculate the dispersion parameter, expressed in ps/nm/km versus the wavelength.

The strong third-order nonlinear effects occurring in the fiber create a broadband radiation, whose spectral region ranging from 1 µm to 1.7 µm is used as Stokes radiation of the CARS process.

The pump pathway is composed by an adjustable delay-line made by two concave mirrors to allow the synchronization with the SC Stokes beam after its propagation through the nonlinear fiber.

Pump and Stokes beams are spatially superimposed by means of a dichroïc plate before they reach the microscope stage. The two beams propagate to the microscope through a long-pass filter (LF in Figure 3-19). Finally, the CARS signal is recorded by a spectrometer through a short-pass filter (SF in Figure 3-19).

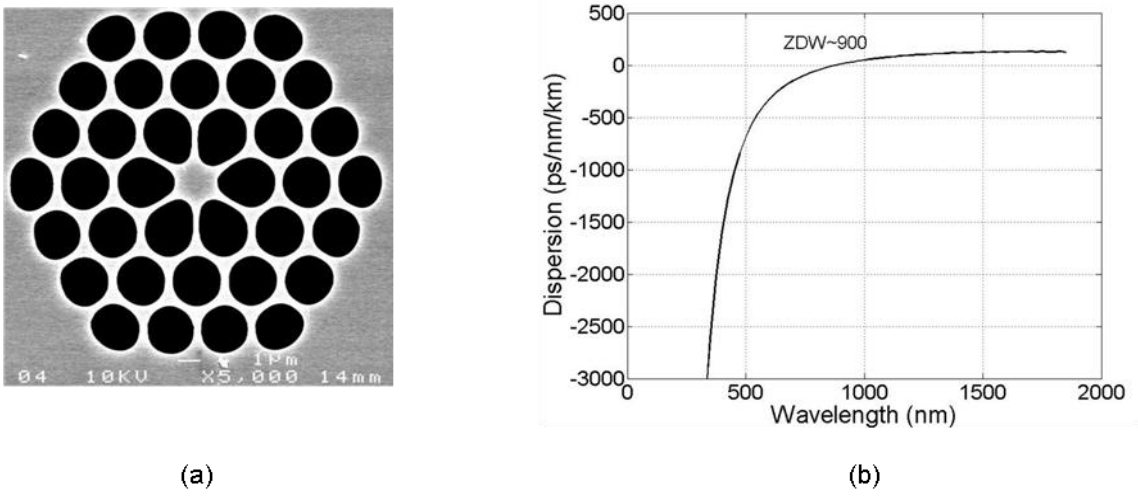

Figure 3-20: *(a) Dispersion curve of fiber fundamental guided mode of the PCF used in our experiment (ZDW ~ 900 nm), and (b) air holes distribution in the section of the PCF.*

Such a system must achieve three main purposes:

1) Providing a broadband Stokes wave for M-CARS process in infrared domain.

2) Permitting an easy synchronization between the optical beams and, more generally, between the optical beams and the electric stimulation.

3) Permitting to superpose and focalize the optical probe beams on the sample and synchronize them with the electric stimulation at the microscope stage.

In the following, each point will be fully discussed one by one.

3.4.1 Generated SC in the subnanosecond regime

When the 1064-nm optical beam is injected into the PCF, since the first centimetres of propagation, nanosecond optical pulses are mainly subjected to fiber nonlinearities, predominant in comparison to dispersive effects [179]. These effects lead to several modifications of the original temporal and spectral profiles.

For better understanding how SC is generated in sub-nanosecond regime, we report here the processes that are involved in it (for more details about each process the reader can refer to paragraph 2.6.3). We consider the Gaussian pulse in the inset 1 of Figure 3-22 that propagates through the PCF in the anomalous regime of the fiber. In the first centimeters of the fiber, the pulse experiences a spectral broadening due to the SPM. In this way, an initial unchirped optical pulse acquires a so-called chirp, i.e., a temporally varying instantaneous frequency (Figure 3-21).

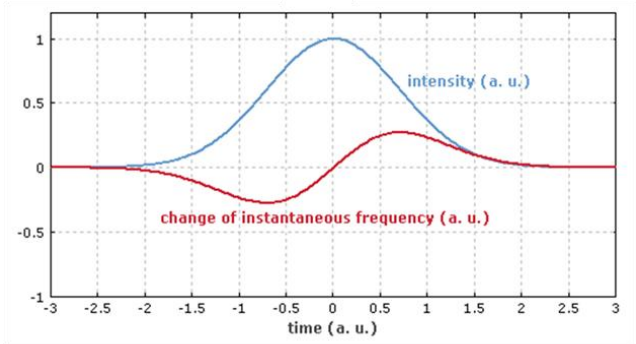

Figure 3-21: *(a) Instantaneous frequency of an initially unchirped pulse which has experienced SPM. (b) Characteristic oscillations of the power spectral density* induced by SPM.

This spectral broadening is accompanied by the linear effect of dispersion leading to temporal distortions of the initial pulse envelope. The combination of SPM and linear dispersion in anomalous domain gives birth to MI as we can see in inset 2 of Figure 3-22 [151]. The latter, due to the interplay between the SPM and the dispersion, leads to a break-up of the initial nanosecond pump pulse in a train of ultrashort pulses (femtosecond pulses) that may be considered as solitons. The periodicity of MI establishes the number and the rate of the solitons and the total energy of a MI period is confined into a single soliton. Because of the initial Gaussian distribution of the pump power solitons exhibit unequal peak power. In absence of perturbation the fundamental quasi-solitons forming the quasi-soliton train have the same group velocity, so they propagate in a quasi-coupled manner. Nevertheless, during propagation in the fiber the solitons are affected by high order dispersion effects, and by Raman phenomenon. Both effects act as a perturbation for the symmetry of the soliton train, breaking it in individual solitons. When the soliton spectrum is broad enough to overlap the Raman gain spectrum, the longer wavelengths experience the Raman amplification at the expenses of the shorter wavelengths. This effect, called self soliton frequency shift (SSFS), causes an overall spectral shift of the soliton towards IR region.

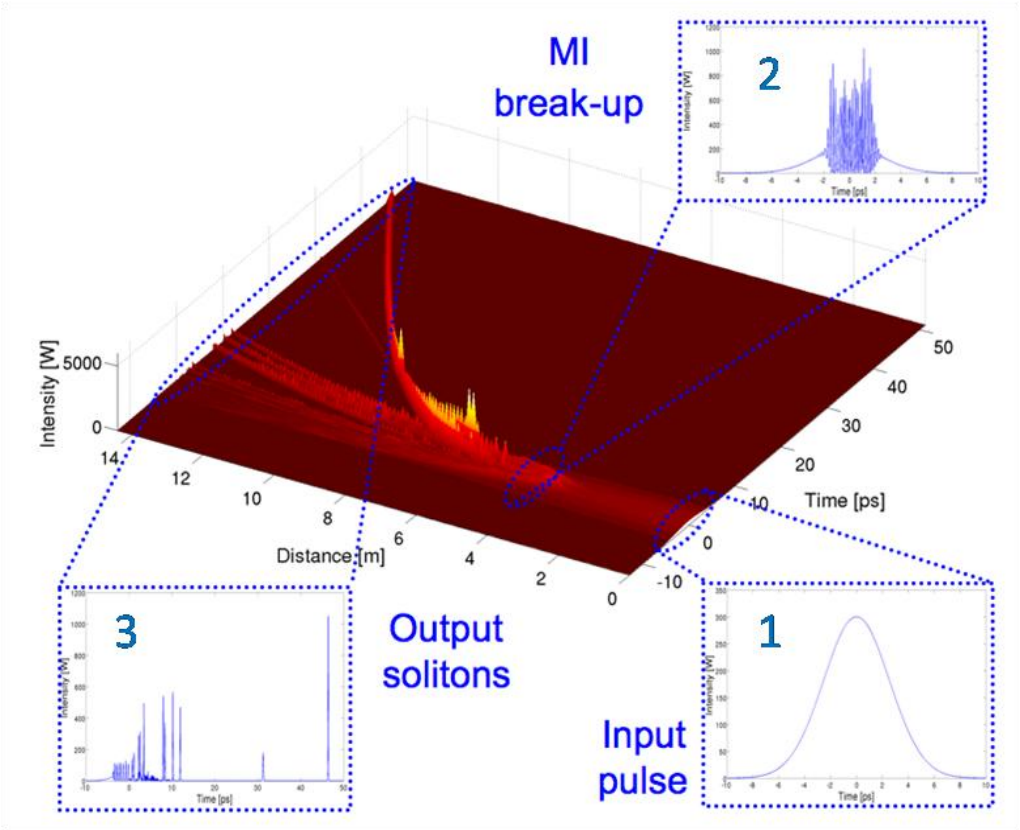

Figure 3-22: *Numerical temporal evolution of the input pulse as a function of propagation distance for the case where T_0 = 6 ps (shortest possible duration for simulation). Inset: temporal profile at different position along the fiber* **[179]**.

That SSFS phenomenon progressively creates a large bande spectrum spreading from the pump radiation at 1064 nm and up to 2 µm (Figure 3-23).

That spectral broadening is also enhanced by soliton collisions. Since the SSFS is proportional to the square of the soliton power, during the propagation the soliton initially generated in the central part of the input pulse downshifts faster than the other solitons. Additionally, because of the dispersion-induced slowing down, this central soliton may collide with other solitons of the train. During the collisions, the slower, lower-frequency central soliton acquires energy from a faster, higher-frequency soliton. As a result of all collisions, the most energetic solitons run away from the soliton train, contributing to generate a broad SC in the IR region (inset 3 in Figure 3-22).

In the normal dispersion regime (400-1000 nm) the build-up mechanism of the continuum is different that in IR domain. Because of the sign of the dispersion, no soliton generation is observed. The continuum is then driven by FWM process arising from interactions between the pump wave and the IR spectrum.

In our case, the SC obtained from the PCF at different input peak powers is showed in Figure 3-23. Because of MI represents an amplification of noise and not of the pulse itself, at the output end of the PCF, an incoherent infrared beam composed by a large number of ultrashort pulses is generated, as said before. It covers the region between 400 nm and 1700 nm at the highest input power (red curve Figure 3-23). For a fixed pulse duration (500 ps FWHM), we observe that the spectrum enlarges as the pump peak power is increased.

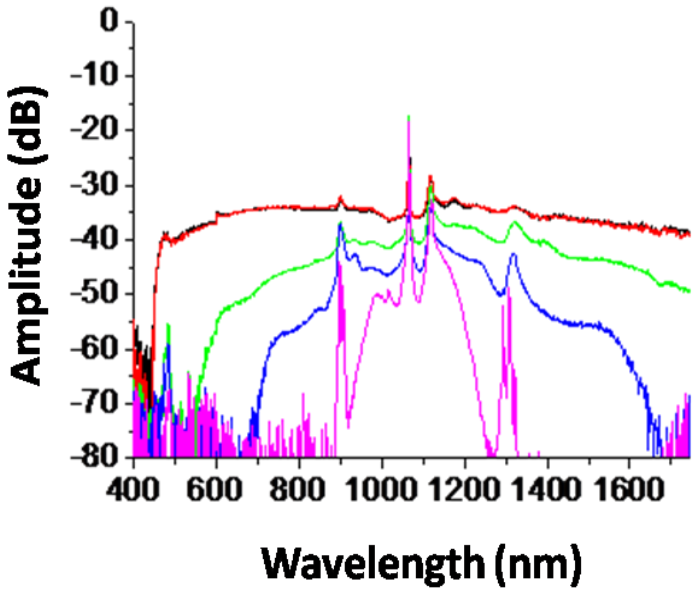

Figure 3-23: *Spectrum of the Stokes beam obtained by SC generation in the PCF.*

This result is expected, since SC generation is based on nonlinear effects depending on intensity variations of the propagating radiation; and it agrees with the numerical simulation reported in the PhD thesis of Marco Andreana [179]. The fiber nonlinearities permit to generate a flat enough SC spectrum between 600 nm and 1700 nm with a power decreasing of only 3 dB in the interesting band (1100-1700 nm) (red curve in Figure 3-23). Since for biological application we are interested in infrared wavelengths corresponding to the biological fingerprint region (1000 - 2000 cm^{-1}) (pump 1064 nm), our analysis is limited to the IR domain.

A more detailed analysis of the SC generation in PCF and of its impact on the original monochromatic beam is reported in the next chapter.

3.4.2 Beam synchronization and overlapping

Since CARS process needs a perfect temporal and spatial overlapping between the pump and Stokes waves to occur, after obtaining the broadband Stokes wave we verified the synchronization between the involved optical beams. As we can see in Figure 3-19, pump and Stokes beams run through two different pathways. The first beam propagates in air above a space of no more than 2 m, whereas the second one covers 7 meters of fiber. Consequently, in order to equalize the length of the two pathways, we need to introduce a time delay in the pump arm. Such time delay is provided by a Herriott cavity (Figure 3-19) and a simple series of four mirrors (M6-M9 in Figure 3-19).

First introduced by Herriott *et al.* [180], [181], a Herriott cavity is a particular type of multi-pass delay line forming a stable optical resonator. In its simplest configuration, it consists of two curved mirrors, separated by a distance L. A fixed insertion mirror (M4 inFigure 3-19) is placed off-axis near one of the mirrors, and a mobile mirror (M5 in Figure 3-19) is placed intracavity in order to extract the beam. When the Herriott cavity parameters are properly adjusted, the incident beam injected with the correct offset and tilt, undergoes multiple reflections, permitting a long path-length to be achieved in a small space. These multiple bounces forms a circular or an elliptical spot pattern on the mirror surface (Figure 3-24). Using appropriate design conditions, the beam size and energy remain constant, because the diffractive beam spreading effects are exactly cancelled as a result of the periodic focusing inside the cavity [182]. On the contrary, if the cavity is unstable, the beam diameter grows without limit. In order to avoid it, there is a stability criterion [180] that helps in choosing the useful parameters:

$$0 < \frac{d}{f} < 4 \quad \textbf{(34)}$$

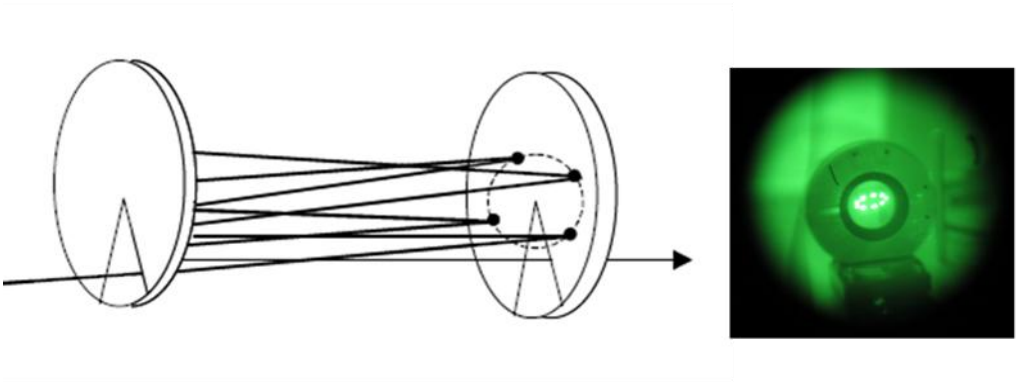

Figure 3-24: *(a) Sketch of the Herriott's cavity, forming by two concave mirrors. The multiple bounces of the beam between the mirrors marks an elliptical spot pattern on the mirror surface; in (b) is reported a picture of that pattern.*

In order to establish how many bounces the beam must do in the cavity and properly design the delay line, we have considered two factors: the distance covered by each beams and the speed at which the beams propagate in the different media (the air or the fiber). Knowing the time spent by Stokes beam to run through the fiber, we can estimate how long the delay line has to be for beam synchronization. We calculated the number of round trips the beam must do in the cavity, and then, we deduced the focal length f of the mirrors and the distance d between the mirrors (see Table 4 [180]).

Table 4. Different mirror focal length-distance ratios and the corresponding round trips for a beam propagating in the Herriott's cavity.

# round trip	2	3	4	6	12	24
f/d	0.5	1	1.7	3.7	14.7	58

Finally, we have verified the synchronization of pump and Stokes beams by using a 16-GHz oscilloscope (Figure 3-25).

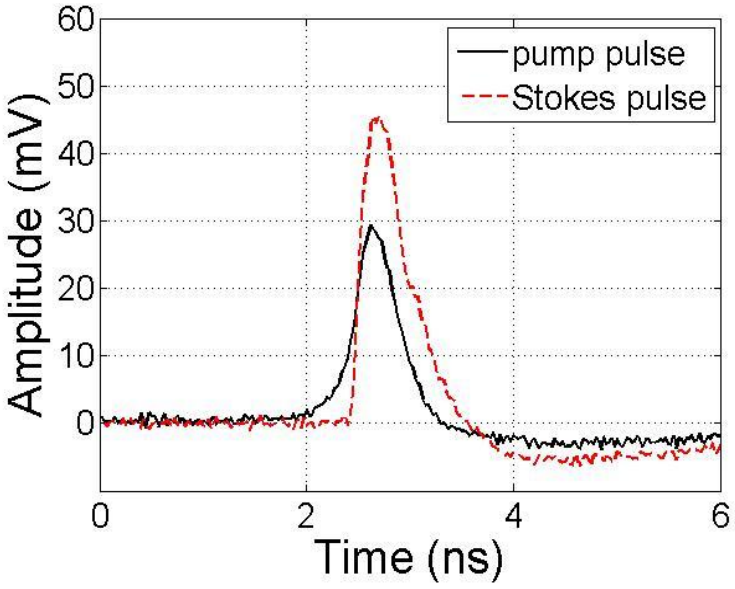

Figure 3-25: *Pump/Stokes pulse synchronization recorded through a photodiode and a fast oscilloscope.*

The second step is to verify the spatial overlapping of the beams, obtained with a dichroic mirror. The major difficulty is to perfectly focalize and superpose two beams of 4-µm diameter onto a small sample. The polychromatic Stokes beam passing through the objective lenses is subject to a strong chromatic aberration. Indeed, the glass used in microscope lenses exhibits different refractive indexes at different wavelengths of light. Light of shorter wavelengths, at the blue end of the spectrum, is focused nearer to the back of the objective than light of longer wavelengths. As a consequence, each wavelength of Stokes beam has a different focus plane, limiting its perfect focalization on the microscope slide (Figure 3-26). Some achromatic lenses permit chromatic compensation effect over two or three wavelengths, but no standard element is able to compensate chromatic aberrations over the entire spectrum (1000-1800 nm).

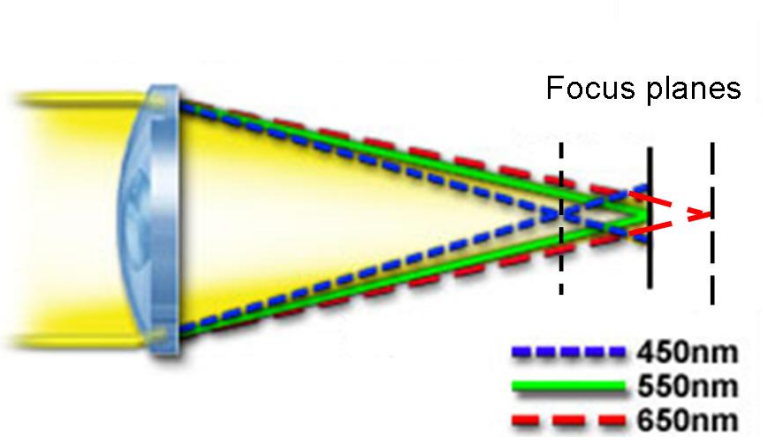

Figure 3-26: *Chromatic aberration in a lens, illustrating the existence of different focal planes for different wavelengths of light.*

In order to optimize the spatial and temporal overlapping of pump and Stokes beams, we have exposed a KDP crystal to the optical beams at the microscope stage (point where we focalize the radiations on the cell in bioelectromagnetic investigations). The two beams are focused onto KDP crystal with a 60X microscope objective (NA=0.7) and the radiation emitted by the crystal is collected with a 50X microscope objective (NA=0.85). The KDP crystal is cut for collinear Second Harmonic Generation (SHG) at 1064 nm, but can be used for Sum Frequency Generation (SFG) between radiations close to 1064 nm.

SFG obtained in crystals is a nonlinear optical parametric process using χ^2 susceptibility and mixing three waves instead of four waves when using χ^3 susceptibility.

The SFG process combines two low energy photons into a high energy photon: $1/\lambda_1 + 1/\lambda_2 = 1/\lambda_3$ .That nonlinear conversion phenomenon allows to perfectly synchronize the pump and Stokes waves by generating a new spectral component in visible domain. The optimization of that new wave generation guaranties a perfect temporal and spatial overlap between the two incident radiations (pump and Stokes waves). In our case, the involved wavelengths were 1064 nm (the pump) and 1118 nm (a spectral component of the Stokes beam) and 545 nm corresponding to the sum of the two precedent wavelengths. The maximization of the SFG process allows to properly adjust all the beam pathways in the microscope and to ensure spatial and temporal overlapping between the waves in order to induce CARS process. In Figure 3-27(a) we show the SFG due to the interaction between the pump beam at 1064 nm and wavelengths around 1118 nm provided by the broadband Stokes wave. In Figure 3-27(b) is reported SHG peak at 532 nm arising from the pump radiation only.

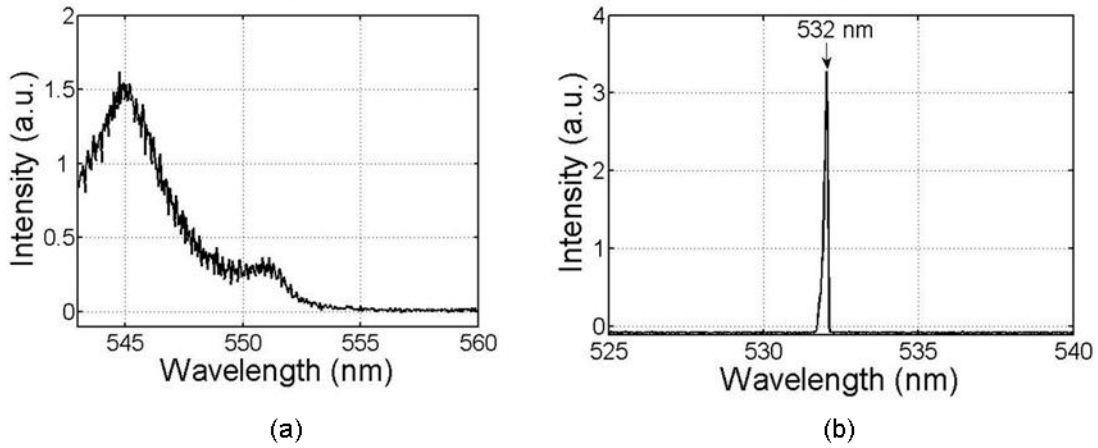

Figure 3-27: *(a) Peak at 545 nm generated by SFG process in a KDP crystal (λ_1=1064 nm and λ_2=1118 nm); (b) Peak at 532 nm generated by SHG process due at the interaction between the pump beam at 1064 nm and the KDP crystal.*

Finally, by using a fast oscilloscope, we are able to synchronize the delay between the electrical pulse excitation and the optical probe waves (CARS imaging system) (Figure 3-28).

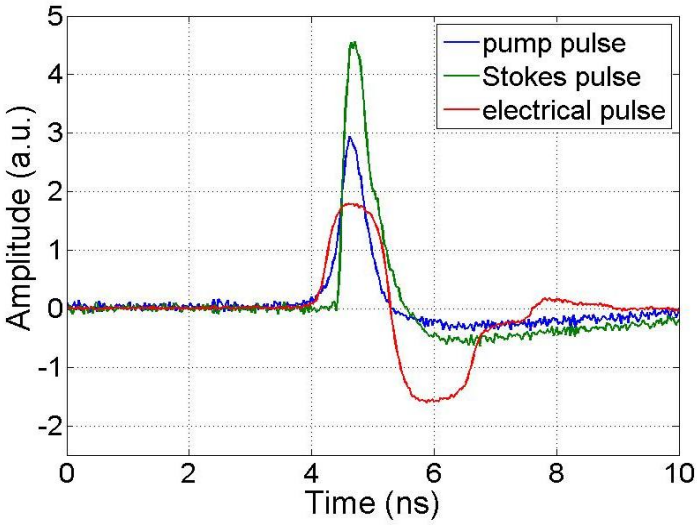

Figure 3-28: *Synchronization between the optical pulse and the unipolar (a) and bipolar (b) electrical pulse.*

3.5 Conclusions

In this chapter, the electro-optical pump-probe system for cell electroperturbation and detection, main subject of this PhD thesis, has been introduced, described and commented in detail. The system consists of an electrical pump that serves for stimulating and manipulating the biological cell, and of an optical probe for imaging the cell and detecting the PEF bioeffects.

In order to conceive a performing and compact system, satisfying the requirements both of the electrical and the optical applications, a component that matches the two scientific areas has been necessary. Such a component is represented by a common sub-nanosecond laser source. That laser provides: 1) the trigger beam for the photocommutation process leading to the electric pulse generation, and 2) the pump and Stokes beam for the CARS imaging system.

The photocommutation-based generator is a robust, flexible and repeatable device. The key-characteristic consists of using photoconductive semiconductor switches working in linear regime, permitting to easily adjust the shape, the duration and the amplitude of the generated pulses according to the application. The generator is matched to an exposure microchamber where the electric pulses are delivered to the cells, on the stage of a microscope. The microchamber is designed to deliver the maximum of the energy to the sample by mains of two biocompatible electrodes in a broadband frequency configuration.

The M-CARS source provides a monochromatic pump beam from the fundamental laser and a polychromatic Stokes beam by the passage of the fundamental beam through a PCF. Next, the pump and Stokes beams are superposed on the sample at the microscope stage and synchronized with the electric pulses.

While such an exposure system has already been presented in previous works [17–20], [74], [172], as well as several solutions providing SC sources for M-CARS microscopy [130], [131], [140], a complete system that combines the two technologies is introduced here for the first time. The use of M-CARS imaging may represent a valid improvement in the electroporation research area, leading to know the physical mechanisms beyond the bioeffects already observed by means of other techniques, such as fluorescence microscopy. The major improvements of M-CARS microspectroscopy deal with the following advantages: a non invasive and non toxic detection; high sensitivity and high spectral resolution provided by the nonlinear dependence of the CARS signal on the excitation intensity, and by the use of narrower-band pump pulses, respectively. On the other hand, concerning the acquisition time, we think that it is possible to perform a faster imaging system producing powerful subnanosecond puloses at repetition rate higher than tens of kilohertz still synchronized with the electrical device. An optoelectronic generator with kilohertz generation has been already demonstrated and published in 2008 [71]. In that context, a high repetition rate M-CARS system, suitable to be synchronized with the electric device, has to be demonstrated.

In Chapter 4, a detailed characterization of high repetition rate SC sources, developed from microchip laser source, is presented.

Chapter 4- High repetition rate M-CARS sub-nanosecond laser sources: a temporal and spectral analysis

Since 2007 Okuno *et al.* [130–132] have collaborated with our research group of Xlim, in designing a M-CARS laser source in sub-nanosecond regime, showing the possibility to use such a SC source laser in performing M-CARS measurements. In 2007, the group of Xlim laboratory has developed an ultraboadband laser source for CARS spectroscopy using the SC generated from a PCF by seeding both 532 and 1064 nm sub-nanosecond pulses. In a second time, that laser source has been used by Okuno's group, demonstrating M-CARS measurements of several molecular liquid (benzene, toluene, and pyridine) with a spectral resolution of about 3 cm^{-1}, in the spectral range of > 2000 cm^{-1} [130]. The authors highlighted that a detection time reduction by a factor of > 100 may be significantly obtained by optimizing the pulse energy and the repetition rate of laser source. In a second study [131], [132], they have extended their investigations to the deep near-infrared (NIR) region in order to apply such system to CARS imaging of living cells. That NIR CARS excitation is more suitable for biological analysis, minimizing photodamage and penetrating deeper into the tissue. In these first examples the M-CARS laser source had a repetition rate of 6.6 kHz and in a further study the repetition rate is increased to 33 kHz [140]. The increase of the repetition rate of the seeding optical pulse improves the acquisition time of the imaging system, permitting to obtain images in few milliseconds. In the latter study [140], some multi-colour images of *C.elegans* in both C-H stretching and fingerprint regions (Figure 4-1) have been obtained using this 33-kHz, sub-nanosecond source, demonstrating its applicability to M-CARS microspectroscopy.

We remind that such kind of sub-nanosecond ultracompact system offers several advantages, like a high spectral resolution (< 0.1 cm^{-1} [140]) because of its Fourier transform sub-nanosecond pump pulse and simultaneous probing of a large variety of chemical bonds thanks to a good time synchronization of all the wavelengths propagating in the Stokes wave [132]. Moreover, a lower sensitivity to the group-delay dispersion permits to obtain CARS signals without changing the delay-time between the pump and Stokes pulses. Therefore, the recording of multicolour images by CARS becomes easier and faster (order of ms thanks to repetition rate

up to 100 kHz) [131], [132], [140]. Nevertheless, the residual spectro-temporal spreading out of the Stokes wave in nanosecond regime during the spectral broadening in fibers is more complex than in femtosecond domain [104]. Indeed, the larger the input pulse duration is, the higher the temporal decoherence is. Furthermore, the numerical solving of nonlinear Schrodinger equation, usually used in the simulations, for nanosecond pulses becomes difficult (high number of samples, high computation time). As we have seen in the previous sections, the mixing of several nonlinear effects gives birth to large temporal instabilities with the build-up of solitons and rogue solitons propagating in presence of large Raman perturbation which drastically distorts the input signal envelop. As a matter of fact, the investigations performed with this innovative laser source have highlighted that the use of a polychromatic Stokes beam instead of a monochromatic one introduces some technical difficulties in pump-Stokes temporal synchronization and spatial superimposition because of these temporal distortions undergone by the Stokes pulses during propagation in the PCF.

In this context, I contributed in understanding the reasons and the impact of these temporal distortions, carrying out a detailed study of phenomena occurring in time and in spectral domain. This new laser source has been the object of a patent [183].

In this chapter we present another sub-nanosecond M-CARS source on the base of that mentioned above. Here, the decrease of optical pulse peak power, due to a higher repetition rate of 75 kHz, is compensate by adding an optical fiber amplifier (Ytterbium-doped fiber amplifier, YDFA) before PCF (Figure 4-2(a)). Unfortunately, this new setup introduces some difficulties associated with the nonlinearity effect occurring in the fiber of amplifier. In order to understand the impact of YDFA on SC generation and on the pump/Stokes synchronization, we report a detailed analysis of the spectral broadening induced by a PCF and the impact of PCF characteristics on temporal Stokes pulse profiles. Such a temporal study is performed for the first time to the best of our knowledge.

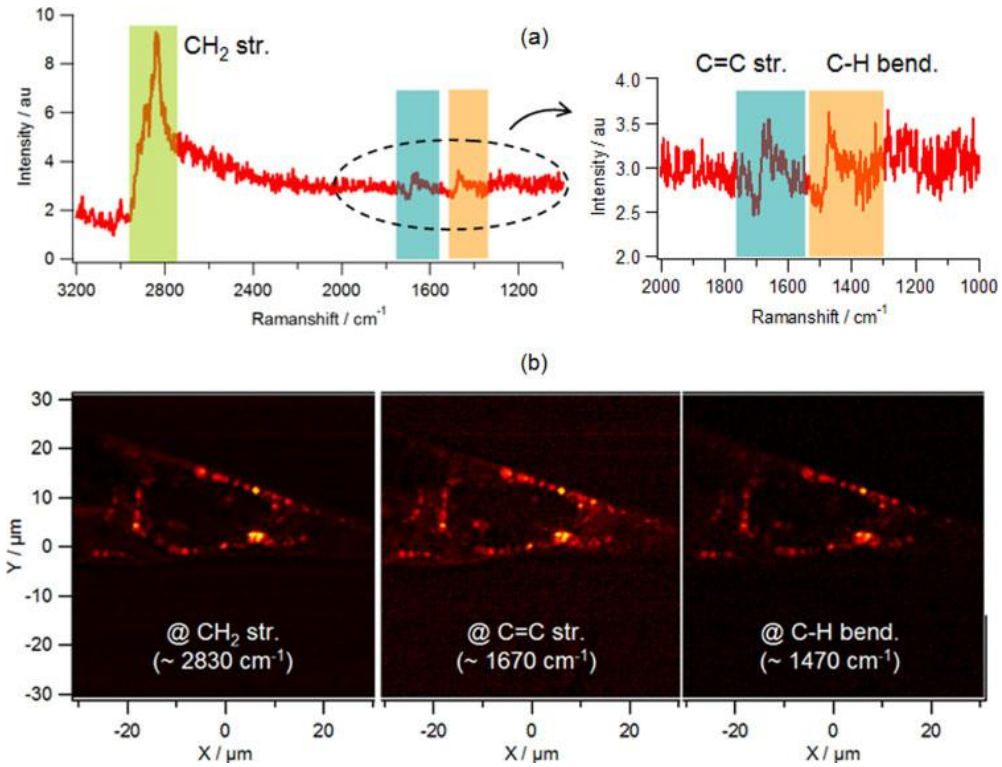

Figure 4-1: *Spectral profile of M-CARS signal (a) and multi-color imaging of C.elegans in both CH_2 stretching and fingerprint regions (b)* **[140]**.

4.1 Laser source design and parameters

The design of the dual-output compact laser source presented here is shown in Figure 4-2(a). The pump source is a longitudinally single-mode passively Q-switched microchip laser, delivering sub-nanosecond (950 ps, FWHM) pulses at 1064 nm with a repetition rate of 75 kHz (Figure 4-3(a)). More precisely, the Q-switching technology permits to generate a pulsed output beam with high peak power (> 20 kW), repetition rate from a few Hz to hundreds of kHz and longer pulse durations compared to mode-locking laser. The Q-switch is a variable attenuator of the optical resonator Q-factor and can work in a passive or an active way (externally controlled). In our case (passive Q-switching), the Q-switch is a CR4+:YAG saturable absorber, a material whose transmission increases when the energy of light exceeds some threshold [184]. The beam issued from the microchip laser is divided in two parts whose ratio of energy is adjusted by using a half wave plate and a polarizer. This energy control permits a real-time optimization of the CARS signals and allows adapting the pump and Stokes power to each studied sample.

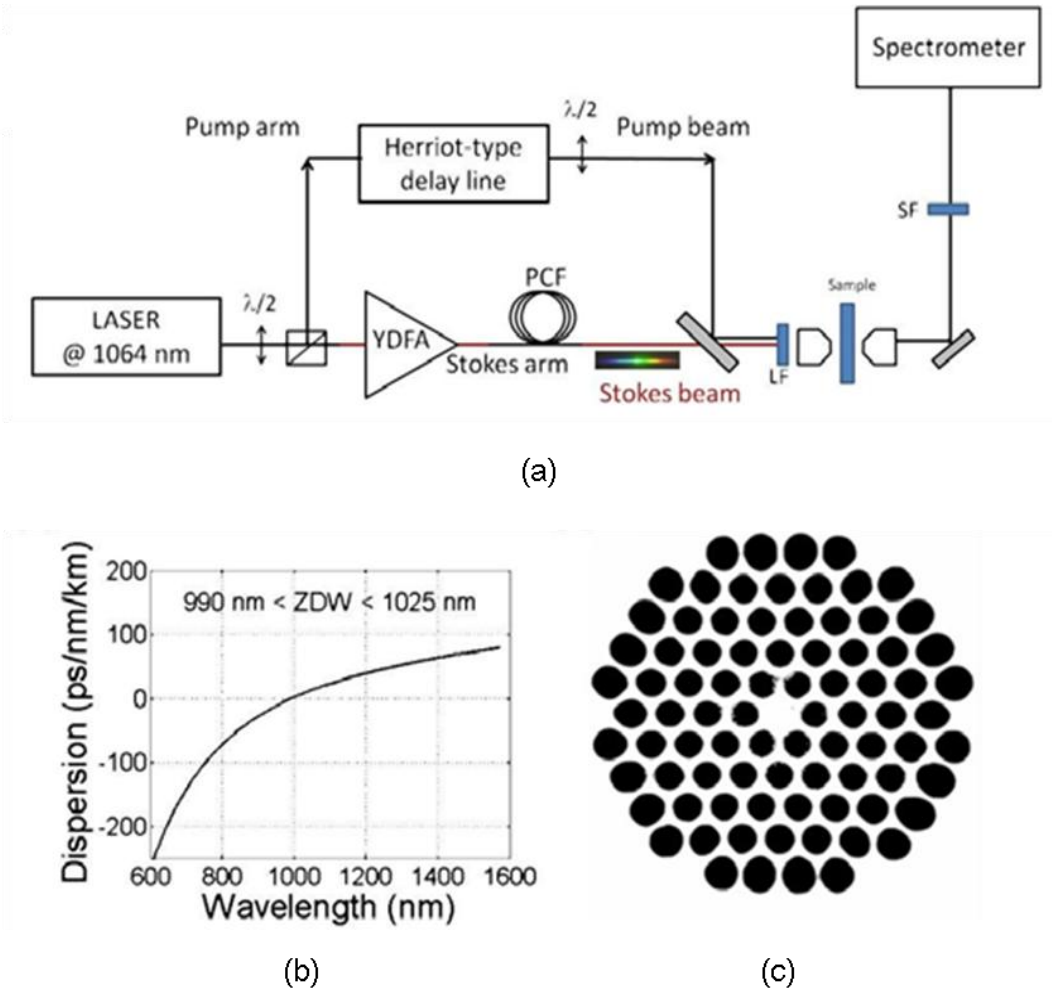

Figure 4-2: *(a) Schematic representation of the dual-output light source designed for M-CARS microspectroscopy applications; (b) dispersion curve of fiber fundamental guided mode of the PCF used in our experiment (ZDW ~1000 nm), and (c) air holes distribution in the section of the PCF.*

One part of the energy is directly used for the pump wave (average power ~ 200 mW, peak power ~ 2.7 kW) of the CARS process after the passage through a Herriot-type delay-line for synchronizing the pump and the Stokes pulses. After the delay-line a half wave plate is placed to select the polarization of the pump beam sent to the sample.

Because of the high repetition rate of the microchip laser (75 kHz), the peak power lunched in the nonlinear fiber (only 270 W) is not high enough to obtain large spectral broadening in the PCF. Then, in order to regenerate the amplitude of the excitation pulses necessary to SC generation we need to amplify the optical pulses before launching into the PCF.

We placed an ytterbium-doped fiber amplifier (YDFA) just before the PCF in our system (Figure 4-2(a)). The YDFA is constituted by a 6-m-long double-clad fiber exhibiting a single transverse mode at 1064 nm and with a ZDW at 1.3 μm. The available average power at the amplifier output is 900 mW which represents more than 12.5 kW of peak power. In Table 5 the pump and Stokes beams parameters are reported.

The nonlinear spectral enlargement is realized by the passage in a 7-m-long air-silica PCF slightly different from the PCF used in the M-CARS source of the system presented in the previous chapter (Figure 3-20). A part of the continuum beam at the PCF output (from 1 μm to 2.4 μm) constitutes the Stokes radiation of the CARS process. Monochromatic (pump) and polychromatic (Stokes) beams are spatially superimposed by means of a dichroïc plate before sending to a microscope. The two beams are sent to the microscope through a long-pass filter (LF in Figure 4-2(a)) to optically excite the sample in the IR range that allows a deeper penetration and to avoid photodamage to the biological sample. The two beams are collimated and focalized on the sample by the microscope condenser lens. Next, the beam transmitted by the sample is collected by the objective lens of the microscope and sent at the detection system, composed of a spectrometer and a CCD detector.

In order to reject the pump and Stokes beams and collect only the CARS signals, they pass through a short-pass filter (SF in Figure 4-2(a)) before going to the spectrometer input gate.

Table 5. Laser source output parameters of the pump and Stokes beams.

	Average Power [mW]	Peak Power [kW]	Pulse Duration [ns]	Repetition Rate [kHz]
PUMP BEAM	200	2.8	0.95	75
STOKES BEAM	0-800	10.1	0.95	75

In the following section the fiber amplifier effects on the optical pulses of the SC wave in time and spectral domain will be discussed.

4.2 Impact of YDFA on SC generation

The temporal and spectral profiles of the beam pulse produced by the microchip laser are shown in Figure 4-3 (pulse width of 950 ps, spectrum width of ~ 2 pm). After propagation in the YDFA a powerful beam (900 mW) exhibiting minor spectral and temporal distortions is obtained. During propagation in the YDFA, Raman conversion partially depletes the central part of the pulse and produces a frequency conversion towards infrared domain close to 1118 nm (Figure 4-3(c) and (d)). The Raman conversion efficiency is estimated to 10% of the initial energy but is sufficiently high to induce some modifications of the temporal shape with the occurrence of a depletion in the central part of the nanosecond pulse at 1064 nm. That modification of the time profile is recorded by using a fast oscilloscope and a band-pass filter at 1064 nm.

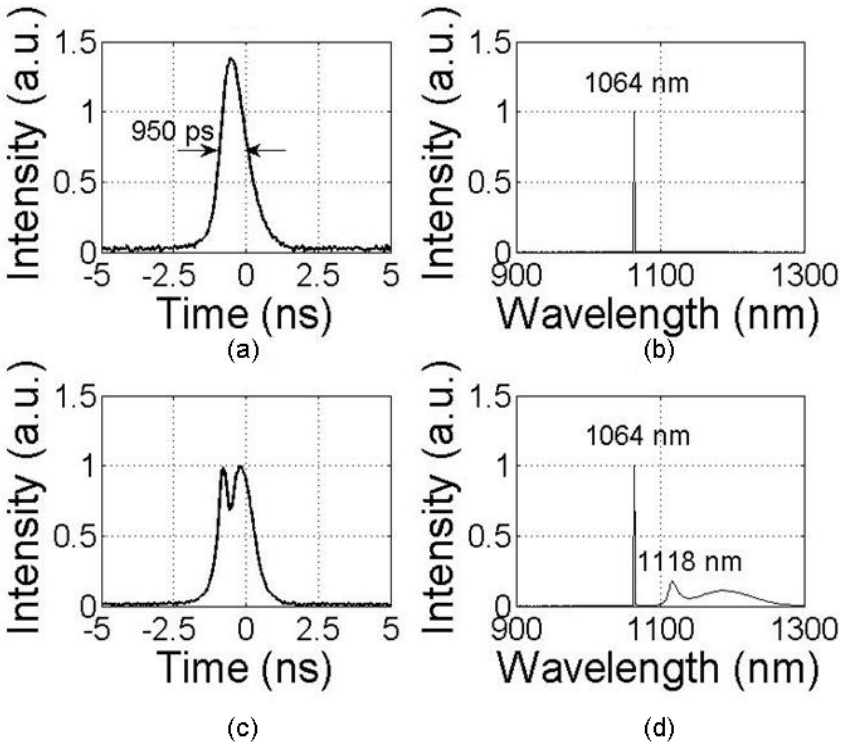

Figure 4-3: *Pulse and spectrum profiles at the PCF input (a) and (b) without amplification in the YDFA, and (c) and (d) with amplification in the YDFA, normalized to the correspondent incident peak power (2.8 kW and 10.1 kW, respectively).*

Without filtering, in fact, no temporal distortion of the pulse shape is observed and we only observe the spectral content modification.

As we said in Chapter 3, the interplay between self-phase modulation and dispersion yields in the early stage of propagation in the PCF to a self-induced instability, referred to as modulation instability. The spectral broadening towards infrared wavelengths is subsequently driven by Raman soliton self-frequency shift enhanced by compression throughout soliton collisions in the presence of Raman gain. At output end of the PCF an incoherent infrared beam constituted by a large number of ultrashort pulses is generated. The spectrum is particularly flat with an overall amplitude difference lower than 5 dB over the entire infrared domain between 1 μm and 2.2 μm (Figure 4-4). This spectral profile is recorded by means of an optical spectrum analyzer in a large averaging mode (>10).

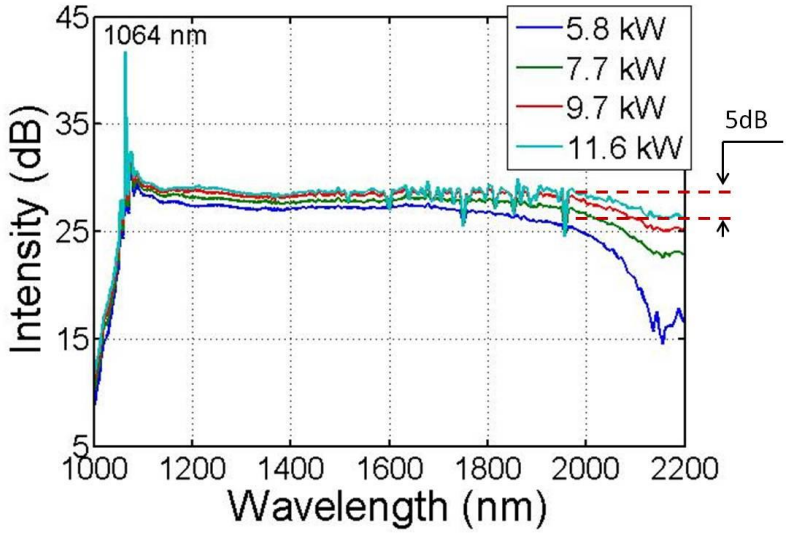

Figure 4-4: *Spectral broadening (SC) of the Stokes beam by nonlinear propagation in the PCF for four different values of the amplifier peak power*.

At this stage, no information is obtained on the temporal distribution of the continuum energy that is however of major importance for multiplex-CARS applications. In order to overcome this drawback, we have performed an exhaustive study of the Stokes beam spectral content in the time domain. The method and the results of this analysis are discussed in the next section.

4.3 Time-frequency resolved analysis of the generated SC

First, the set-up used for the spectral and temporal measurement recording is described. Next, the results are discussed and a comprehensive interpretation of the occurring phenomena is done.

4.3.1 Recording set-up

The purpose is to record the temporal profiles of the Stokes pulses for each wavelength constituting the SC beam issued from the PCF. The recording set-up is shown in Figure 4-6. The laser source and the PCF are those described in section 4.1. The monochromatic laser beam is divided in two parts by the beam splitter, BS, in Figure 4-5. The one directly goes to the gate 1 of the 16-GHz oscilloscope and serves as a reference for the interesting pulses during the visualization on the oscilloscope monitor. The other part passes through the fiber and the output is sent to a diffraction grating in order to separate each spectral component of the polychromatic beam. Next, we select one wavelength at a time by means of a pinhole. The corresponding pulse is recorded then both by the oscilloscope (gate 2) and by the spectral analyser. The temporal and

spectral resolutions are 20 ps and 30 nm, respectively. Finally, the recorded data are processed to obtain the spectrogram of Figure 4-6(a).

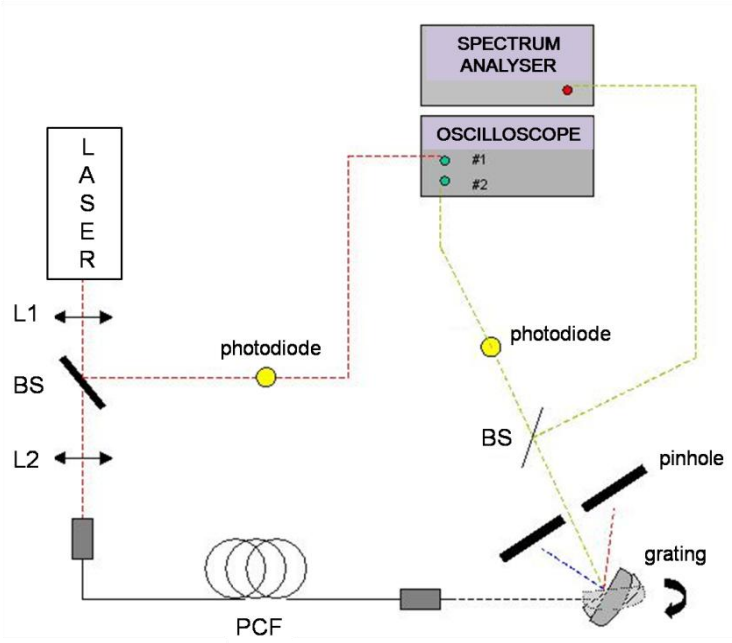

Figure 4-5: *Set-up for recording the Stokes pulse temporal profiles at different wavelengths.*

4.3.2 An original approach for the spectral broadening analysis

Figure 4-6(a) shows the energy distribution of the Stokes wave versus wavelengths, and in (b) we report some Stokes pulse time profiles at different wavelengths. As we can see, the central part of the pump pulse at 1064 nm is fully depleted at the output of the PCF. In order to understand what happens, we need to refer to the different mechanisms affecting the propagation in PCF (section 3.4.1). In the current set-up, the fundamental beam (constituting by Gaussian pulses) passes through the YDFA fiber before going into the PCF. The Stimulated Raman scattering is the dominant effect during propagation in the first fiber (YDFA), and transfers all the energy contained in the central part of the pump pulse towards infrared wavelengths. Pulse tails instead remain largely undepleted, being their instantaneous power below the Raman threshold. Hence, the output profile of the pump pulse is dramatically transformed from a 950-ps almost Gaussian shape into two shorter pulses formed by the remaining tails and separated in time by more than 2 ns (Figure 4-6(b) at 1065 nm).

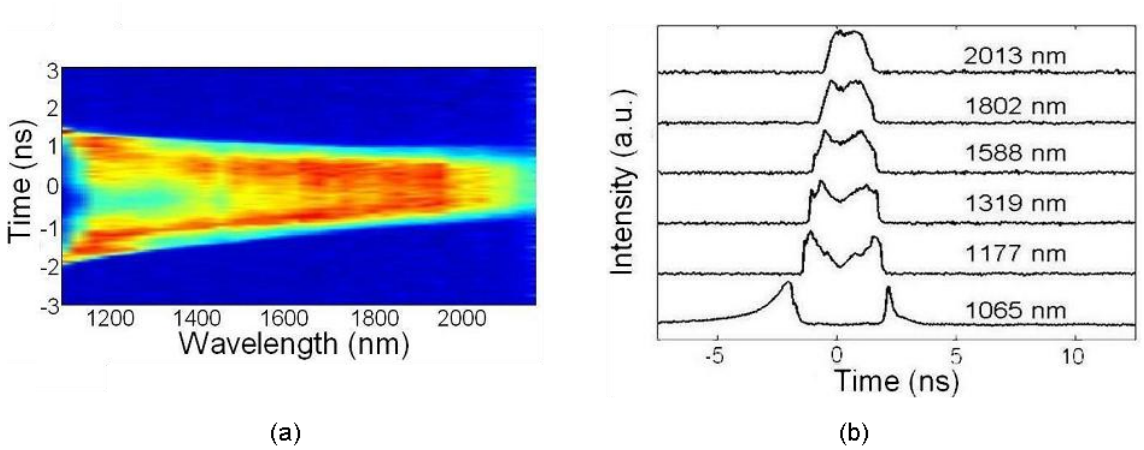

Figure 4-6: *(a) and (b) Spectro-temporal evolution of the Stokes wave recorded at the output end of the YDFA+PCF; (a) 2-D representation; (b) 3-D representation.*

Similar distortions can be observed in Figure 4-6(b) for wavelengths longer than 1064 nm: even there we find again the same power depletion in the central part of the pulse. Such depletion gradually tends to disappear for wavelengths longer than 1800 nm. This Raman-induced depletion acts as a pulse reshaping effect for infrared wavelengths. It is worth noting that those tails which are not affected by Raman gain, are instead influenced by MI, solitonic propagation and SSFS. Then a continuous spectrum on each pulse sides is obtained for wavelengths between 1.1 μm and 2.2 μm.

At this stage, we would like to emphasize an important point. In practice, when a quasi-CW or nanosecond pulse propagates in the anomalous dispersion regime, it is rather unusual that the Raman effect dominates since the early stage of propagation. As we have mentioned in the previous chapter, MI usually occurs first whereas Raman scattering generally takes place much later during propagation and essentially manifests itself via the SSFS. The different behaviour that we observe here can be easily understood by noticing that the Raman-induced Stokes generation is initiated earlier when propagating in the YDFA. Because of strong amplification, the central part of the 1064 nm pulse propagating in normal dispersive regime in the YDFA (ZDW~1300 nm) eventually exceeds the Raman threshold and therefore experiences the Raman effect. This results in initiating the depletion of the central part of the pulse to form the first Stokes peak at 1118 nm (Figure 4-3(d)).The coupling of these two radiations in the PCF (pump and first Raman Stokes radiations) acts as an optical seeding that decreases the Raman threshold. Therefore, Raman effect occurs first in the PCF and is responsible for the strong depletion of the initial pulse. The onset phase of MI generally observed in the very first stage of propagation in the anomalous dispersion regime arises later and is clearly visible for wavelengths above 1500 nm. In contrast, because of their low power level, pulse tails are not affected by the Raman gain but rather by MI, by soliton collisions and by SSFS. A continuum is

then formed. Hence, because of the initial pump conditions set at the input of the PCF, the threshold of Raman effect is probably lower than that of MI and therefore primarily affects the pulse spectrum.

Whereas Raman gain is the dominant effect in the early stage of propagation, both nonlinear effects (Raman and MI) subsequently contribute to the spectral broadening and remain in competition throughout propagation. Indeed, after few meters of propagation, MI progressively enters into play and ultimately breaks up the pulse structure into solitons. The MI signature is clearly visible for wavelengths longer than 1.55 μm. At this stage, soliton propagation and SSFS dominate as the Raman scattering essentially manifests itself via the SSFS and not via the Stokes generation. The output pulse envelope obtained for wavelengths above 1600 nm, exhibits square shape and it is likely composed by several kind of waveforms including femtosecond pulses. The envelope durations at these wavelengths are much larger than that of the initial pump pulse at 1064 nm and progressively decrease as the wavelengths increase. This temporal evolution is induced by the initial Gaussian pulse profile where the conversion toward longer wavelengths is produced by the most powerful part of the pulse.

In order to verify further our hypothesis regarding the competing role of stimulated Raman scattering and MI, we experimentally achieved the same spectral broadening under different input conditions. In this new experiment, a sub-nanosecond Fourier transform pulse at 1064 nm was directly launched in the PCF.

In Figure 4-7 is shown the spectrogram and a collection of temporal pulse profiles as well as in the previous case. Now, the first nonlinear effect occurring during the propagation is MI followed by soliton dynamics. Hence, the initial pulse envelope of the initial pulse is periodically modulated and ultimately transformed into a periodic train of solitons which later colliding and exchanging energy throughout propagation.

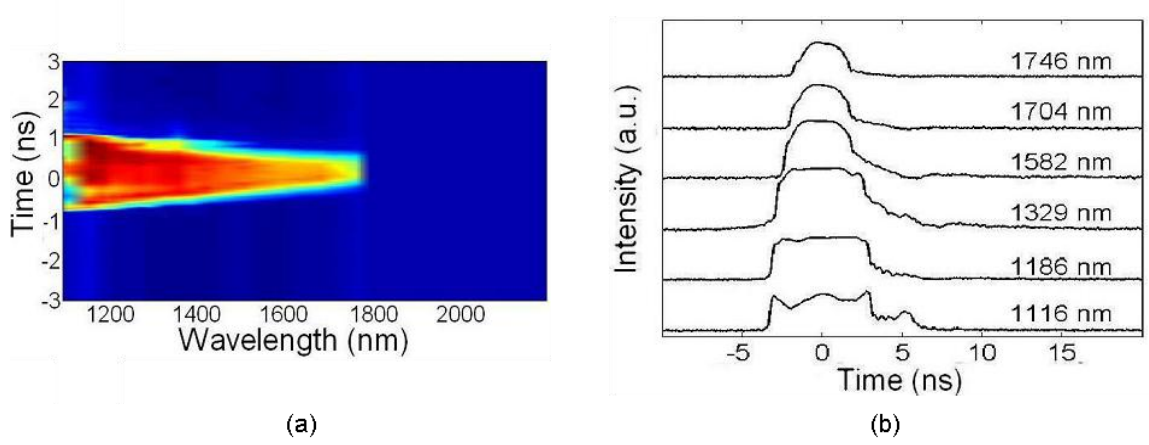

Figure 4-7: *(a) and (b) Spectro-temporal evolution of the Stokes wave recorded at the output end of the PCF only; a) 2-D representation; b) 3-D representation.*

Lower depletion of the pulse center is obtained with respect to the previous case, confirming the fact that the YDFA has a strong impact in inducing temporal distortion on Stokes pulses.

We discuss now the role of dispersion on the beam spectral broadening. Due to the short fiber length (7 m) used in the experiment, a weak influence of the group velocity difference is observed on the spectro-temporal profile (Figure 4-6(b)). The infrared pulses propagate slower than the other ones in the anomalous dispersion regime, and are progressively delayed all along the propagation in the fiber.

The maximum delay obtained at the output end of the fiber is estimated to 254 ps (Figure 4-8, square dots). By this way the leading edges of all the pulses at each wavelength are quasi synchronized (Figure 4-9(b)). The maximum pulse broadening observed on the spectro-temporal representation is obtained for wavelengths close to the pump and reaches 3 ns (FWHM). The minimum pulse duration is obtained for infrared pulses above 2 μm and reaches 1.3 ns (Figure 4-8).

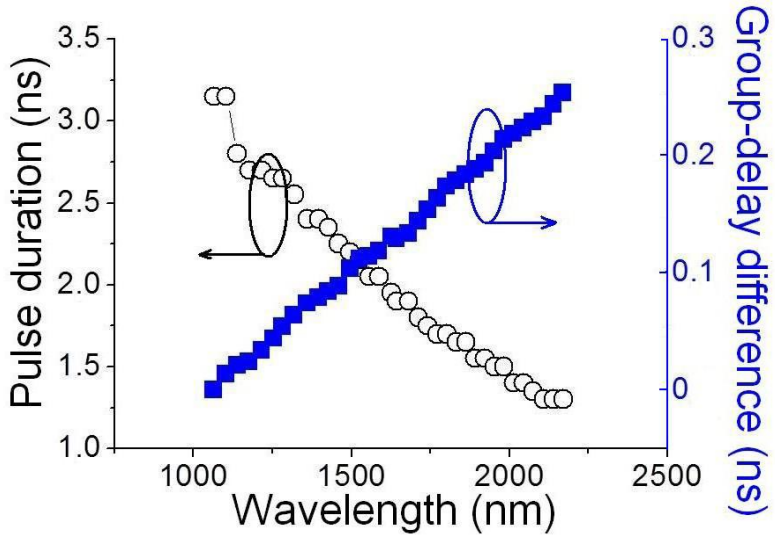

Figure 4-8: *Stokes pulses duration (circle dots) and group-delay difference (square dots) trends versus wavelength.*

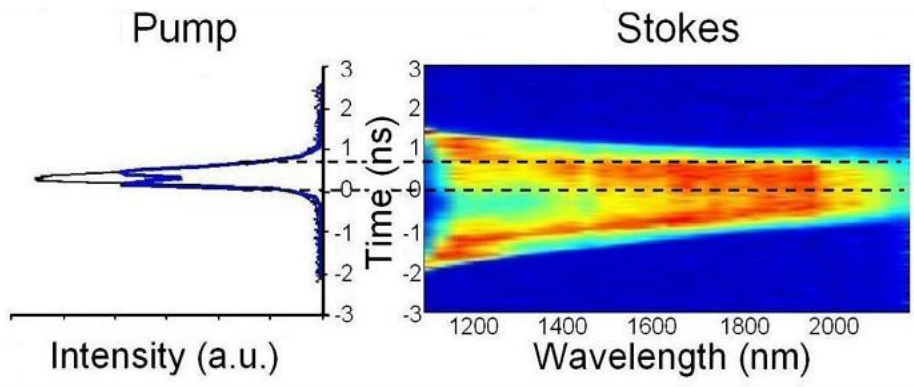

Figure 4-9: *Superimposition between the distorted (blue line) and the Gaussian (black line) pump pulse (a), and Stokes pulses (b).*

4.3.3 Numerical analysis of the propagation phenomena in the optical fibers

In order to have a theoretical explication of the experimentally observed wave broadening phenomena during its propagation through the fiber, we have also performed a numerical simulation. Similar numerical studies have been already made and reported in the PhD thesis of Marco Andreana [105] in the case of femtosecond and picosecond pulses. Here, we are interested in studying the phenomena concerning the nanosecond pulses where unfortunately numerical simulations are more time consuming. For this reason we simulated pulse durations much shorter than the ones used in the experiment.

Before discussing the method and the results of the simulation, let us introduce first some basic of pulse propagation in fibers.

An appropriate model for describing the wave propagation in a dielectric medium, like the optical fiber, is given by the solution of the Generalized Nonlinear Schrödinger Equation (GNLSE) [151]. The GNLSE is an extended version of the Nonlinear Schrodinger Equation, assuming a slowly varying envelope. The GNLSE reads as:

$$\frac{\partial E(z,t)}{\partial z} - \sum_{n\geq 2} \beta_n \frac{i^{n+1}}{n!} \frac{\partial^n E(z,t)}{\partial t^n} + \frac{\alpha}{2} E(z,t) = i\gamma \left(1 + \frac{i}{\omega_0}\frac{\partial}{\partial t}\right) \left(E(z,t) \int_0^{+\infty} R(\tau) \left|E(z,t-\tau)\right|^2 \partial\tau \right) \quad \textbf{(35)}$$

Beyond its complex aspect, is important to highlight that this partial differential equation takes into account: the different order dispersions through β (second term of the left-hand member of the equation), the fiber losses with α (third term of the left-hand member), and, the nonlinear response of the medium in the right-hand member of the equation represented by the nonlinear fiber coefficient γ (defined in Chapter 2) and included in:

$$R(t) = (1 - f_R)\delta(t) + f_R h_R(t) \quad \textbf{(36)}$$

where $\delta(t)$ is the Dirac function and $h_R(t)$ is the Raman response function. The function R(t) therefore includes the nonlinear contribution of electronic origin through the term $(1-f_R)$ which acts as an instantaneous nonlinear potential (here it comes its name as it looks like a Schrödinger equation for a nonlinear potential), and the delayed nonlinear response coming from molecular vibrations through the coefficient f_R = 0.18 (in silica fibers these vibrations are connected to the Raman effect, and this is why the NLSE is called Generalized). Details on the numerical methods to solve the GNLSE can be found in [185], [186].

It is also useful to introduce two length scales, known as the dispersion length L_D and the nonlinear length L_{NL} [151].

$$L_D = \frac{T_0^2}{|\beta_2|} \qquad L_{NL} = \frac{1}{\gamma P_0} \quad \textbf{(37)}$$

where T_0 and P_0 are the input pulse width and the peak power of the incident pulse, respectively. These two lengths, L_D and L_{NL}, provide the distance over which dispersive or nonlinear effects become important for a pulse propagating through the fiber. We can identify four different regimes:

- if $L \ll L_D$ and $L \ll L_{NL}$ the nonlinear and dispersive effects do not play a significant role during pulse propagation;
- if $L \gg L_D$ and $L \gg L_{NL}$ dispersion and non-linearity act together as the pulse propagates along the fiber;
- if $L \sim L_D$ and $L \ll L_{NL}$ the pulse evolution is governed by GVD;
- if $L \sim L_{NL}$ and $L \ll L_D$ the pulse evolution is governed by nonlinear effects.

We have experimentally observed that when the wave propagates in the amplifier fiber before entering in the PCF, first the Raman effects occur, next followed by MI (section 4.3.2). In order to confirm the hypothesis of a competition between MI and Raman Stokes conversion, we resorted to the following approximate calculation. Roughly speaking, the power spectral density Γ at the frequency Ω_{MI} where the MI gain is maximum can be evaluated as:

$$\Gamma(\Omega_{MI}) = \Gamma_{noise} e^{2\gamma P_0 z} \quad \textbf{(38)}$$

where z is the propagation distance, P_0 represents the quasi-CW pump power, Γ_{noise} is the average spectral density of noise.

For comparison, the maximum power spectral density at the frequency Ω_{max} ~13.2 THz where the Raman gain is maximum is

$$\Gamma(\Omega_{\max}) = \Gamma_{noise} e^{\delta + g_R P_0 z} \quad \textbf{(39)}$$

where δ is an additional gain factor accounting for prior amplification of the noise in the YDFA, and $g_R = 2\gamma f_R \,\mathrm{Im}\left[\chi_R(\Omega_{\max})\right]$ is the Raman gain coefficient with $f_R \sim 0.18$ and $\mathrm{Im}[\chi_R(\Omega_{\max})] \sim 1.39$ in silica glass. One can define some characteristic lengths for MI or Raman Stokes conversion as the lengths of propagation after which the power spectral density exceeds an arbitrary value of reference Γ_{ref}, respectively. Hence, the characteristic length for MI reads as

$$L_{MI} = \frac{1}{2\gamma P_0} \log\left(\Gamma_{ref} / \Gamma_{noise}\right) \quad \textbf{(40)}$$

and the characteristic length for Raman effect is given by

$$L_R = \frac{1}{g_R P_0}\left[\log\left(\Gamma_{ref} / \Gamma_{noise}\right) - \delta\right] \quad \textbf{(41)}$$

In case that $\delta = 0$ (that means without amplifier), then $L_R \sim 4 L_{MI}$, and hence the early stage of propagation is dominated by MI. In contrast, if $\delta > 0$, the Raman length decreases and eventually equals the MI length if $\delta \equiv \delta_0$, where

$$\delta_0 = \left[1 - \frac{g_R}{2\gamma}\right] \log\left(\Gamma_{ref} / \Gamma_{noise}\right) = \left\{1 - f_R \,\mathrm{Im}\left[\chi_R(\Omega_{\max})\right]\right\} \log\left(\Gamma_{ref} / \Gamma_{noise}\right) \quad \textbf{(42)}$$

However, if $\delta > \delta_0$, the Raman length will be shorter than the MI length and consequently, the Raman effect acts before MI sidebands appear. For example, if we consider a reference power spectral density that is 10 dB above that of the noise, then $\delta_0 \sim 1.726$ (Figure 4-10).

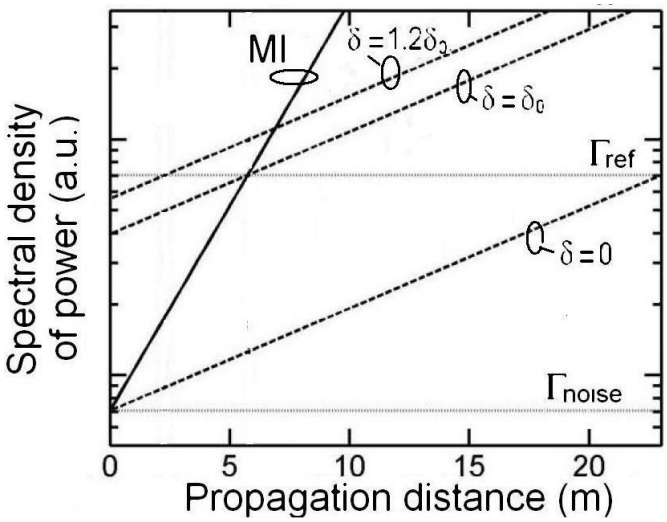

Figure 4-10: *Power spectral density vs. propagation distance z, for γ=0.02 m-1W-1 and P0=10 W. Dotted lines stand for Γ_{noise} and $\Gamma_{ref} = 10\,\Gamma_{noise}$, respectively. Solid line stands for the evolution of the maximum spectral density of power of MI sidebands. The dashed lines indicate the maximum spectral density of power of the Raman peak for the different cases when $\delta = 0$, and $\delta = 1.2\delta_0$, respectively.*

The GNLSE permits to calculate the evolution of the complex function E(t, z) representing the slowly varying envelope of the electric field at times t and position z.

From an experimental point of view, one often has access to only a part of this information. For instance, the spectrum recorded by an optical spectrum analyzer provide the spectral intensity associated to E(t, z), but not the corresponding phase. For this reason, several experimental techniques have been developed to characterize a pulse envelope in time and frequency as our recording set-up described before (Figure 4-5).

Even from a numerical point of view, where E(t, z) is completely calculated in modulus and phase, it is difficult to provide an appropriate representation which should represent a guide for further applications or experimental implementations.

For the CARS application, moreover, we need to verify the synchronization between signals pertaining to different spectral regions. It is then appropriate and a known procedure to provide a representation of the complex envelope E(t) in time and frequency. For ease of discussion we refer to a fixed position z along the fiber.

We define the spectrogram signal as

$$S(\omega,t)=\left|\int_{-\infty}^{+\infty}E(t)g(t-\tau)e^{-i\omega t}dt\right|^2 \quad \textbf{(43)}$$

For a fixed position z, the two variables of the spectrogram signal are the angular frequency ω and the time delay τ. For this reason a 3D representation is required.

g(t- τ) is a gating function of time: one can assume for simplicity a Gaussian shape. The spectrogram signal is then a real-valued function of two variables ω and τ, (we remind that we have chosen to fix the position within the fiber to a fixed coordinate value z). From a physical point of view one extracts different time portions of the complex signal E(t) by sliding the time-gating function g in different time positions. The spectrogram is then composed by the spectra corresponding to this set of time gating portions of the complex signal E(t). This representation then allows us a direct inspection of the complex field E(t) and provide an answer to the intuitive question whether two distinct spectral regions have been generated within the same time interval.

We have studied the SC generation in the two cases described in the experimental section. In the first case (CASE A) a transform-limited pulse is sent to a chain of two fibers: the first fiber segment has normal dispersion and should imitate the nonlinear and dispersive contribution of the amplifier; the second segment is the PCF used in the experiment. In CASE B the same input condition of case A is instead directly assumed as input condition for the GNLSE. Note that the output of any partial differential equation may be significantly conditioned by the input condition. In the case of partial differential equations the input condition is the function called

complex electric field envelope calculated at the input end of a given fiber segment $E(t, z=z_0)$. We discuss then the differences between the results of case A and case B by using the tool of the spectrogram signal: note that in both cases we consider the same PCF parameters and both cases consider the same input pulse. However the same PCF is excited, in the two cases, by two different input conditions: the laser spectrum broadened by the amplifier in case A, and the laser itself for case B.

Case A

We show here some numerical simulations assuming a sech shaped laser pulse of 32 ps and a peak power of 2kW. We consider a fiber length of PCF of 1 m and a nonlinear coefficient of 21 $km^{-1}W^{-1}$. The pulse duration is much shorter than that used in the experiment and this choice has been made to limit the computational effort. Of course this also means that the "wave packet" generated at each carrier frequencies of the SC are much shorter in time in the simulations than the ones generated in the experiment by the microchip laser. This means that the eventual pulse carving in temporal domain to be revealed in the simulations would require ideal detectors, again in the simulations much faster than the ones used in the experiments.
However, between the laser source and the PCF we assumed to have an intermediate lossless segment of fiber whose dispersion is simply the one of fiber glass, with a zero dispersion wavelength at 1273 nm and a dispersion value of -27.5 ps/(km nm). Hereafter this fiber segment will be indicate as standard monomode fiber (SMF). Such fiber segment is assumed to have a nonlinear coefficient of 4 $km^{-1}W^{-1}$ and a length of 7.5 m. Moreover, it is expected to model the dispersive and nonlinear contribution of the YDFA. Note that there is no gain included in this segment of fiber: it is not then a numerical simulation close to the experimental conditions but numerical simulations which give qualitatively similar results as those obtained at the output of the YDFA. Being in the normal dispersion regime this fiber segment gives a spectral reshape of the input pulse with a generation of a Raman Stokes sideband. We show in Figure 4.11 the spectrum at the output of the intermediate fiber segment. We observe the formation of a Raman Stokes sideband nearly 10 dB below the remaining pump pulse. The corresponding complex field envelope is then used as input condition for the PCF.

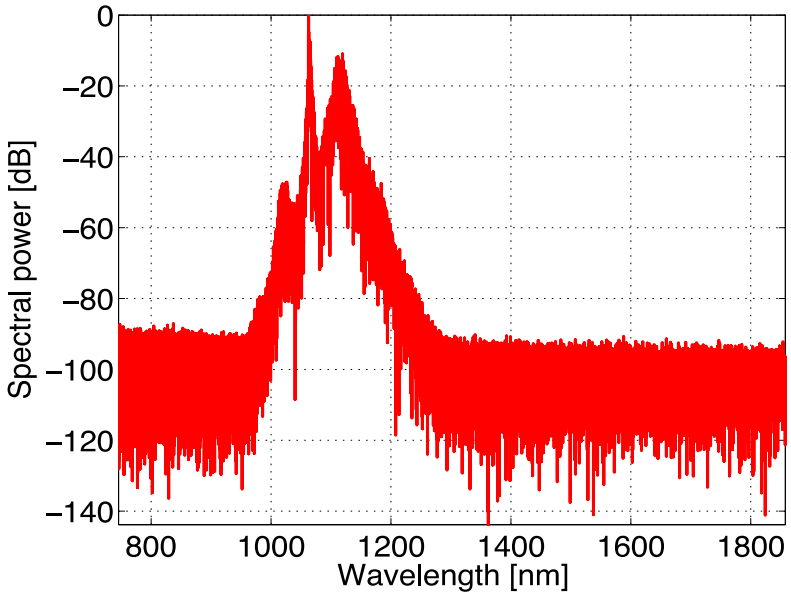

Figure 4-11: *Case A: numerically calculated optical spectrum at the output of the first fiber segment (silica dispersion only).*

Case B

In the case B the same laser pulse of case A (hyperbolic secant, 32 ps wide and 2kW of peak power) is directly used as input condition for the PCF, in absence of any intermediate. This would correspond to the practical case of direct coupling between the laser and the PCF in absence of any optical amplifier. We show the corresponding spectral power in Figure 4-12.

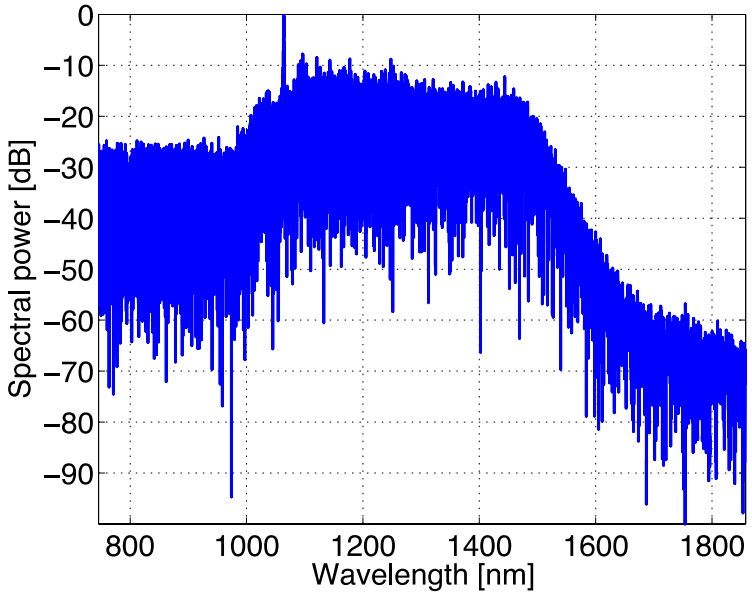

Figure 4-12: *Case B: numerically calculated optical spectrum at the PCF output.*

Comparison between Case A and Case B

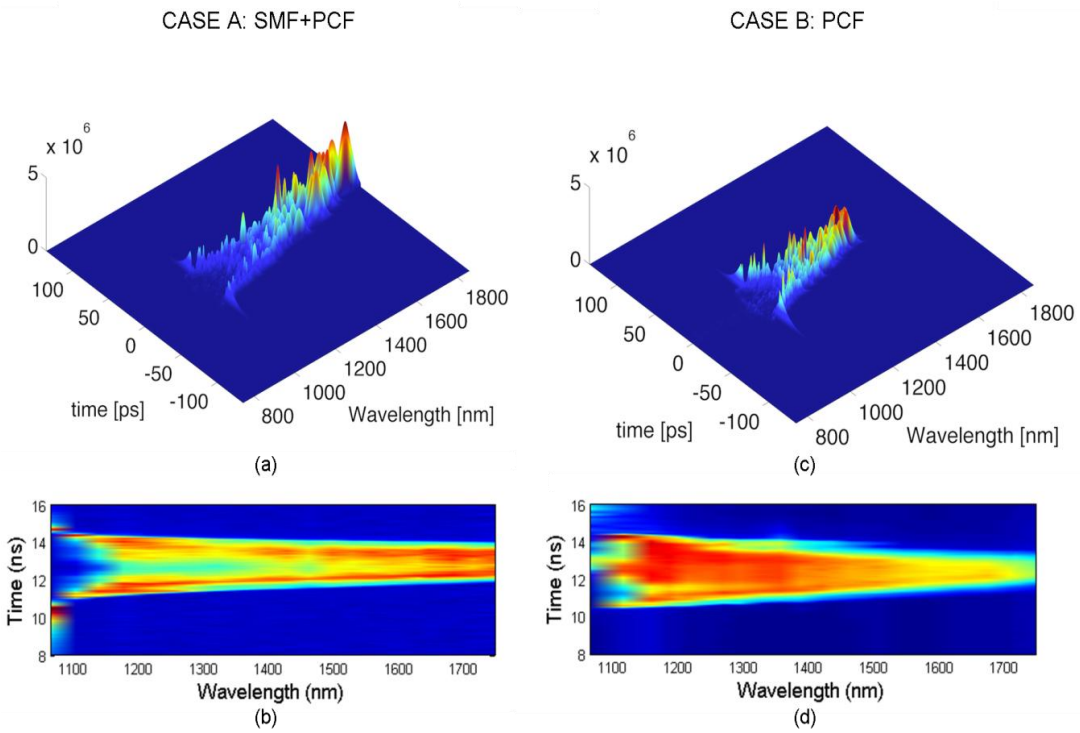

Figure 4-13: *Comparison between the simulated (a)-(c), and experimental (b)-(d) spectrograms, representing the temporal evolution of the pulses forming the SC wave in the range 1000-1800 nm, in the case A in which the input pulse propagates first in the SMF and next in PCF, and in the case B (only PCF), respectively.*

We now analyze carefully the spectrogram signal at the output of the PCF for case A (left) and case B (right). Despite the input signal from the laser is the same, the presence of the intermediate segment SMF makes case A qualitatively different from case B. We observe first of all that the combined action of SMF and PCF gives a spectrum broader than the case of PCF alone. This fact seems consistent with the experimental observation (reported below). The two spectrograms have been represented under the same vertical scales. We now focus on the temporal signal per frequency band. In both cases we observe that the original temporal waveform is carved and at all wavelengths between 1064 and 1150 nm the temporal waveform is composed by two sharp edges temporally spaced by same fraction of the original pulse duration. Upon wavelength this temporal waveform reminds a sort of “two riverbanks” gradually merging for wavelengths above 1150 nm. We noticed that between these two “riverbanks”, in the region 1060-1150 nm, there are slightly less fluctuations in temporal signal for case A than for case B. In practice, this effect is much more striking in the experiments than in the simulations. This is fact may be explained by the large difference between the laser and fiber parameters used in the experiments and their numerical counterpart.

4.3.4 Spectral broadening and nonlinear "saturable transparency"

In a second experiment, we recorded the pulse profile at a given wavelength of 1204 nm for several values of the input peak powers. For a low pump power the converted pulse exhibits a quasi-square shape of 400 ps duration (FWHM) (Figure 4-14). As the pump energy increases, the peak power of the converted pulse progressively grows until it saturates. At this stage the maximum peak power is close to 800 W for pulse duration of 1 ns. Beyond this value and further increasing the pump, only the energy of the converted pulse increases whereas the peak power saturates. A square pulse envelop of more than 2.6 ns duration with a large central depletion induced by the stimulated Raman is obtained. This saturation is mainly due to the effect of SSFS. Indeed, after the temporal reshaping of the sub-nanosecond input pulse into several solitonic waves, each soliton is shifted toward another wavelength when exceeding a given intensity threshold. The remaining energy represents the low energy part of the solitonic pulse unaffected by SSFS. This effect of spectral shift obtained above an intensity threshold at a given wavelength, mimics the effect of a "saturable transparency", and creates a continuum with a limited peak power fixed by the SSFS threshold (Figure 4-14(b)).

Here, the distortion undergone by the input pulse during the continuum generation dramatically changes the overlap between the Stokes and the pump waves. In the time domain, because of the nonlinear conversion obtained down to the pump pulses edges, large infrared pulses are obtained. An increase of the input pulse power leading to the continuum generation does not overcome this drawback. Indeed, for higher peak power, a broader continuum is obtained with longer wavelengths in the IR domain while the energy at intermediate wavelengths, located in the central part of the continuum, grows by means of a temporal broadening keeping constant their peak power. Because of the linear dependence of the CARS signal with respect to the Stokes peak power, no improvement of the output signal is obtained by increasing the input pulse peak power at the PCF input.

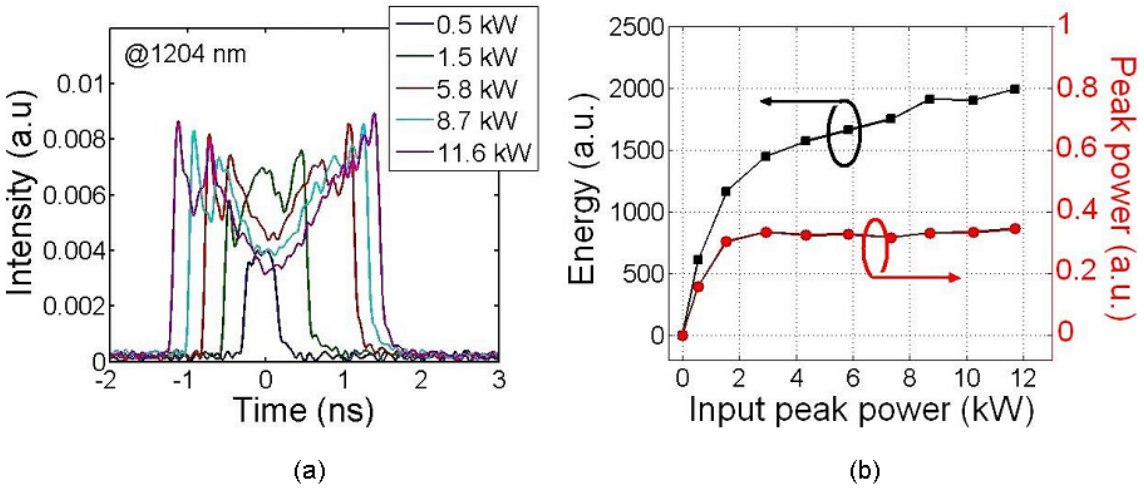

Figure 4-14: *(a) Variation of the PCF output pulse profile at 1204 nm for several input peak power; (b) PCF output energy and peak power evolution of the 1204 nm-pulse versus amplifier peak power at the PCF input.*

4.4 Conclusion

We have proposed a new compact laser source specifically designed for fast multiplex-CARS microspectroscopy. This ultrabroadband light source is based on the combination of a sub-nanosecond microchip laser with a repetition rate of 75 kHz, an YDFA amplifier and an air-silica PCF. Since we increase the repetition rate, the laser peak power is not high enough for inducing an efficient spectral broadening into the PCF. Consequently, using an optical amplifier becomes necessary.

We performed a detailed analysis of the time-frequency distortions undergone by the Stokes wave during nonlinear propagation in fiber amplifier and PCF. These distortions represent a temporal broadening of the Stokes pulses that makes the Stokes/pump pulses synchronization difficult.

We pointed out the impact of Raman effect interplaying with modulation instability and soliton propagation upon the generation of the SC used as Stokes component for multiplex-CARS application. The nonlinear temporal broadening of the Stokes pulse is mainly due to the depletion of the upper part of the pulse that undergoes the Raman and solitonic effects. The role played by the competition between Raman effect and MI has been also confirmed by numerical simulations.

Concerning the dispersive effects, a weak impact of group velocity dispersion is observed during propagation in the PCF thanks to both the sub-nanosecond duration of the pump pulse (less sensitive to GVD with respect to shorter pulses) and the short length of the fiber ($L < L_D$). However, we demonstrated that the temporal superposition between the pump and the Stokes

beam is dramatically impaired since less than half of the initial energy of the Stokes wave contributes to the CARS process. We emphasize the saturation of the Stokes wave peak power during SC generation because of SSFS. This effect limits the CARS efficiency and cannot be compensated simply by increasing the initial pulse peak power.

Nevertheless, preliminary tests have been performed by our Japan partner in order to verify the applicability of this laser source to M-CARS microspectroscopy. They recorded the CARS spectra of indene samples, represented in Fig. The results open the way to the use of sub-nanosecond microchip-based SC sources in the CARS applications, as a better alternative to the usual picosecond or femtosecond laser sources.

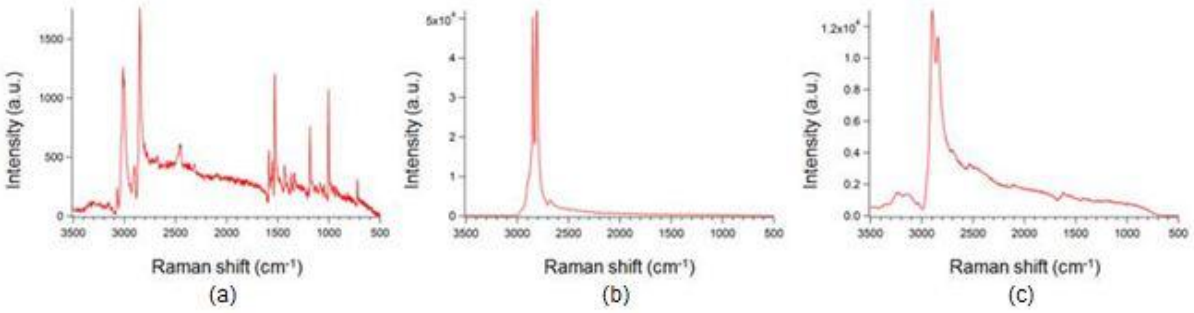

Figure 4-15: *M-CARS spectra of (a) indene, (b) parafilm, and (c) human hair.*

General Conclusion

Since the discovery that an intense electric field is able to induce changes in TMP and, consequently, changes in its permeability, the so called electroporation phenomenon has drawn great interest in the bioelectromagnetic community. Indeed, the millisecond and microsecond pulses inducing effects on biological cell are currently used in different applications, both industrial and biomedical (bacterial decontamination, electrochemotherapy, cell fusion, drug delivery…) [14], [187]. More recently, nanopulse effects have been studied as their shorter duration permits to apply stronger electric field (order of kV/m) avoiding thermal effects, minimizing the damages of biological tissue. Additionally, nanopulses seem to have bioeffects on internal cell membranes, potentially permitting the manipulation of subcellular structures [12].

From the first experiments demonstrating cell membrane electroporation, several theoretical description have been proposed, based on assumptions of elastic deformation of the lipid bilayer forming the cell membrane [188], or on molecular-level events such as phase transition [189], or on breakdown of the lipid/suspension interfaces [190]. Nowadays, is widely accepted the hypothesis of aqueous pore formation through the membrane due to an electric-field-induced polarization of the bilayer and the contacting water molecules. There is also a discrepancy between the molecular dynamic simulations and the experimental results: the simulations predict that the pore formation occurs within several nanosecond, whereas experiments show a lag of several microseconds between the onset of the pulse and that of detectable transmembrane transport [11], [23]. It is also difficult to delivery short-duration, high-intensity pulses with different shapes without affecting the biological environment. Additionally, there is a lack of fast and submicrometer-resolution imaging techniques suitable for the detection of subcellular-scale phenomena.

In this context, the objective of my PhD work was to provide a complete and compact system that satisfies the requirements mentioned above, and in which the electrical and the optical technologies work together. To reach this purpose, we have used a common sub-nanosecond powerchip laser with a double function: 1) triggering the photocommutation process for the electric pulse generation trough a microstrip line pulse generator, and 2) providing the seeding beam for the M-CARS microscopy source. The whole system consists of two coupled devices perfectly synchronized at the sub-nanosecond scale: an electrical pump and an optical probe.

First, we have designed and realized a flexible and nanoporation-suitable electric pulse generator, based on the microsctrip line geometry and on the laser-triggered optoelectronic switching already tested and characterized in previous works of our equip [16–18], [72], [172].

The generator permits to obtain square or bipolar pulses with durations of 1ns or 2 ns and amplitude up to 4 kV. Its low timing jitter (< 3 ps) and the linear regime of the switches allow the synchronization with the optical system. The studied system is also able to produce nanosecond pulses with adjustable spectral and temporal shape.

Next, we have studied the existing possible ways to efficiently deliver the pulsed electric field to the cells under microscope [19], [20], [74]. We have chosen the geometry of a microchamber, consisting of two biocompatible electrodes forming the microchannel where cells in suspension are injected. Particular attention has been paid in the impedance matching in the system composed by the generator, the microchamber and the biological solution, in order to maximize the energy delivered to the cells and avoid any pulse profile distortion.

Finally, we have conceived a M-CARS laser source that brings some innovations on the currently sources presents in the domain literature. The main innovations concern the sub-nanosecond regime of the optical pulses with respect to the usual femtosecond or picosecond regimes, and the use of only one laser providing both the pump and the Stokes beams for the M-CARS process. The sub-nanosecond laser source exhibits low cost and compact device that permits a less complex setting up in comparison with other sources already published. Beyond these technical characteristics, the sub-nanosecond pump regime improves also the imaging efficiency thanks to its higher spectral resolution. This implies a better intrinsic vibrational contrast and an increased ratio between the resonant signal and nonresonant background. Moreover, as in the sub-nanosecond regime the different spectral components of the beam are less sensitive to the group velocity dispersion in fiber, the pump/Stokes beams synchronization is easier.

From an optical nonlinear process point of view, the sub-nanosecond seeding regime provides a broader SC than that is generated by shorter pulses, extending the interaction spectral region for the M-CARS signals. This effect is explained through the nonlinear effects occurring in the optical fiber used to this scope. In particular, the main role of the soliton built-up, starting from MI, soliton self-frequency shift and soliton collisions has been highlighted. Both the simulation and the experimental results have showed that the number of solitons produced by MI explains why a longer input pulse leads to a larger IR bandwidth at the output: more solitons means more collisions, so more possibilities to exacerbate the SSFS of the most energetic soliton [179]. Finally, with the sub-nanosecond powerchip laser we have able to obtain a stable SC beam ranging from about 500 nm to 2000 nm. Furthermore, we easily synchronized the pump beam with the Stokes one by means of a Herriott's cavity and a linear delay line.

Despite the perfect beam synchronization and superposition, adjusted and optimized by maximizing the SFG in a KDP crystal, we did not obtain CARS signals neither of the crystal nor of polystyrene beads. The main problems that limit the CARS signal detection can be summarized in three points. The first point deals with the low average power delivered by the pump source

producing pulses with only 500 Hz of repetition rate. The second one could arise from our detection system that is not temporally synchronized with the pump laser source. At last, a single optical grating used to spectrally separate all the CARS contributions should be not sufficient in order to select the CARS signal among SC radiations, not filtered after sample exposition. Consequently, a too low signal-to-noise ratio could be at the origin of our problems.

In a last time, we developed and studied another M-CARS laser, able to generate two synchronized beams, the one monochromatic, and the other polychromatic. In this work, we used a sub-nanosecond microchip seeding laser with a repetition rate higher than that used in the previous system. We then used have needed a fiber amplifier followed by a microstructured optical fiber in order to generate the SC Stokes beam. The nonlinear behaviour obtained in the fibers introduced some temporal and spectral distortions, making the pump/Stokes synchronization difficult. A detailed analysis of the energy distribution over the SC spectral range has been experimentally and numerically performed. Thanks to both the sub-nanosecond duration of the pump pulse and the short length of the fiber, a weak impact of dispersion and group velocity dispersion is observed during propagation in the PCF. We also demonstrated that the temporal superimposition between the pump and the Stokes beam is dramatically impaired since less than half of the initial energy of the Stokes wave contributes to the CARS process. Nevertheless, the pump/Stokes superposition is possible and efficient over the biological interest region (700-3500 cm^{-1}). We also emphasize the saturation of the Stokes wave peak power during SC generation because of SSFS. This effect limits CARS efficiency and cannot be compensated simply by increasing the initial pulse peak power. Despite the identified spectral and temporal distortions of the Stokes beam, this original high repetition rate sub-nanosecond source has been used to perform M-CARS measurements of different samples. CARS spectra of indene, yeast cell and human hair, among others, have been obtained by our Japanese colleagues [130–132], [140]. These results open the way to the use of amplified sub-nanosecond microchip-based SC sources in M-CARS applications, as a better alternative to the widespread picosecond or femtosecond laser sources.

The results of my PhD work concerning the design and realization of optoelectronic generator and microscopy-suitable exposure system as well as M-CARS sources, has been largely diffused within the bioeletromagnetic and optic scientific community. Two papers are published in different international peer reviewed journals and one has been submitted. The studies on M-CARS sub-nanosecond sources have been presented within five international and two national conferences. Moreover, the high repetition rate M-CARS source has been the object of a patent [183].

Bibliography

[1] C. Polk et E. Postow, *Handbook of Biological Effects of Electromagnetic Fields*. CRC Press, 1996.

[2] K. H. Schoenbach, R. P. Joshi, R. H. Stark, F. C. Dobbs, et S. J. Beebe, « Bacterial decontamination of liquids with pulsed electric fields », *Dielectrics and Electrical Insulation, IEEE Transactions on*, vol. 7, nº. 5, p. 637–645, 2000.

[3] G. Sersa, T. Cufer, S. M. Paulin, M. Cemazar, et M. Snoj, « Electrochemotherapy of chest wall breast cancer recurrence », *Cancer Treatment Reviews*, vol. 38, nº. 5, p. 379-386, août 2012.

[4] M. P. Rols, J. M. Bachaud, P. Giraud, C. Chevreau, H. Roche, et J. Teissie, « Electrochemotherapy of cutaneous metastases in malignant melanoma », *Melanoma research*, vol. 10, nº. 5, p. 468–474, 2000.

[5] L. M. Mir, L. F. Glass, G. Sersa, J. Teissié, C. Domenge, D. Miklavcic, M. J. Jaroszeski, S. Orlowski, D. S. Reintgen, Z. Rudolf, M. Belehradek, R. Gilbert, M. P. Rols, J. Belehradek, J. M. Bachaud, R. DeConti, B. Stabuc, M. Cemazar, P. Coninx, et R. Heller, « Effective treatment of cutaneous and subcutaneous malignant tumours by electrochemotherapy. », *Br J Cancer*, vol. 77, nº. 12, p. 2336-2342, juin 1998.

[6] L. C. Van Dinten, J. A. Den Boon, A. L. M. Wassenaar, W. J. M. Spaan, et E. J. Snijder, « An infectious arterivirus cDNA clone: identification of a replicase point mutation that abolishes discontinuous mRNA transcription », *Proceedings of the National Academy of Sciences*, vol. 94, nº. 3, p. 991, 1997.

[7] M. G. Delgadillo, D. R. Liston, K. Niazi, et P. J. Johnson, « Transient and selectable transformation of the parasitic protist Trichomonas vaginalis », *Proceedings of the National Academy of Sciences*, vol. 94, nº. 9, p. 4716, 1997.

[8] T. Saito et N. Nakatsuji, « Efficient gene transfer into the embryonic mouse brain using in vivo electroporation », *Dev. Biol.*, vol. 240, nº. 1, p. 237-246, déc. 2001.

[9] M. R. Prausnitz, « A practical assessment of transdermal drug delivery by skin electroporation », *Advanced drug delivery reviews*, vol. 35, nº. 1, p. 61–76, 1999.

[10] T. Kotnik et D. Miklavcic, « Theoretical evaluation of voltage inducement on internal membranes of biological cells exposed to electric fields », *Biophysical journal*, vol. 90, nº. 2, p. 480–491, 2006.

[11] T. Kotnik, P. Kramar, G. Pucihar, D. Miklavcic, et M. Tarek, « Cell membrane electroporation-Part 1: The phenomenon », *Electrical Insulation Magazine, IEEE*, vol. 28, nº. 5, p. 14–23, 2012.

[12] T. Kotnik, D. Miklavčič, et L. M. Mir, « Cell membrane electropermeabilization by symmetrical bipolar rectangular pulses: Part II. Reduced electrolytic contamination », *Bioelectrochemistry*, vol. 54, nº. 1, p. 91-95, août 2001.

[13] T. Kotnik, G. Pucihar, M. Rebersek, D. Miklavcic, et L. M. Mir, « Role of pulse shape in cell membrane electropermeabilization », *Biochimica et Biophysica Acta (BBA)-Biomembranes*, vol. 1614, nº. 2, p. 193–200, 2003.

[14] K. H. Schoenbach, S. Katsuki, R. H. Stark, E. S. Buescher, et S. J. Beebe, « Bioelectrics-new applications for pulsed power technology », *Plasma Science, IEEE Transactions on*, vol. 30, nº. 1, p. 293–300, 2002.

[15] M. Kenaan, S. E. Amari, A. Silve, C. Merla, L. M. Mir, V. Couderc, D. Arnaud-Cormos, et P. Leveque, « Characterization of a 50- Omega Exposure Setup for High-Voltage Nanosecond Pulsed Electric Field Bioexperiments », *Biomedical Engineering, IEEE Transactions on*, vol. 58, nº. 1, p. 207–214, 2011.

[16] C. Merla, S. El Amari, M. Kenaan, M. Liberti, F. Apollonio, D. Arnaud-Cormos, V. Couderc, et P. Leveque, « A 10-Omega high-voltage nanosecond pulse generator », *IEEE transactions on microwave theory and techniques*, vol. 58, nº. 12, p. 4079–4085, 2010.

[17] El Amari Saad, « Développement et caractérisation de générateur optoélectronique d'impulsions de champ électrique nanoseconde et subnanoseconde de forte intensité: application au domaine biomédical », Electronique des Haute frequences, Photonique et systèmes, Université de Limoges, 2011.

[18] C. Merla, S. El-Amari, F. Danei, M. Liberti, F. Apollonio, D. Arnaud-Cormos, V. Couderc, et P. Leveque, « Microstrip-based nanosecond pulse generators: Numerical and circuital modeling », in *Microwave Symposium Digest (MTT), 2010 IEEE MTT-S International*, p. 101–104.

[19] Kenaan Mohamad, « Développement d'applicateurs pour étudier le comportement des cellules biologiques soumises à des impulsions électromagnetiques ultracourtes », Université de Limoges, 2010.

[20] D. Arnaud-Cormos, P. Leveque, Y.-H. Wu, J. M. Sanders, M. A. Gundersen, et P. T. Vernier, « Microchamber Setup Characterization for Nanosecond Pulsed Electric Field Exposure », *IEEE Transactions on Biomedical Engineering*, vol. 58, nº. 6, p. 1656 -1662, juin 2011.

[21] M. Kenaan, M. G. Moisescu, T. Savopol, D. Martin, D. Arnaud-Cormos, et P. Leveque, « Dosimetry of an in vitro exposure system for fluorescence measurements during 2.45 GHz microwave exposure », *International Journal of Microwave and Wireless Technologies*, vol. 3, nº. 01, p. 81–86, 2011.

[22] P. Jarrige, N. Ticaud, S. Kohler, R. P. O'Connor, L. Duvillaret, G. Gaborit, D. Arnaud-Cormos, et P. Leveque, « Electrooptic Probe Adapted for Bioelectromagnetic Experimental Investigations », *IEEE Transactions on Instrumentation and Measurement*, vol. 61, nº. 7, p. 2051 -2058, juill. 2012.

[23] F. Apollonio, M. Liberti, P. Marracino, et L. Mir, « Electroporation mechanism: Review of molecular models based on computer simulation », in *Antennas and Propagation (EUCAP), 2012 6th European Conference on*, 2012, p. 356–358.

[24] A. Silve, N. Dorval, T. Schmid, L. M. Mir, et B. Attal-Tretout, « A wide-field arrangement for single-shot CARS imaging of living cells », *Journal of Raman Spectroscopy*, 2012.

[25] J. White, U. Pliquett, P. Blackmore, R. Joshi, K. Schoenbach, et J. Kolb, « Plasma membrane charging of Jurkat cells by nanosecond pulsed electric fields », *European Biophysics Journal*, vol. 40, nº. 8, p. 947-957, 2011.

[26] Staempfli, « Reversible breakdown of the excitable membrane of a Ranvier node », *An. Acad. Brasil. Ciens*, vol. 30, p. 57, 1958.

[27] R. J. Turnbull, E. Neumann, et K. Rosenheck, « An alternate explanation for the permeability changes induced by electrical impulses in vesicular membranes », *The Journal of Membrane Biology*, vol. 14, p. 193-196, déc. 1973.

[28] C. Merla, A. Denzi, A. Paffi, M. Casciola, G. d' Inzeo, F. Apollonio, et M. Liberti, « Novel Passive Element Circuits for Microdosimetry of Nanosecond Pulsed Electric Fields », *Biomedical Engineering, IEEE Transactions on*, vol. 59, nº. 8, p. 2302–2311, 2012.

[29] A. Ogura, J. Matsuda, et R. Yanagimachi, « Birth of normal young after electrofusion of mouse oocytes with round spermatids », *Proceedings of the National Academy of Sciences*, vol. 91, nº. 16, p. 7460, 1994.

[30] K. H. Schoenbach, S. J. Beebe, et E. S. Buescher, « Intracellular effect of ultrashort electrical pulses », *Bioelectromagnetics*, vol. 22, nº. 6, p. 440–448, 2001.

[31] S. J. Beebe, P. M. Fox, L. J. Rec, E. L. K. Willis, et K. H. Schoenbach, « Nanosecond, high-intensity pulsed electric fields induce apoptosis in human cells », *The FASEB journal*, vol. 17, nº. 11, p. 1493–1495, 2003.

[32] K. J. Müller, V. L. Sukhorukov, et U. Zimmermann, « Reversible Electropermeabilization of Mammalian Cells by High-Intensity, Ultra-Short Pulses of Submicrosecond Duration », *Journal of Membrane Biology*, vol. 184, nº. 2, p. 161-170, 2001.

[33] P. T. Vernier, A. Li, L. Marcu, C. M. Craft, et M. A. Gundersen, « Ultrashort pulsed electric fields induce membrane phospholipid translocation and caspase activation: differential sensitivities of Jurkat T lymphoblasts and rat glioma C6 cells », *Dielectrics and Electrical Insulation, IEEE Transactions on*, vol. 10, nº. 5, p. 795–809, 2003.

[34] P. T. Vernier, Y. Sun, L. Marcu, S. Salemi, C. M. Craft, et M. A. Gundersen, « Calcium bursts induced by nanosecond electric pulses », *Biochemical and biophysical research communications*, vol. 310, nº. 2, p. 286–295, 2003.

[35] S. S. Scarlett, J. A. White, P. F. Blackmore, K. H. Schoenbach, et J. F. Kolb, « Regulation of intracellular calcium concentration by nanosecond pulsed electric fields », *Biochimica et Biophysica Acta (BBA)-Biomembranes*, vol. 1788, nº. 5, p. 1168–1175, 2009.

[36] S. J. Beebe, P. Fox, L. Rec, K. Somers, R. H. Stark, et K. H. Schoenbach, « Nanosecond pulsed electric field (nsPEF) effects on cells and tissues: apoptosis induction and tumor growth inhibition », *Plasma Science, IEEE Transactions on*, vol. 30, nº. 1, p. 286–292, 2002.

[37] B. Alberts, *Essential Cell Biology: An introducton to the Molecular Biology of the Cell*, vol. 2. Garland, 1997.

[38] K. H. Schoenbach, F. E. Peterkin, I. Alden, R.W., et S. J. Beebe, « The effect of pulsed electric fields on biological cells: experiments and applications », *IEEE Transactions on Plasma Science*, vol. 25, nº. 2, p. 284 - 292, avr. 1997.

[39] M. Stoneman, A. Chaturvedi, D. B. Jansma, M. Kosempa, C. Zeng, et V. Raicu, « Protein influence on the plasma membrane dielectric properties: In vivo study utilizing dielectric spectroscopy and fluorescence microscopy », *Bioelectrochemistry*, vol. 70, nº. 2, p. 542-550, mai 2007.

[40] A. Agarwal, I. Zudans, E. A. Weber, J. Olofsson, O. Orwar, et S. G. Weber, « Effect of Cell Size and Shape on Single-Cell Electroporation », *Anal. Chem.*, vol. 79, nº. 10, p. 3589-3596, mai 2007.

[41] R. V. Davalos, L. M. Mir, et B. Rubinsky, « Tissue ablation with irreversible electroporation », *Annals of biomedical engineering*, vol. 33, nº. 2, p. 223–231, 2005.

[42] L. M. Mir, *Proceedings of the Electroporation based technologies and treatments: International Scientific Workshop and Postgraduate Course, November 15-21, 2009, Ljubljana, Slovenia*. Založba FE in FRI, 2009.

[43] M. Golzio, M. P. Rols, et J. Teissie, « In vitro and in vivo electric field-mediated permeabilization, gene transfer, and expression », *Methods*, vol. 33, nº. 2, p. 126–135, 2004.

[44] J. C. Weaver, « Electroporation theory », *Methods in molecular biology*, vol. 28, p. 3–28, 1995.

[45] C. Merla, A. Paffi, F. Apollonio, P. Leveque, G. d' Inzeo, et M. Liberti, « Microdosimetry for nanosecond pulsed electric field applications: a parametric study for a single cell », *Biomedical Engineering, IEEE Transactions on*, vol. 58, nº. 5, p. 1294–1302, 2011.

[46] W. Frey, J. White, R. Price, P. Blackmore, R. Joshi, R. Nuccitelli, S. Beebe, K. Schoenbach, et J. Kolb, « Plasma membrane voltage changes during nanosecond pulsed electric field exposure », *Biophysical journal*, vol. 90, nº. 10, p. 3608–3615, 2006.

[47] A. G. Pakhomov, J. F. Kolb, J. A. White, R. P. Joshi, S. Xiao, et K. H. Schoenbach, « Long-lasting plasma membrane permeabilization in mammalian cells by nanosecond pulsed electric field (nsPEF) », *Bioelectromagnetics*, vol. 28, nº. 8, p. 655–663, 2007.

[48] A. G. Pakhomov, R. Shevin, J. A. White, J. F. Kolb, O. N. Pakhomova, R. P. Joshi, et K. H. Schoenbach, « Membrane permeabilization and cell damage by ultrashort electric field shocks », *Archives of biochemistry and biophysics*, vol. 465, nº. 1, p. 109–118, 2007.

[49] E. S. Buescher, R. R. Smith, et K. H. Schoenbach, « Submicrosecond intense pulsed electric field effects on intracellular free calcium: mechanisms and effects », *Plasma Science, IEEE Transactions on*, vol. 32, nº. 4, p. 1563–1572, 2004.

[50] E. Tekle, H. Oubrahim, S. M. Dzekunov, J. F. Kolb, K. H. Schoenbach, et P. Chock, « Selective field effects on intracellular vacuoles and vesicle membranes with nanosecond electric pulses », *Biophysical journal*, vol. 89, nº. 1, p. 274–284, 2005.

[51] T. Kotnik, F. Bobanovic, et others, « Sensitivity of transmembrane voltage induced by applied electric fields–A theoretical analysis », *Bioelectrochemistry and bioenergetics*, vol. 43, nº. 2, p. 285–291, 1997.

[52] C. Merla, A. Paffi, F. Apollonio, P. Leveque, et M. Liberti, « Microdosimetry applied to nanosecond pulsed electric fields: a comparison on a single cell between real and ideal waveforms », in *Engineering in Medicine and Biology Society, EMBC, 2011 Annual International Conference of the IEEE*, 2011, p. 302–305.

[53] P. T. Vernier, Y. Sun, L. Marcu, C. M. Craft, et M. A. Gundersen, « Nanosecond pulsed electric fields perturb membrane phospholipids in T lymphoblasts », *FEBS letters*, vol. 572, nº. 1-3, p. 103–108, 2004.

[54] A. Silve, I. Leray, B. Al-Sakere, et L. M. Mir, « Nanopulses and their applications: Permeabilisation to bleomycin molecules by 10 ns duration electric pulses in a tumor model in vivo », in *2012 6th European Conference on Antennas and Propagation (EUCAP)*, 2012, p. 348 -350.

[55] Y. Rosemberg et R. Korenstein, « Electroporation of the photosynthetic membrane:: A study by intrinsic and external optical probes », *Biophysical journal*, vol. 58, nº. 4, p. 823–832, 1990.

[56] M.-P. Rols et J. Teissié, « Electropermeabilization of Mammalian Cells to Macromolecules: Control by Pulse Duration », *Biophysical Journal*, vol. 75, nº. 3, p. 1415-1423, sept. 1998.

[57] G. Pucihar, L. M. Mir, et D. Miklavcic, « The effect of pulse repetition frequency on the uptake into electropermeabilized cells in vitro with possible applications in electrochemotherapy »,

Bioelectrochemistry, vol. 57, nº. 2, p. 167–172, 2002.

[58] P. T. Vernier, M. M. S. Thu, L. Marcu, C. M. Craft, et M. A. Gundersen, « Nanosecond electroperturbation-mammalian cell sensitivity and bacterial spore resistance », *Plasma Science, IEEE Transactions on*, vol. 32, nº. 4, p. 1620–1625, 2004.

[59] J. Zhang, P. F. Blackmore, B. Y. Hargrave, S. Xiao, S. J. Beebe, et K. H. Schoenbach, « Nanosecond pulse electric field (nanopulse): A novel non-ligand agonist for platelet activation », *Archives of biochemistry and biophysics*, vol. 471, nº. 2, p. 240–248, 2008.

[60] R. Nuccitelli, U. Pliquett, X. Chen, W. Ford, R. James Swanson, S. J. Beebe, J. F. Kolb, et K. H. Schoenbach, « Nanosecond pulsed electric fields cause melanomas to self-destruct », *Biochemical and biophysical research communications*, vol. 343, nº. 2, p. 351–360, 2006.

[61] K. H. Schoenbach, R. P. Joshi, J. F. Kolb, N. Chen, M. Stacey, P. F. Blackmore, E. S. Buescher, et S. J. Beebe, « Ultrashort electrical pulses open a new gateway into biological cells », *Proceedings of the IEEE*, vol. 92, nº. 7, p. 1122–1137, 2004.

[62] R. P. Joshi et K. H. Schoenbach, « Bioelectric effects of intense ultrashort pulses », *Crit Rev Biomed Eng*, vol. 38, nº. 3, p. 255-304, 2010.

[63] Q. Hu et Reviranda P. Joshi, « Transmembrane voltage analysis cells in response to an intense ultrashort electrical pulse », *Physical Review E*, vol. 79, p. 1-11, 2009.

[64] 15. Ravindra P. Joshi et 1. K. H. Schoenbach, « Modeling studies of cell response to ultrashort, high-intensity electric fields-Implication for intracellular manipulation », *IEEE TRANSACTIONS ON PLASMA SCIENCE*, vol. 32, p. 1677-1686, 2004.

[65] E. H. Hall, K. H. Schoenbach, et S. J. Beebe, « Nanosecond pulsed electric fields induce apoptosis in p53-wildtype and p53-null HCT116 colon carcinoma cells », *Apoptosis*, vol. 12, nº. 9, p. 1721–1731, 2007.

[66] R. Nuccitelli, X. Chen, A. G. Pakhomov, W. H. Baldwin, S. Sheikh, J. L. Pomicter, W. Ren, C. Osgood, R. J. Swanson, J. F. Kolb, et others, « A new pulsed electric field therapy for melanoma disrupts the tumor's blood supply and causes complete remission without recurrence », *International Journal of Cancer*, vol. 125, nº. 2, p. 438–445, 2009.

[67] M. Behrend, A. Kuthi, X. Gu, P. T. Vernier, L. Marcu, C. M. Craft, et M. A. Gundersen, « Pulse generators for pulsed electric field exposure of biological cells and tissues », *Dielectrics and Electrical Insulation, IEEE Transactions on*, vol. 10, nº. 5, p. 820–825, 2003.

[68] J. F. Kolb, S. Kono, et K. H. Schoenbach, « Nanosecond pulsed electric field generators for the study of subcellular effects », *Bioelectromagnetics*, vol. 27, nº. 3, p. 172–187, 2006.

[69] C. Eing, S. Bonnet, M. Pacher, H. Puchta, et W. Frey, « Effects of nanosecond pulsed electric field exposure on arabidopsis thaliana », *Dielectrics and Electrical Insulation, IEEE Transactions on*, vol. 16, nº. 5, p. 1322–1328, 2009.

[70] M. T. Chen, C. Jiang, P. T. Vernier, Y. H. Wu, et M. Gundersen, « Two-dimensional nanosecond electric field mapping based on cell electropermeabilization », *PMC biophysics*, vol. 2, nº. 1, p. 9, 2009.

[71] B. Vergne, V. Couderc, et P. Leveque, « A 30-kHz Monocycle Generator Using Linear Photoconductive Switches and a Microchip Laser », *Photonics Technology Letters, IEEE*, vol. 20, nº. 24, p. 2132 -2134, déc. 2008.

[72] S. El Amari, M. Kenaan, C. Merla, B. Vergne, D. Arnaud-Cormos, P. Leveque, et V. Couderc, « Kilovolt, nanosecond, and picosecond electric pulse shaping by using optoelectronic switching », *Photonics Technology Letters, IEEE*, vol. 22, nº. 21, p. 1577–1579, 2010.

[73] Y. Sun, P. Vernier, M. Behrend, L. Marcu, et M. Gundersen, « Microscope Slide Electrode Chamber for Nanosecond, Megavolt-Per-Meter Biological Investigations », *NSTI-Nanotech*, vol. 1, p. 485-488, 2004.

[74] C. Dalmay, J. Villemejane, V. Joubert, A. Silve, D. Arnaud-Cormos, O. Français, L. Mir, P. Leveque, et B. Le Pioufle, « A microfluidic biochip for the nanoporation of living cells », *Biosensors and Bioelectronics*, 2011.

[75] K. Walker III, O. N. Pakhomova, J. Kolb, K. S. Schoenbach, B. E. Stuck, M. R. Murphy, et A. G. Pakhomov, « Oxygen enhances lethal effect of high-intensity, ultrashort electrical pulses », *Bioelectromagnetics*, vol. 27, nº. 3, p. 221–225, 2006.

[76] J. Morren, B. Roodenburg, et S. W. H. de Haan, « Electrochemical reactions and electrode corrosion in pulsed electric field (PEF) treatment chambers », *Innovative Food Science & Emerging Technologies*, vol. 4, nº. 3, p. 285-295, sept. 2003.

[77] O. P. Hamill, A. Marty, E. Neher, B. Sakmann, et F. J. Sigworth, « Improved patch-clamp techniques for high-resolution current recording from cells and cell-free membrane patches », *Pfl"ugers Archiv European journal of physiology*, vol. 391, nº. 2, p. 85–100, 1981.

[78] B. Sakmann et E. Neher, *Single-Channel Recording*. Springer, 2009.

[79] J. Pawley, *Handbook of Biological Confocal Microscopy*. Springer, 2006.

[80] K. König, A. P. Raphael, L. Lin, J. E. Grice, H. P. Soyer, H. G. Breunig, M. S. Roberts, et T. W. Prow, « Applications of multiphoton tomographs and femtosecond laser nanoprocessing microscopes in drug delivery research », *Advanced drug delivery reviews*, 2011.

[81] H. G. Breunig, R. Bückle, M. Kellner-Höfer, M. Weinigel, J. Lademann, W. Sterry, et K. König, « Combined in vivo multiphoton and CARS imaging of healthy and disease-affected human skin », *Microscopy Research and Technique*, 2011.

[82] A. K. Swan, L. A. Moiseev, C. R. Cantor, B. Davis, S. B. Ippolito, W. C. Karl, B. B. Goldberg, et M. S. Unlu, « Toward nanometer-scale resolution in fluorescence microscopy using spectral self-interference », *Selected Topics in Quantum Electronics, IEEE Journal of*, vol. 9, nº. 2, p. 294–300, 2003.

[83] C. Mauroy, T. Portet, M. Winterhalder, E. Bellard, M.-C. Blache, J. Teissié, A. Zumbusch, et M.-P. Rols, « Giant lipid vesicles under electric field pulses assessed by non invasive imaging », *Bioelectrochemistry*, vol. 87, nº. 0, p. 253-259, oct. 2012.

[84] A. Silve, N. Dorval, T. Schmid, L. m. Mir, et B. Attal-Tretout, « A wide-field arrangement for single-shot CARS imaging of living cells », *Journal of Raman Spectroscopy*, vol. 43, nº. 5, p. 644–650, 2012.

[85] H. Leontiadou, A. E. Mark, et S. J. Marrink, « Molecular dynamics simulations of hydrophilic pores in lipid bilayers », *Biophysical journal*, vol. 86, nº. 4, p. 2156–2164, 2004.

[86] M. Tarek, « Membrane electroporation: a molecular dynamics simulation », *Biophysical journal*, vol. 88, nº. 6, p. 4045–4053, 2005.

[87] P. Marracino, F. Apollonio, M. Liberti, G. D'Inzeo, A. Amadei, M. Aschi, et A. Di Nola, « Molecular simulations of micellar carriers in presence of high intense electric fields », in *9th IEEE Conference on Nanotechnology, 2009. IEEE-NANO 2009*, 2009, p. 787 -789.

[88] J.-X. Cheng, S. Pautot, D. A. Weitz, et X. S. Xie, « Ordering of water molecules between phospholipid bilayers visualized by coherent anti-Stokes Raman scattering microscopy », *PNAS*, vol. 100, nº. 17, p. 9826-9830, août 2003.

[89] K. Kneipp, H. Kneipp, I. Itzkan, R. R. Dasari, et M. S. Feld, « Ultrasensitive chemical analysis by Raman spectroscopy », *Chem. Rev*, vol. 99, nº. 10, p. 2957–2976, 1999.

[90] H. J. Van Manen, Y. M. Kraan, D. Roos, et C. Otto, « Single-cell Raman and fluorescence microscopy reveal the association of lipid bodies with phagosomes in leukocytes », *Proceedings of the National Academy of Sciences of the United States of America*, vol. 102, nº. 29, p. 10159, 2005.

[91] P. D. Maker et R. W. Terhune, « Study of optical effects due to an induced polarization third order in the electric field strength », *Phys. Rev*, vol. 137, p. 801–818, 1965.

[92] S. J. Lockett, G. R. Holtom, et L. G. Rodriguez, « Coherent Anti-Stokes Raman Scattering Microscopy : A Biological Review », *Cytometry*, vol. 791, p. 779-791, 2006.

[93] C. L. Evans et X. S. Xie, « Coherent Anti-Stokes Raman Scattering Microscopy: Chemical Imaging for Biology and Medicine », *Annual Review of Analytical Chemistry*, vol. 1, nº. 1, p. 883-909, juill. 2008.

[94] J. R. Baena et B. Lendl, « Raman spectroscopy in chemical bioanalysis », *Current opinion in chemical biology*, vol. 8, nº. 5, p. 534–539, 2004.

[95] D. I. Ellis et R. Goodacre, « Metabolic fingerprinting in disease diagnosis: biomedical applications of infrared and Raman spectroscopy », *Analyst*, vol. 131, nº. 8, p. 875–885, 2006.

[96] P. A. Franken, A. E. Hill, C. W. Peters, et G. Weinreich, « Generation of optical harmonics », *Physical Review Letters*, vol. 7, nº. 4, p. 118–119, 1961.

[97] W. Kaiser et C. G. B. Garrett, « Two-Photon Excitation in CaF_ ${$2$}$: Eu^${$2+$}$ », *Physical Review Letters*, vol. 7, nº. 6, p. 229–231, 1961.

[98] G. Eckhardt, R. W. Hellwarth, F. J. McClung, S. E. Schwarz, D. Weiner, et E. J. Woodbury, « Stimulated Raman scattering from organic liquids », *Physical Review Letters*, vol. 9, nº. 11, p. 455–457, 1962.

[99] H. Lotem, R. T. Lynch, et N. Bloembergen, « Interference between Raman resonances in four-wave difference mixing », *Phys. Rev. A*, vol. 14, nº. 5, p. 1748, nov. 1976.

[100] M. D. Duncan, J. Reintjes, et T. J. Manuccia, « Scanning coherent anti-Stokes Raman microscope », *Opt. Lett.*, vol. 7, nº. 8, p. 350-352, 1982.

[101] D. M.D., « Molecular discrimination and contrast enhancement using a scanning coherent anti-stokes Raman microscope », *Optics Communications*, vol. 50, nº. 5, p. 307-312, Luglio 1984.

[102] M. Duncan, J. Reintjes, et T. Manuccia, « Imaging biological compounds using the coherent anti-Stokes Raman scattering microscope », *Optical engineering*, vol. 24, nº. 2, p. 352–355, 1985.

[103] A. Zumbusch, G. R. Holtom, et X. S. Xie, « Three-dimensional vibrational imaging by coherent anti-Stokes Raman scattering », *Physical Review Letters*, vol. 82, nº. 20, p. 4142–4145, 1999.

[104] A. Volkmer, J. X. Cheng, et X. Sunney Xie, « Vibrational imaging with high sensitivity via epidetected coherent anti-Stokes Raman scattering microscopy », *Physical Review Letters*, vol. 87, nº. 2, p. 23901, 2001.

[105] J. X. Cheng, Y. K. Jia, G. Zheng, et X. S. Xie, « Laser-scanning coherent anti-Stokes Raman scattering microscopy and applications to cell biology », *Biophysical journal*, vol. 83, nº. 1, p. 502–509, 2002.

[106] K. Hiramatsu, M. Okuno, H. Kano, P. Leproux, V. Couderc, et H. Hamaguchi, « Observation of Raman Optical Activity by Heterodyne-Detected Polarization-Resolved Coherent Anti-Stokes Raman Scattering », *Physical Review Letters*, vol. 109, nº. 8, p. 83901, 2012.

[107] J. A. Shirley, R. J. Hall, et A. C. Eckbreth, « Folded BOXCARS for rotational Raman studies », *Optics Letters*, vol. 5, nº. 9, p. 380–382, 1980.

[108] J. X. Cheng, A. Volkmer, et X. S. Xie, « Theoretical and experimental characterization of coherent anti-Stokes Raman scattering microscopy », *JOSA B*, vol. 19, nº. 6, p. 1363–1375, 2002.

[109] J.-X. Cheng, « Coherent Anti-Stokes Raman Scattering Microscopy », *Appl Spectrosc*, vol. 61, nº. 9, p. 197-208, sept. 2007.

[110] J. X. Cheng et X. S. Xie, « Coherent anti-Stokes Raman scattering microscopy: instrumentation, theory, and applications », *The Journal of Physical Chemistry B*, vol. 108, nº. 3, p. 827–840, 2004.

[111] J. L. Oudar, R. W. Smith, et Y. Shen, « Polarization-sensitive coherent anti-Stokes Raman spectroscopy », *Applied Physics Letters*, vol. 34, nº. 11, p. 758–760, 1979.

[112] A. Laubereau et W. Kaiser, « Vibrational dynamics of liquids and solids investigated by picosecond light pulses », *Reviews of Modern Physics*, vol. 50, nº. 3, p. 607, 1978.

[113] B. Hudson, W. Hetherington, S. Cramer, I. Chabay, et G. K. Klauminzer, « Resonance enhanced coherent anti-Stokes Raman scattering », *Proceedings of the National Academy of Sciences*, vol. 73, nº. 11, p. 3798 - 3802, nov. 1976.

[114] J. Andrews, R. Hochstrasser, et H. Trommsdorff, « Vibrational transitions in excited states of molecules using coherent stokes raman spectroscopy: application to ferrocytochrome-C* 1 », *Chemical Physics*, vol. 62, nº. 1-2, p. 87–101, 1981.

[115] Y. Yacoby, R. Fitzgibbon, et B. Lax, « Coherent cancellation of background in four-wave mixing spectroscopy », *Journal of Applied Physics*, vol. 51, nº. 6, p. 3072–3077, 1980.

[116] A. Volkmer, L. D. Book, et X. S. Xie, « Time-resolved coherent anti-Stokes Raman scattering microscopy: Imaging based on Raman free induction decay », *Applied Physics Letters*, vol. 80, nº. 9, p. 1505-1507, mars 2002.

[117] D. L. Marks, C. Vinegoni, J. S. Bredfeldt, et S. A. Boppart, « Interferometric differentiation between resonant coherent anti-Stokes Raman scattering and nonresonant four-wave-mixing processes », *Applied physics letters*, vol. 85, nº. 23, p. 5787–5789, 2004.

[118] S. A. Akhmanov, N. I. Koroteev, et A. I. Kholodnykh, « Excitation of the coherent optical phonons of Eg-type

in calcite by means of the active spectroscopy method », *Journal of Raman Spectroscopy*, vol. 2, nº. 3, p. 239-248, juin 1974.

[119] M. Müller et J. M. Schins, « Imaging the Thermodynamic State of Lipid Membranes with Multiplex CARS Microscopy », *J. Phys. Chem. B*, vol. 106, nº. 14, p. 3715-3723, oct. 2011.

[120] C. Otto, A. Voroshilov, S. Kruglik, et J. Greve, « Vibrational bands of luminescent zinc (II)-octaethylporphyrin using a polarization-sensitive 'microscopic'multiplex CARS technique », *Journal of Raman Spectroscopy*, vol. 32, nº. 6-7, p. 495–501, 2001.

[121] B. Toleutaev, T. Tahara, et H. Hamaguchi, « Broadband (1000 cm- 1) multiplex CARS spectroscopy: Application to polarization sensitive and time-resolved measurements », *Applied Physics B: Lasers and Optics*, vol. 59, nº. 4, p. 369–375, 1994.

[122] A. Voroshilov, C. Otto, et J. Greve, « Secondary structure of bovine albumin as studied by polarization-sensitive multiplex CARS spectroscopy », *Applied spectroscopy*, vol. 50, nº. 1, p. 78–85, 1996.

[123] J. X. Cheng et X. S. Xie, « Coherent anti-Stokes Raman scattering microscopy: instrumentation, theory, and applications », *J. Phys. Chem. B*, vol. 108, nº. 3, p. 827–840, 2004.

[124] M. Hashimoto, T. Araki, et S. Kawata, « Molecular vibration imaging in the fingerprint region by use of coherent anti-Stokes Raman scattering microscopy with a collinear configuration », *Optics letters*, vol. 25, nº. 24, p. 1768–1770, 2000.

[125] E. O. Potma, D. J. Jones, J. X. Cheng, X. S. Xie, et J. Ye, « High-sensitivity coherent anti-Stokes Raman scattering microscopy with two tightly synchronized picosecond lasers », *Optics letters*, vol. 27, nº. 13, p. 1168–1170, 2002.

[126] C. L. Evans, E. O. Potma, M. Puoris' haag, D. Côté, C. P. Lin, et X. S. Xie, « Chemical imaging of tissue in vivo with video-rate coherent anti-Stokes Raman scattering microscopy », *Proceedings of the National Academy of Sciences of the United States of America*, vol. 102, nº. 46, p. 16807, 2005.

[127] H. N. Paulsen, K. M. Hilligse, J. ThU00F8gersen, S. R. Keiding, et J. J. Larsen, « Coherent anti-Stokes Raman scattering microscopy with a photonic crystal fiber based light source », *Optics letters*, vol. 28, nº. 13, p. 1123–1125, 2003.

[128] T. W. Kee et M. T. Cicerone, « Simple approach to one-laser, broadband coherent anti-Stokes Raman scattering microscopy », *Optics letters*, vol. 29, nº. 23, p. 2701–2703, 2004.

[129] F. Ganikhanov, S. Carrasco, X. Sunney Xie, M. Katz, W. Seitz, et D. Kopf, « Broadly tunable dual-wavelength light source for coherent anti-Stokes Raman scattering microscopy », *Optics letters*, vol. 31, nº. 9, p. 1292–1294, 2006.

[130] M. Okuno, H. Kano, P. Leproux, V. Couderc, et H. Hamaguchi, « Ultrabroadband (> 2000 cm^- 1) multiplex coherent anti-Stokes Raman scattering spectroscopy using a subnanosecond supercontinuum light source », *Optics letters*, vol. 32, nº. 20, p. 3050–3052, 2007.

[131] M. Okuno, H. Kano, P. Leproux, V. Couderc, et H. Hamaguchi, « Ultrabroadband multiplex CARS microspectroscopy and imaging using a subnanosecond supercontinuum light source in the deep near infrared », *Optics letters*, vol. 33, nº. 9, p. 923–925, 2008.

[132] M. Okuno, H. Kano, P. Leproux, V. Couderc, J. P. R. Day, M. Bonn, et H. Hamaguchi, « Quantitative CARS molecular fingerprinting of single living cells with the use of the maximum entropy method », *Angewandte Chemie International Edition*, vol. 49, nº. 38, p. 6773–6777, 2010.

[133] C. Lin et R. Stolen, « New nanosecond continuum for excited-state spectroscopy », *Applied Physics Letters*, vol. 28, nº. 4, p. 216–218, 1976.

[134] A. Mussot, T. Sylvestre, L. Provino, et H. Maillotte, « Generation of a broadband single-mode supercontinuum in a conventional dispersion-shifted fiber by use of a subnanosecond microchiplaser », *Optics letters*, vol. 28, nº. 19, p. 1820–1822, 2003.

[135] G. Genty, T. Ritari, et H. Ludvigsen, « Supercontinuum generation in large mode-area microstructured fibers », in *Optical Communication, 2005. ECOC 2005. 31st European Conference on*, 2005, vol. 3, p. 513–514.

[136] E. Räikkönen, G. Genty, O. Kimmelma, M. Kaivola, K. P. Hansen, et S. C. Buchter, « Supercontinuum generation by nanosecond dual-wavelength pumping in microstructured optical fibers », *Optics express*,

vol. 14, nº. 17, p. 7914–7923, 2006.

[137] E. E. Serebryannikov et A. M. Zheltikov, « Supercontinuum generation through cascaded four-wave mixing in photonic-crystal fibers: When picoseconds do it better », *Optics Communications*, vol. 274, nº. 2, p. 433–440, 2007.

[138] S. Gao, X. Li, et S. Zhang, « Supercontinuum generation by combining clad-pumped Er/Yb co-doped fiber amplifier and highly nonlinear photonic crystal fiber », *Optik-International Journal for Light and Electron Optics*, vol. 121, nº. 23, p. 2110–2112, 2010.

[139] J. Cheng, A. Volkmer, D. Lewis, et X. S. Xie, « An epi-detected coherent anti-Stokes Raman scattering (E-CARS) microscope with high spectral resolution and high sensitivity », *The Journal of Physical Chemistry B*, vol. 105, nº. 7, p. 1277–1280, 2001.

[140] P. Leproux, V. Couderc, A. de Angelis, M. Okuno, H. Kano, et H. Hamaguchi, « New opportunities offered by compact sub-nanosecond supercontinuum sources in ultra-broadband multiplex CARS microspectroscopy », *Journal of Raman Spectroscopy*.

[141] R. R. Alfano et S. L. Shapiro, « Observation of Self-Phase Modulation and Small-Scale Filaments in Crystals and Glasses », *Phys. Rev. Lett.*, vol. 24, nº. 11, p. 592, mars 1970.

[142] N. G. Bondarenko, I. V. Eremina, et V. I. Talanov, « Broadening of Spectrum in Self Focusing of Light in Crystals », 1970. [Online]. Available: http://adsabs.harvard.edu/abs/1970JETPL..12...85B. [Accessed: 07-oct-2011].

[143] W. Werncke, A. Lau, M. Pfeiffer, K. Lenz, H. J. Weigmann, et C. Thuy, « An anomalous frequency broadening in water », *Optics Communications*, vol. 4, nº. 6, p. 413–415, 1972.

[144] J. E. Rothenberg, « Space-time focusing: breakdown of the slowly varying envelope approximation in the self-focusing of femtosecond pulses », *Opt. Lett.*, vol. 17, nº. 19, p. 1340-1342, Ottobre 1992.

[145] B. N., « The influence of electron plasma formation on superbroadening in light filaments », *Optics Communications*, vol. 8, nº. 4, p. 285-288, Agosto 1973.

[146] P. Kaiser et H. Astle, « Low-loss single-material fibers made from pure fused silica », *Bell System Technical Journal*, vol. 53, nº. 6, p. 1021–39, 1974.

[147] J. C. Knight, T. A. Birks, P. S. J. Russell, et D. M. Atkin, « All-silica single-mode optical fiber with photonic crystal cladding », *Opt. Lett.*, vol. 21, nº. 19, p. 1547-1549, Ottobre 1996.

[148] K. P. Hansen et R. E. Kristiansen, « Supercontinuum generation in photonic crystal fibers », *Application Note, Crystal Fibre A/S*, 2005.

[149] A. Bjarklev, A. S. Bjarklev, et J. Broeng, *Photonic crystal fibers*. Springer Netherlands, 2003.

[150] V. Tombelaine, « Etude de rayonnements à large bande spectrale induits dans les fibres optiques microstructurées air-silice », Université de Limoges, 2007.

[151] G. P. Agrawal, *Applications of nonlinear fiber optics*. Academic Press, 2008.

[152] G. P. Agrawal, P. L. Baldeck, et R. R. Alfano, « Modulation instability induced by cross-phase modulation in optical fibers », *Physical Review A*, vol. 39, nº. 7, p. 3406–3413, 1989.

[153] Y. Kodama et A. Hasegawa, « Nonlinear pulse propagation in a monomode dielectric guide », *Quantum Electronics, IEEE Journal of*, vol. 23, nº. 5, p. 510–524, 1987.

[154] P. Beaud, W. Hodel, B. Zysset, et H. Weber, « Ultrashort pulse propagation, pulse breakup, and fundamental soliton formation in a single-mode optical fiber », *Quantum Electronics, IEEE Journal of*, vol. 23, nº. 11, p. 1938–1946, 1987.

[155] N. Tzoar et M. Jain, « Self-phase modulation in long-geometry optical waveguides », *Physical Review A*, vol. 23, nº. 3, p. 1266, 1981.

[156] W. Tomlinson, R. Stolen, et C. Shank, « Compression of optical pulses chirped by self-phase modulation in fibers », *JOSA B*, vol. 1, nº. 2, p. 139–149, 1984.

[157] P. Baldeck, R. Alfano, et G. P. Agrawal, « Induced-frequency shift of copropagating ultrafast optical pulses », *Applied physics letters*, vol. 52, nº. 23, p. 1939–1941, 1988.

[158] I. K. Ilev, H. Kumagai, et K. Toyoda, « A widely tunable (0.54–1.01 μm) double-pass fiber Raman

laser », *Applied physics letters*, vol. 69, p. 1846, 1996.

[159] L. F. Mollenauer, R. H. Stolen, J. P. Gordon, et W. Tomlinson, « Extreme picosecond pulse narrowing by means of soliton effect in single-mode optical fibers », *Optics Letters*, vol. 8, nº. 5, p. 289–291, 1983.

[160] J. P. Gordon, « Theory of the soliton self-frequency shift », *Opt. Lett.*, vol. 11, nº. 10, p. 662-664, Ottobre 1986.

[161] F. M. Mitschke et L. F. Mollenauer, « Discovery of the soliton self-frequency shift », *Optics letters*, vol. 11, nº. 10, p. 659–661, 1986.

[162] M. Islam, C. Poole, et J. Gordon, « Soliton trapping in birefringent optical fibers », *Optics letters*, vol. 14, nº. 18, p. 1011–1013, 1989.

[163] M. N. Islam, E. Sunderman, R. H. Stolen, W. Pleibel, et J. R. Simpson, « Soliton switching in a fiber nonlinear loop mirror », *Optics letters*, vol. 14, nº. 15, p. 811–813, 1989.

[164] J. K. Ranka, R. S. Windeler, et A. J. Stentz, « Visible continuum generation in air-silica microstructure optical fibers with anomalous dispersion at 800 nm », *Optics Letters*, vol. 25, nº. 1, p. 25–27, 2000.

[165] P. Russell, « Photonic crystal fibers », *Science*, vol. 299, nº. 5605, p. 358, 2003.

[166] J. C. Knight, « Photonic crystal fibres », *Nature*, vol. 424, nº. 6950, p. 847–851, 2003.

[167] W. Reeves, D. Skryabin, F. Biancalana, J. Knight, P. S. J. Russell, F. Omenetto, A. Efimov, et A. Taylor, « Transformation and control of ultra-short pulses in dispersion-engineered photonic crystal fibres », *Nature*, vol. 424, nº. 6948, p. 511–515, 2003.

[168] V. P. Mitrokhin, A. B. Fedotov, A. A. Ivanov, M. V. Alfimov, et A. M. Zheltikov, « Coherent anti-Stokes Raman scattering microspectroscopy of silicon components with a photonic-crystal fiber frequency shifter », *Optics letters*, vol. 32, nº. 23, p. 3471–3473, 2007.

[169] S. V. Smirnov, J. D. Ania-Castanon, T. J. Ellingham, S. M. Kobtsev, S. Kukarin, et S. K. Turitsyn, « Optical spectral broadening and supercontinuum generation in telecom applications », *Optical Fiber Technology*, vol. 12, nº. 2, p. 122–147, 2006.

[170] C. F. Kaminski, R. S. Watt, A. D. Elder, J. H. Frank, et J. Hult, « Supercontinuum radiation for applications in chemical sensing and microscopy », *Applied Physics B: Lasers and Optics*, vol. 92, nº. 3, p. 367–378, 2008.

[171] J. Clowes, « Next Generation Light Sources for Biomedical Applications », *Optik & Photonik*, vol. 3, nº. 1, p. 36–38, 2008.

[172] S. El Amari, A. De Angelis, D. Arnaud-Cormos, V. Couderc, et P. Leveque, « Characterization of a Linear Photoconductive Switch Used in Nanosecond Pulsed Electric Field Generator », *IEEE Photonics Technology Letters*, vol. 23, nº. 11, p. 673 -675, juin 2011.

[173] R. N. Hall, « Electron-hole recombination in germanium », *Physical Review*, vol. 87, nº. 2, p. 387, 1952.

[174] F. J. Zutavern, G. M. Loubriel, M. O'Malley, L. Shanwald, W. Helgeson, D. McLaughlin, et B. McKenzie, « Photoconductive semiconductor switch experiments for pulsed power applications », *Electron Devices, IEEE Transactions on*, vol. 37, nº. 12, p. 2472–2477, 1990.

[175] B. Vergne, « Synthèse d'onde électriques picosecondes de puissance par commutation optoélectronique-Application aux radars à bande spectrale ultralarge », Université de Limoges, 2006.

[176] W. C. Nunnally, « High-power microwave generation using optically activated semiconductor switches », *Electron Devices, IEEE Transactions on*, vol. 37, nº. 12, p. 2439–2448, 1990.

[177] A. L. Ivanov, L. V. Keldysh, et V. V. Panashchenko, « Low-threshold exciton-biexciton optical Stark effect in direct-gap semiconductors », *Soviet physics, JETP*, vol. 72, nº. 2, p. 359–367, 1991.

[178] C. Dalmay, M. Cheray, A. Pothier, F. Lalloué, M. O. Jauberteau, et P. Blondy, « Ultra sensitive biosensor based on impedance spectroscopy at microwave frequencies for cell scale analysis », *Sensors and Actuators A: Physical*, vol. 162, nº. 2, p. 189-197, août 2010.

[179] M. Andreana, « Soliton propagation in crystals and optical fibres », 2011.

[180] D. Herriott, H. Kogelnik, et R. Kompfner, « Off-axis paths in spherical mirror interferometers », *Applied Optics*, vol. 3, nº. 4, p. 523–526, 1964.

[181] D. R. Herriott et H. J. Schulte, « Folded optical delay lines », *Applied Optics*, vol. 4, nº. 8, p. 883–889, 1965.

[182] A. Sennaroglu et J. Fujimoto, « Design criteria for Herriott-type multi-pass cavities for ultrashort pulse lasers », *Optics Express*, vol. 11, nº. 9, p. 1106–1113, 2003.

[183] Annalisa De Angelis, Vincent Couderc, Philippe Leproux, et Guillaume Huss, « Nonlinear imaging laser source », U.S. Patent WO/2012/05244727-avr-2012.

[184] W. Koechner, *Solid-state laser engineering*, Third completely and updated edition., vol. 1. Springer-Verlag, 1992.

[185] J. M. Dudley, G. Genty, et S. Coen, « Supercontinuum generation in photonic crystal fiber », *Reviews of modern physics*, vol. 78, nº. 4, p. 1135, 2006.

[186] J. M. Dudley et J. R. Taylor, *Supercontinuum Generation in Optical Fibers*. Cambridge University Press, 2010.

[187] L. M. Mir, S. Orlowski, J. Belehradek, J. Teissie, M. P. Rols, G. Ser\vsa, D. Miklav\vci\vc, R. Gilbert, et R. Heller, « Biomedical applications of electric pulses with special emphasis on antitumor electrochemotherapy », *Bioelectrochemistry and bioenergetics*, vol. 38, nº. 1, p. 203–207, 1995.

[188] D. H. Michael et M. E. O'Neill, « Electrohydrodynamic instability in plane layers of fluid », *J. Fluid Mech*, vol. 41, nº. part 3, p. 571–580, 1970.

[189] I. P. Sugár, « A theory of the electric field-induced phase transition of phospholipid bilayers », *Biochimica et Biophysica Acta (BBA)-Biomembranes*, vol. 556, nº. 1, p. 72–85, 1979.

[190] L. Cruzeiro-Hansson et O. G. Mouritsen, « Passive ion permeability of lipid membranes modelled via lipid-domain interfacial area », *Biochimica et Biophysica Acta (BBA)-Biomembranes*, vol. 944, nº. 1, p. 63–72, 1988.

[191] C. A. Balanis, *Antenna theory: analysis and design/Constantine A. Balanis*. J. Wiley, New York, 1982.

[192] R. J. P. Douville et D. S. James, « Experimental study of symmetric microstrip bends and their compensation », *Microwave Theory and Techniques, IEEE Transactions on*, vol. 26, nº. 3, p. 175–182, 1978.

APPENDIX A- Calculation of the impedance-matched microstrip line dimension

In order to design the microstrips line of the generator we used the approximated formulas of Schneider and Hammerstad [191]

$\frac{w}{h} \geq 2$

$$Z_c = \frac{120\pi}{\sqrt{\varepsilon_r}}\left[\frac{w}{h} + 0.833 + \frac{\varepsilon_r + 1}{\pi\varepsilon_r}\left\{Ln\left(\frac{w}{2h} + 0.94\right) + 1.451\right\} + 0.165\frac{\varepsilon_r - 1}{\varepsilon_r^{\,2}}\right]^{-1} \quad \textbf{(44)}$$

$\frac{w}{h} < 2$

$$Z_c = \frac{60\sqrt{\varepsilon_r}}{\sqrt{\varepsilon_r + 1}}\left[Ln\left(\frac{8h}{w}\right) + \frac{1}{8}\left(\frac{w}{2h}\right)^2 - \frac{\varepsilon_r - 1}{2(1+\varepsilon_r)}\left\{Ln\left(\frac{\pi}{2}\right) + \frac{1}{\varepsilon_r}Ln\frac{4}{\pi}\right\}\right] \quad \textbf{(45)}$$

In our case we have:

$h = 1.6mm$ dielectric substrate thickness

$\varepsilon_r = 4.6$ relative permittivity of substrate at 1 MHz

In order to obtain a microstrip line characteristic impedance $Z_c = 50\Omega$, we need a width of the line w of 3 mm.

To obtain the needed microstrip line length, we calculate the propagation velocity as function of the effective permittivity:

$$v_{microstrip} = \frac{c_0}{\sqrt{\varepsilon_{eff}}} \quad \textbf{(46)}$$

The effective permittivity considers that the wave propagates in an inhomogeneous medium (substrate and air). We can calculate it as follows:

$$\varepsilon_{eff} = \frac{\varepsilon_r + 1}{2} + \frac{\varepsilon_r - 1}{2}\frac{1}{\sqrt{1 + 10\frac{h}{w}}} \quad \textbf{(47)}$$

Next, considering that the pulse duration is equal to two times the propagation time along the line, we can calculate the length of the microstrip as:

$$d = \frac{v_m \Delta T}{2} \quad \textbf{(48)}$$

So in order to generate pulses of 2-ns and <1-ns duration we designed two lines of different length: 16 cm and 6 cm, respectively.

For building a complete circuit in microstrip, it is often necessary for the path of a strip to turn through a large angle. An abrupt 90° bend in a microstrip will cause a significant portion of the signal on the strip to be reflected back towards its source, with only part of the signal transmitted on around the bend. One means of effecting a low-reflection bend, is to curve the path of the strip in an arc of radius at least 3 times the strip-width [T.H. Lee, Planar Microwave Engineering; *Cambridge University Press*, pp. 173-174, 2004]. However, a far more common technique, and one which consumes a smaller area of substrate, is to use a mitred bend.

To a first approximation, an abrupt un-mitred bend behaves as a shunt capacitance placed between the ground plane and the bend in the strip. Mitring the bend reduces the area of metallization, and so removes the excess capacitance. The percentage mitre is the cut-away fraction of the diagonal between the inner and outer corners of the un-mitred bend.

The optimum mitre for a wide range of microstrip geometries has been determined experimentally by Douville and James [192]. They find that a good fit for the optimum percentage mitre is given by,

$$M = 100\frac{x}{d}\% = (52 + 65e^{-\frac{27}{20}\frac{w}{h}})\% \quad \textbf{(49)}$$

subject to $w/h \geq 0.25$ and with the substrate dielectric constant $\varepsilon_r \leq 25$. This formula is entirely independent of ε_r. The actual range of parameters for which Douville and James present evidence is $0.25 \leq w/h \leq 2.75$ and $2.5 \leq \varepsilon_r \leq 25$. For both the curved and mitred bends, the electrical length is somewhat shorter than the physical path-length of the strip.

APPENDIX B- The “stack-and-draw” process

“Stack-and-draw” is the name of the procedure generally used in the fabrication of high quality custom-designed PCF. That technique relies on manual assembly of glass capillaries and rods into an appropriate pre-form stack whose structure corresponds approximately to the desired fiber structure. After inserting the pre-form stack into a glass tube and fusing during the drawing process, one obtains a microstructured pre-form or "cane". The final step in PCF fabrication involves drawing the cane into fiber with the desired dimensions, such as cladding-lattice pitch and the outer fiber diameter. By tuning process parameters such as temperature, pre-form feed rate and drawing speed, as well as the pressure inside the pre-form, the size of the air-holes and their regularity can be controlled. As for standard fibers, the fabricated PCF is coated with a polymer jacket for improved mechanical strength.

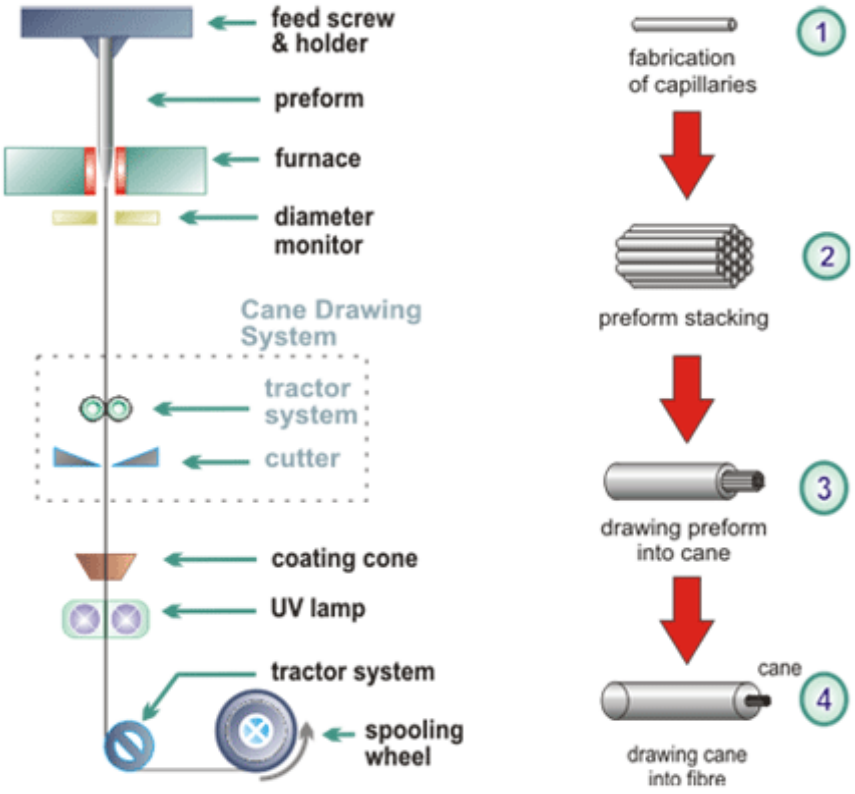

Figure B-1: *Steps in the fabrication of photonic crystal fibers. (1) 1-mm thick capillaries are drawn to precise dimensions and then (2) stacked to form the desired "pre-form". (3) The pre-form is fused together and drawn down in size to a "cane" (~ 1 mm in diameter). (4) In the final drawing step, the cane is drawn down to fiber and encased in a silica outer cladding.*

List of Communications

Papers

"*A novel electro-optical pump-probe system for bioelectromagnetic investigations*".
A. De Angelis, V. Couderc, P. Leproux, A. Labruyère, A. Tonello, S. El Amari, D. Arnoud-Cormos, P. Leveque; Proc. SPIE 8487, Novel Optical System Design and Optimization, (2012).

"*Time-frequency resolved analysis of a nanosecond supercontinuum source dedicated to multiplex CARS application".*
A. De Angelis, A. Labruyère, V. Couderc, P. Leproux, A. Tonello, H. Segawa, M. Okuno, H. Kano, D. Arnaud-Cormos, P. Leveque, and H. Hamaguchi; Optics Express (2012). (Accepted)

"*Characterization of a Linear Photoconductive Switch used in nanosecond pulsed electric field generator*".
S. El Amari, **A. De Angelis**, D. Arnoud-Cormos, V. Couderc, P. Leveque; Photonic Technology Letters, IEEE 23, 11(2011).

"*New opportunities offered by compact sub-nanosecond supercontinuum sources in ultra-broadband multiplex CARS microscopy*".
P. Leproux, V. Couderc, **A. De Angelis**, M. Okuno, H. Kano, H. Hamaguchi ; Journal of Raman Spectroscopy 42, 10 (2011).

International conferences

"*Compact sub-nanosecond supercontinuum sources for ultrabroadband multiplex CARS microspectroscopy*".
P. Leproux, V. Couderc, **A. De Angelis**, P. Leveque, G. Huss M. Okuno, H. Kano, H. Hamaguchi ; ECONOS, Germany (2010) (Oral presentation).

"*New biomedical opportunities offered by compact sub-nanosecond supercontinuum sources*".
P. Leproux, V. Couderc, A. Labruyere, M. Andreana, **A. De Angelis**; International Conference on Fiber Optics and Photonics, PHOTONICS INDIAN, India (2010) (Invited speaker).

"*Twofold coherent and incoherent subnanosecond laser emission for CARS spectroscopy*".

A. De Angelis, D. Arnoud-Cormos, P. Leveque , P. Leproux, V. Couderc; 10th International Conference of the European BioElectromagnetics Association, EBEA-2011, Rome, Italy (2011) (Poster session).

"*Spectro-temporal characterisation of incoherent supercontinuum subnanosecond laser emission for multiplex-CARS microspectroscopy*".

A. De Angelis, P. Leproux, V. Couderc, D. Arnoud-Cormos, P. Leveque ; Conference on Laser and Electro-Optics Europe, and 12th European Quantum Electronics Conference (CLEO-Europe/EQEC), Munich, Germany (2011) (Oral presentation).

"*A novel electro-optical pump-probe system for bioelectromagnetic investigations".*

A. De Angelis, V. Couderc, P. Leproux, A. Labruyere, A. Tonello, S. El Amari, D. Arnoud-Cormos, P. Leveque ; Optical Engineering and Applications, SPIE Optics+Photonics 2012, San Diego, California (2012) (Oral presentation).

National Conference

"*Caractérisation spectro-temporelle d'une source supercontinuum incohérente dédiée à la microspectroscopie CARS"*.

A. De Angelis, P. Leproux, V. Couderc, D. Arnoud-Cormos, P. Leveque ; Deuxième Colloque francophone PLUridisciplinaire sur le Matériaux , l'Environnement et l'Electronique, PLUMEE, Limoges, France (2011) (Poster session).

"*Analyse en temps et en fréquence d'une source laser large bande pour l'imagerie CARS "*.

A. De Angelis, A. Labruyère, P. Leproux, A. Tonello, D. Arnoud-Cormos, P. Leveque, H. Kano, V. Couderc; JNOG 2012- Session : Capteurs-Techniques de caractérisation, Lyon, France (2012) (Oral presentation).

Patents

« Nonlinear imaging laser source ».

A. De Angelis, V. Couderc, G. Huss, P. Leproux.

Registered on October 18, 2010, n° 1058472, ref. 27658/011FR (France)

Registered on April 27, 2012, n° WO/2012/052447 (International)

Title: Electro-optical system suitable for the investigation of electroporated biological cells

Abstract

A sufficiently strong electric field is able to change the cell membrane permeability, forming aqueous pores across it, hence the name *electroporation*, permitting the passage, otherwise forbidden, of ions and molecules. Since its efficient application in biotechnology and medicine (e.g. electrochemotherapy), ms/µs-pulse-induced electroporation draws growing interest. Recently, the application of nanosecond pulses has showed electroperturbation on intracellular membranes, opening the way to subcellular manipulations. To date, the mechanisms beyond the electroporation are not still well known. The lack of ultra-rapid and flexible pulsers for cell stimulation on the one hand, and the rapid and subcellular-scale involved dynamics on the other hand, make the investigations complex.

In this context, we have designed and realized a compact system providing both the electric pump and the optical probe for electroporation studies. The electric pump consists of a photocommutation-based pulse generator triggered by a sub-nanosecond microchip laser that also provides the optical excitation of the multiplex-CARS microscope used for cell imaging.

The main innovation of this system is represented by the sub-nanosecond regime of the common laser source. This choice is justified by the need for synchronizing the nanosecond electrical stimulation with the optical detection. A detailed analysis in the time and frequency domains has been performed in order to verify the whole system efficiency and applicability to nano-electroporation investigations.

Keywords: Electroporation, multiplex-CARS, photocommutation-based generator, supercontinuum, photonic crystal fiber, Bio-Electro-Photonic.

Titre: Système électro-optique pompe-sonde pour l'étude de cellules biologiques électroporées

Résumé

Un champ électrique suffisamment intense induit des effets sur la membrane cellulaire, notamment la formation des pores qui permettent le passage , autrement interdit, de ions et molécules, d'où le nom *électroporation*. Grâce à son application à la biotechnologie et à la médicine (électrochimiothérapie), l'électroporation représente un phénomène de grand intérêt. Récemment, des impulsions de l'ordre de la nanoseconde ont étés appliquées, montrant des effets sur les membranes intracellulaires. Les mécanismes qui sont à la base de l'électroporation ne sont pas encore complètement compris. D'une part, il n'y a pas en commerce de générateurs ultra-rapides et flexibles pour une stimulation électrique adaptée. D'autre part, la détection de phénomènes à l'échelle subcellulaire et de dynamiques temporelles rapides résulte très difficile. En ce contexte, nous avons conçu et réalisé un système électro-optique pompe-sonde. Il se compose d'un système optoélectronique dédié à la génération d'impulsions ultracourtes et de forte intensité, et d'une source pour l'imagerie optique non linéaire basée sur la microspectroscopie multiplex-CARS. Les deux sources sont déclenchées par le même laser fonctionnant en régime sub-nanoseconde. Ce régime temporel permet une synchronisation efficace des deux systèmes, mais il nécessite d'une étude approfondie des effets optiques non linéaires qui induisent l'élargissement spectral du faisceau, indispensable pour l'imagerie multiplex-CARS. Une caractérisation dans le temps et en fréquence a été menée afin de vérifier les performances du system entier et son emploi aux études de nano-électroporation.

Mots-clés : Electroporation, CARS multiplex, générateur basé sur la photocommutation, supercontinuum, fibre à cristaux photoniques, Bio-Electro-Photonique.